UNIVERSITY OF ALBERTA

INTERFACIAL STRUCTURES AND ELECTRICAL PROPERTIES OF Ti AND Ge/Ni METALLIZATIONS TO InP

BY

DASHAN WANG ©

A thesis submitted to the Faculty of Graduate Studies and Research in partial fulfillment of the requirements for the degree of **MASTER OF SCIENCE**

IN

METALLURGICAL ENGINEERING
DEPARTMENT OF CHEMICAL AND MATERIALS ENGINEERING

EDMONTON, ALBERTA

Spring 1997

National Library of Canada
Acquisitions and Bibliographic Services
395 Wellington Street
Ottawa ON K1A 0N4
Canada

Bibliothèque nationale du Canada
Acquisitions et services bibliographiques
395, rue Wellington
Ottawa ON K1A 0N4
Canada

Your file Votre référence

Our file Notre référence

The author has granted a non-exclusive licence allowing the National Library of Canada to reproduce, loan, distribute or sell copies of his/her thesis by any means and in any form or format, making this thesis available to interested persons.

L'auteur a accordé une licence non exclusive permettant à la Bibliothèque nationale du Canada de reproduire, prêter, distribuer ou vendre des copies de sa thèse de quelque manière et sous quelque forme que ce soit pour mettre des exemplaires de cette thèse à la disposition des personnes intéressées.

The author retains ownership of the copyright in his/her thesis. Neither the thesis nor substantial extracts from it may be printed or otherwise reproduced with the author's permission.

L'auteur conserve la propriété du droit d'auteur qui protège sa thèse. Ni la thèse ni des extraits substantiels de celle-ci ne doivent être imprimés ou autrement reproduits sans son autorisation.

0-612-21218-1

Canadä

UNIVERSITY OF ALBERTA

RELEASE FORM

NAME OF AUTHOR: **Dashan Wang**

TITLE OF THESIS: **Interfacial Structures and Electrical Properties of Ti and Ge/Ni Metallizations to InP**

DEGREE: **Master of Science**

YEAR THIS DEGREE GRANTED: **Spring 1997**

Permission is hereby granted to the University of Alberta Library to reproduce single copies of this thesis, and to lend or sell such copies for private, scholarly or scientific research purposes only.

The author reserves all other publication and other rights in association with the copyright in the thesis, and except as hereinbefore provided neither the thesis nor any substantial portion thereof may be printed or otherwise reproduced in any material form whatever without the author's prior written permission.

Dashan Wang
208-10633 112 St
Edmonton, AB T5H 3G9

Date: Nov. 28, 1996

UNIVERSITY OF ALBERTA

FACULTY OF GRADUATE STUDIES AND RESEARCH

The undersigned certify that they have read, and recommend to the Faculty of Graduate Studies and Research for acceptance, a thesis entitled **INTERFACIAL STRUCTURES AND ELECTRICAL PROPERTIES OF Ti AND Ge/Ni METALLIZATIONS TO InP** submitted by **DASHAN WANG** in partial fulfillment of the requirements for the degree of **MASTER OF SCIENCE in METALLURGICAL ENGINEERING.**

D. Ivey

Dr. D.G. Ivey
Supervisor

ML Wayman

Dr. M.L. Wayman

MJ Brett

Dr. Michael Brett

DATE: Nov. 28. 1996

Abstract

The literature concerning the principles of ohmic contact formation and properties of InP is comprehensively reviewed. Interfacial reactions that occur during annealing in three metallization systems, i.e., Ti(100 nm)/InP, (annealed in forming gas: 95% N_2+5% H_2), Ni (50 nm)/InP, (annealed in vacuum) and Ge (52.5 nm)/Ni(25 nm)-InP, (annealed in forming gas), were characterized using transmission electron microscopy (TEM) and related techniques, Thin films for the three systems were deposited by electron beam evaporation onto <001> oriented InP.

Initial interfacial reactions between Ti thin films and InP were detected at 325°C, which resulted in the formation of metallic In and TiP. TiP formation was limited by kinetics at low temperatures and much of the P released during InP decomposition was lost to the atmosphere. The amount of TiP formation increased with increasing temperatures and TiP was the only Ti-P phase detected. No In-Ti compound formation was detected in any sample studied.

For Ni/InP metallizations, initial annealing (<250°C) led to the formation and growth of an amorphous ternary phase ($Ni_{\approx 3}InP$) at the Ni/InP interface. This was followed by crystallization of the amorphous ternary phase (250-300°C) to Ni_2InP and Ni_2P. Annealing at 500°C resulted in the decomposition of Ni_2InP to Ni_2P and metallic In, which subsequently oxidized forming In_2O_3.

In the Ge/Ni-InP system, an amorphous ternary phase similar to the one in the Ni/InP system formed between Ni and InP (< 250 °C). The amorphous ternary phase decomposed at 250°C forming a Ni_2P-type compound, which then transformed to GeNi. The GeNi is laterally uniform between 250 and 350°C. High temperature annealing resulted in a roughened InP interface and further InP decomposition. Specific contact resistances were measured using a modified transmission line method (TLM). Values as low as $10^{-6}\Omega$-cm^2 have been obtained. Microstructural changes have been correlated with the electrical results.

ACKNOWLEDGEMENTS

I am deeply grateful to Dr. D.G. Ivey, my supervisor, who supported, encouraged and guided me throughout this project and during my entire tenure at the University of Alberta.

I also greatly appreciate the financial support, materials needed in this study and the measurement of electrical properties of contacts provided by NORTEL

I wish to thank Dr. R.F. Egerton, Dr. M.H. Chen, Mr. R. Bhatnagar and Mr.J. Malinski who provided access to TEMs. I also acknowledge Ms. Tina Barker and Mr. Shiraz Merali for their help with SEM and XRD.

Table of Contents

Chapter 1. Introduction 1

Chapter 2. Metal-Semiconductor Contacts 5
  2-1 Properties of InP 5
  2-2 Applications of InP 6
  2-3 Metal-Semiconductor Contacts 9
    2-3-1 Schottky contacts 9
    2-3-2 Ohmic contacts 11
    2-3-3 Metal-semiconductor ohmic contact formation 18
    2-3-4 Techniques of improving contact quality 21
    2-3-5 Ohmic contacts to InP 22
  References 23

Chapter 3 Experimental Methods 36
  3-1 Film deposition 36
  3-2 Annealing 36
  3-3 XRD analysis 37
  3-4 Transmission electron microscopy (TEM) 37
  3-5 TEM specimen preparation 37
    3-5-1 Cross section specimen preparation 38
    3-5-2 Plan view specimen preparation 38
  3-6 EDX analysis 39
  3-7 Electron diffraction 39
    3-7-1 Selective area diffraction (SAD) 39
    3-7-2 Convergent beam electron diffraction (CBED) 40
  3-8 Phase identification 40
  3-9 contact resistance measurement 41
  References 42

Chapter 4. Interfacial Reactions between Ti Metallization and InP 44
  4-1 Ti-based ohmic contacts 44
    4-1-1 Ti metallizations 44
    4-1-2 Ti-semiconductor 44
    4-1-3 Ti-based metallizations 46
  4-2 Reaction between Ti and InP 53
    4-2-1 Experimental results and discussion 53
    4-2-2 Ti-In-P phase diagram 57
  4-3 Conclusion 57
  References 57

Chapter 5 Ohmic Contact Formation in Ge/Ni Metallization to n-type InP **71**
5-1 Ni-based metallizations- a literature review 71
  5-1-1 Ni/InP contact 71
  5-1-2 Au/Ge/Ni-GaAs contacts 74
  5-1-3 AuGeNi-InP contact 77
5-2 Reactions in Ni metallization to InP 81
  5-2-1 Experimental results and discussion 81
  5-2-2 Conclusions 87
5-3 Ge/Ni Metallizations to n-type InP 88
  5-3-1 Experimental results and discussion 88
  5-3-2 Conclusions 93
5-4 Relationship between electrical properties and microstructure 93
  5-4-1 Electrical properties 93
  5-4-2 Ohmic behavior and contact microstructure 94
References 94

Chapter 6 Summary and Recommendations **121**
6-1 Summary 121
6-2 Recommendations 122

List of Tables

Table 2-1 Properties of III-V compounds compared with Si, Ge (T=300°K) 24

Table 2-2 Work functions of some elements and electron affinity of some semiconductors 26

Table 4-1 Indexing of SAD pattern in Figure 4-10c 60

Table 4-2 Indexing of SAD pattern in Figure 4-12b 60

Table 5-1 AuGeNi contacts to GaAs 94

Table 5-2 AuGeNi contacts to InP 95

Table 5-3 Relationship between observed symmetries in CBED patterns and diffraction groups 96

Table 5-4 Relationship between diffraction groups and crystal point groups 97

Table 5-5 Six different cases of dynamic absences along a single systematic line of reflections 98

Table 5-6 Specific contact resistance of Ge/Ni-InP contact annealed at differen temperatures and times 98

List of Figures

Fig. 2-1 Calculated energy band structure of InP in two principal directions in the Brillouin Zone. The various critical point energies are indicated 27

Fig. 2-2 (a) Energy-band diagram of a metal and semiconductor before contact. (b) Ideal energy-band diagram of a metal-n-semiconductor junction for $\phi_m > \phi_s$ 27

Fig. 2-3 Ideal energy-band diagram of a metal-semiconductor junction (a) under reverse bias and (b) under forward bias 28

Fig. 2-4 Current-voltage characteristics of a Schottky contact 28

Fig. 2-5 Ideal energy-band diagram (a) before contact and (b) after contact for a metal-n-semiconductor junction for $\phi_m < \phi_s$ 29

Fig. 2-6 Ideal energy-band diagram of a metal-n-semiconductor ohmic contact (a) with a positive voltage applied to the metal and (b) with a positive voltage applied to the semiconductor 29

Fig. 2-7 Current-voltage characteristics of an ohmic contact 30

Fig. 2-8 Ideal energy-band diagram (a) before contact and (b) after contact for a metal-p-semiconductor junction for $\phi_m > \phi_s$ 30

Fig. 2-9 Energy-band diagram of a heavily doped n-semiconductor to a metal junction 30

Fig. 2-10 Band diagrams describing the Schottky theory of the metal-semiconductor interface. Four types of conduction are possible depending on the difference $\phi_m - \phi_s$ and the semiconductor type. The arrows indicate majority-carrier current flow 31

Fig. 2-11 Band diagram for a nonideal metal-semiconductor interface under forward bias V. An insulating layer of thickness δ exists between the metal and semiconductor and surface states are filled to level ϕ_o 32

Fig. 2-12 Measurement of the specific contact resistance r_c using the Cox-Strack method 32

Fig. 2-13 Measurement of the specific contact resistance r_c by the four-point method 33

Fig. 2-14 Measurement of the specific contact resistance r_c by the Shockley technique. The voltage applied to the coplanar ohmic contacts is V_a. The linear voltage distribution between the contacts is extrapolated to obtain the transfer length L_T 33

Fig. 2-15 Measurement of the specific contact resistance r_c by the transmission-line model (TLM) technique. R_e is the total resistance of the metal-semiconductor interface and the epitaxial layer under the contact 34

Fig. 2-16 A simple method of determining R_e using a linear array of unequally spaced ohmic contacts. The shaded regions are the contact areas 34

Fig. 2-17 Band bending for various semiconductor interfaces: (a) metal on n-InAs; (b) metal on n-InAs/GaAs and (c) metal on n-InAs on graded n^+-$Ga_xIn_{1-x}As$/GaAs 35

Fig. 3-1 Schematic of procedure for cross section specimen preparation: (a) sample piece; (b) "raft-like" structure; (c) a disc.(d) a disc after polishing 42

Fig. 3-2 Schematic presentation of procedure of plan view specimen preparation: (a) a specimen disc 3mm in diameter: (b) a disc dimpled from the semiconductor side 43

Fig. 4-1 Schematic illustration of alloying sequence of Pt/Ti metallization to p^+-GaAs 61

Fig. 4-2 Schematic representation of the layer composition and thickness of Pt (60 nm)/Ti (50 nm) contacts to InP, in the as-deposited conditions and after RTP at 300, 400, 450 and 500°C for 30 sec 61

Fig. 4-3 Schematic representation of the reactions that occur during annealing of Ti/Pt/Au contacts to InGaAs 62

Fig. 4-4 (a)Bright field micrograph of an as deposited cross section specimen showing that the thickness of Ti film is about 120 nm. (b) EDX spectrum of the as deposited Ti layer 63

Fig. 4-5 (a) Bright field micrograph of an as deposited plan view specimen showing that the grain size is approximate 25 nm. (b) SAD diffraction pattern from the as deposited plan view specimen showing the Ti film is <001> preferentially oriented 63

Fig. 4-6 Bright field micrograph of a cross section specimen annealed at 325°C for 5 minutes. Two regions, exhibiting different contrast are shown 64

Fig. 4-7 Ti-P phase diagram showing that solubility of P in Ti is very low 64

Fig. 4-8 Bright field micrograph of a cross section specimen annealed at 350°C for 2 hrs 64

Fig. 4-9 (a) Bright field micrograph of the inner layer (In) from a plan view specimen annealed at 350°C for 2 hrs. (b) Diffraction pattern and (c) EDX spectrum from (a) 65

Fig. 4-10 (a) Bright field micrograph of Ti-P compound from a plan view specimen annealed at 350 °C for 2 hrs. (b) EDX spectrum from the Ti-P compound, and (c) SAD pattern showing that the Ti-P compound is TiP 66

Fig. 4-11 Micrograph of a cross section specimen annealed at 450°C for 1.5 hrs 67

Fig. 4-12 (a) Micrograph of the Ti-P layer from the plan view specimen annealed at 450°C for 1.5 hrs. (b) SAD pattern from (a) indicates that the Ti-P compound is TiP 67

Fig. 4-13 Bright field image of Ti/Pt/Au-InP cross section specimen annealed at 400°C for 2 min 67

Fig. 4-14 (a) Bright field micrograph of the TiP layer from a plan view specimen annealed at 550°C for 30 min. (b) SAD pattern from (a) 68

Fig. 4-15 (a) Bright field image of a cross section specimen annealed at 550°C for 4 hrs. (b) Micrograph of the TiP layer from a plan view specimen annealed at 550 °C for 4hrs. (c) EDX spectrum from the grains of TiP and (d) SAD pattern from the region shown in (b) indicate that the Ti-P compound is TiP 68

Fig. 4-16 (a) Micrograph of a cross section specimen (the top of the film) annealed at 550°C for 4 hrs. (b) CBED pattern from the region shown in (a) indicating that In was oxidized to form In_2O_3 69

Fig. 4-17 Schematic representation of reactions between Ti films and InP substrate 70

Fig. 4-18 Predicted isothermal section of Ti-In-P phase diagram (<550°C) 70

Fig. 5-1 Schemematic model for the AuGeNi alloyed contact to InP, immediately after alloying (a) and after subsequent heat treatment at elevated temperatures for several hours (b) 99

Fig. 5-2 Schematic representation of reactions that occur in the Au (40 nm)/Ge (50 nm) Ni (25 nm) system during annealing 99

Fig. 5-3 Bright field (BF) micrograph from a cross section specimen of the as deposited sample. Also shown is an SAD pattern from a plan view specimen of the Ni layer 100

Fig. 5-4 BF micrographs of cross section specimens (a) annealed at 190°C for 15 min and (b) annealed at 250°C for 30 min. Also shown are EDX spectrum taken from the amorphous ternary layer (c) 100

Fig. 5-5 BF micrographs and EDX spectra from cross section specimens of a sample annealed at 250°C for 90 min. Note, that these micrographs are taken from different regions of the same specimen, indicating the non-uniform nature of the crystallization process 101

Fig. 5-6 BF micrograph from a plan view specimen of a sample annealed at 280°C for 5 min. Two distinct regions are shown, i.e., single crystalline Ni_2InP (upper left) and a polycrystalline Ni_2P/Ni_2InP mixed region (lower right) 102

Fig. 5-7 (a) BF micrograph of a plan view specimen annealed at 400°C for 15 min. CBED patterns (b) and (c) from (a) showing that two phases are present, Ni_2P and Ni_2InP 102

Fig. 5-8 BF micrograph and EDX spectra from different regions of a specimen annealed at 500°C for 20 min. The layer has become non-uniform and shows sign of agglomeration 103

Fig. 5-9 A schematic representation of reactions occurring during the annealing of Ni/InP 104

Fig. 5-10 CBED pattern from [001] orientation of Ni_2InP 105

Fig. 5-11 CBED pattern from [001] showing that spots line up in both the [100] and [010] directions 106

Fig. 5-12 Schematic drawings showing cases where a) the beam direction is parallel to the [001] direction and b) beam is perpendicular to the ZOLZ containing [100] and [010] g vectors 106

Fig. 5-13 Portions of two [001] oriented CBED patterns. The patterns show ZOLZ and FOLZ spots along the [010] direction. ZOLZ and FOLZ spots line up along the [010] direction in (a), but are slightly misaligned in (b) 107

Fig. 5-14 Schematic drawing showing how the angle β can be calculated from 3 coplanar reciprocal lattice vectors perpendicular to the [010] direction 107

Fig. 5-15 CBED patterns from [103] orientation of Ni_2InP. The pattern in (b) is taken with a smaller condenser aperture than the patterns in (a) and (c). The pattern in (a) gives the whole pattern symmetry (m); the pattern in (b) shows the ZOLZ symmetry (2mm); the pattern in (c) gives the zero order disc symmetry (m) 108

Fig. 5-16 CBED pattern from [$1\bar{3}\bar{5}$] orientation of Ni_2InP. The ZOLZ symmetry is 2, while the whole pattern symmetry is 1 108

Fig. 5-17 ZOLZ spots from [001] oriented CBED pattern from Ni_2InP. Alternate forbidden reflections are visible along the [010] direction at h= ±1,3,5,... 108

Fig.5-18 BF micrograph of an as-deposited cross section specimen showing the layer sequence: Ge/Ge-Ni/Ni/Ni-In-P/InP 109

Fig. 5-19 EDX spectra taken from each layer of an as deposited specimen: (a) outer layer of Ge, (b) Ge-Ni, (c) Ni and (d) the inner most layer of Ni-In-P 109

Fig. 5-20 (a) BF micrograph of Ge from an as deposited plan view specimen. (b) SAD pattern from Ge layer shown in (a) indicating that it is amorphous 110

Fig. 5-21 (a) BF micrograph of the Ge-Ni mixed layer from an as deposited plan view specimen. (b) SAD pattern from (a) (rings are from polycrystalline Ni and a diffuse ring from amorphous Ge) 110

Fig. 5-22 (a) BF micrograph of Ni layer from an as-deposited plan view specimen. InP is adjacent to Ni. (b) SAD pattern from the Ni layer shown in (a). Spots are from InP 111

Fig. 5-23 BF micrograph of a cross section specimen annealed at 250°C for 60s 111

Fig. 5-24 (a) BF micrograph of the GeNi layer from a plan view specimen annealed at 250°C for 60s showing that the grain size is 40-50nm. (b) SAD pattern from GeNi layer shown in (a) 112

Fig. 5-25 (a) BF micrograph of $Ge_{12}Ni_{19}$ layer from a plan view specimen annealed at 250°C for 60s showing that the grain size is ≈20nm. (b) SAD pattern from the $Ge_{12}Ni_{19}$ layer shown in (a) 112

Fig.5-26 BF micrograph of a cross section specimen annealed at 250°C for 120s 113

Fig. 5-27 (a) TEM image of a cross section specimen annealed at 250°C for 240 s. (b) TEM image of a cross section specimen annealed at 250°C for 480 s 113

Fig. 5-28 BF micrograph of a cross section specimen annealed at 350°C for 60s 113

Fig. 5-29 BF micrograph of a cross section specimen heated at 160°C for two minutes showing that the thickness of the amorphous ternary layer has increased relative to the as deposited sample 114

Fig. 5-30 (a) BF micrograph of the inner layer from a specimen annealed at 250°C for 90s, showing two regions, i.e., the amorphous region and a crystallized region with a nucleation site. 114

Fig. 5-30 (b) BF micrograph of the inner layer from a specimen annealed at 250°C for 90s, showing distribution of the nucleation sites 114
(c) micrograph of the inner layer from a specimen annealed at 250°C for 90s, showing a nucleation site 115

Fig. 5-31 BF micrograph of crystallized region with small grains showing that the growth of the grains is limited by their orientations 116

Fig.5-32 (a) Two sets of diffraction patterns and (b) computer simulations showing that the grain growth direction is $<0\bar{1}10>$ 116

Fig. 5-33. (a) BF micrograph of the textured single crystal sandwiched by a Ge-Ni layer and InP. (b) CBED diffraction pattern (ZA=[001]) from the textured single crystal and (c) EDX spectrum from the textured crystal 117

Fig. 5-34 Ge-In and Ge-Ni phase diagrams 118

Fig. 5-35 (a) BF micrograph of the GeNi layer from a plan view specimen annealed at 350°C for 60s. (b) SAD pattern from the layer shown in (a) 119

Fig. 5-36 (a) Micrograph of a cross section specimen annealed at 450°C for 60s. A rough InP interface and thick porous outer layer are visible. (b) EDX spectrum from the outer layer shown in (a), which contains mainly In as well as Ge and P 119

Fig. 5-37 Schematic representation of reactions between the Ge/Ni metallization and InP 120

Chapter 1

Introduction

The primary application of InP in the semiconductor industry is for the fabrication of optoelectronic devices and lightwave devices. This is based on its direct band gap characteristics and unique combination of electrical and optical properties, such as high electron mobility, high saturation velocity and radiation tolerance.

Metal semiconductor contacts play an important role in the development of very large scale integration (VLSI) devices and their operation. During device operation, metal/contacts provide communication links between the external circuit and the active regions of semiconductor devices. According to current-voltage characteristics, contacts are divided into two categories. One is Schottky barriers or rectifying contacts, where, for an n-type semiconductor, the majority carrier electrons flow more easily from the semiconductor into the metal if forward bias is applied. The forward-bias current is in the direction from metal to semiconductor; it is an exponential function of the forward-bias voltage. The other type of contact is ohmic contacts, in which the current is a linear function of the applied voltage. Most ohmic contacts are basically Schottky barriers, where a high doping level is introduced into the semiconductor, narrowing the barrier, so that majority carriers can tunnel through the barrier. Introducing an external dopant diffusion source and driving the dopant into the semiconductor, by subsequent annealing or epitaxially growing a thin layer with a high dopant level, are the most conventional ways to form ohmic contacts to InP-based devices. The dopants usually used include Si and Ge for n-type III-V compound semiconductors or Zn and Be for p-type III-V compound semiconductors.

Ohmic contacts to InP-based materials are essential for electronic devices such as field effect transistors (FET), junction field effect transistors (JFET), high electron mobility transistors (HEMT) and heterojunction bipolar transistors (HBT), and lightwave devices such as long wavelength laser diodes and light-emitting diodes (LED). Further scaling in size puts ever-increasing demands on contact performance, since the operation of large scale integrate circuits operate under high currents and at elevated temperatures. The main requirements for ohmic contacts are low contact resistance and good thermal stability, which are directly affected by the contact microstructure as well as the uniformity of the metal/semiconductor interface. It is essential to understand the relationship between microstructures of contacts and electrical properties. Many experimental results for contact microstructure and electrical properties have been reported and almost all the modern materials science research techniques have been utilized for characterization, including Auger electron spectroscopy (AES), x-ray photoelectron spectroscopy (XPS) and ultraviolet photoelectron spectroscopy (UPS), scanning electron microscopy (SEM), x-ray diffraction (XRD), transmission electron microscopy (TEM) and electron energy dispersive spectroscopy (EDX). The result is a range of characterization results, in terms of interfacial reactions, products, contact morphology and electrical properties. TEM combined with EDX is one of the most powerful techniques to analyze the microstructural changes that occur during annealing. It allows direct observation of interfaces and provides high spatial resolution information on both crystal structures and chemical composition. TEM electron diffraction makes it possible to reveal crystal structure in three dimensions. However, TEM requires high quality plan view and cross section specimens in order to provide adequate analysis of the contact structure. This is particularly difficult for InP-based materials. Very few groups have reported successful work using TEM analysis, although hundreds of articles have been published on contacts to InP.

In this study, three contact systems are systematically investigated, i.e., Ti/InP, Ni/InP and GeNi/InP systems.

Titanium is an important constituent in multicomponent metallizations to InP and InP-based compound semiconductors, such as InP, InGaAs and InGaAsP. Ti/Pt and Ti/Pt/Au, are commonly used for ohmic contacts to both n-and p-type materials [1-5]. The primary role of Ti in these contacts is to provide improved metallization adhesion; it is in contact with the underlying semiconductor. Many efforts have been made to correlate electrical properties with microstructure, however, very little has been done to characterize in detail the reactions at the Ti/semiconductor, particularly InP, interface. The only detailed study of microstructural changes which occur during annealing is one on Ti/Pt/Au contacts to InGaAs, using TEM [5]. Another study was done on thin Ti metallizations (<3nm) to <110> InP, using x-ray photoelectron spectroscopy (XPS) and ultraviolet photoelectron spectroscopy (UPS) [6]. However, in these studies the reactions between Ti and InP were insufficiently characterized due to the disadvantages of the analysis techniques utilized.

The main purpose for studying the Ti/InP system is to identify interfacial reactions occurring during annealing of Ti metallizations on InP, and to achieve phase identification through the use of transmission electron microscopy (TEM) techniques, i.e., imaging, electron diffraction and energy dispersive x-ray (EDX) microanalysis.

Nickel is also a common metal in ohmic contacts to InP. This is because not only does Ni provide good adhesion to InP, but Ni_2P, one of the reaction products between Ni and InP, exhibits low specific resistance on n-InP ($r_c=3x10^{-6}\ \Omega cm^2$ for an original doping level of $2x10^{18}\ cm^3$). Different reaction products between Ni and InP have been reported, i.e., a hexagonal ternary phase ($Ni_{2-3}InP$), which formed prior to Ni_2InP (monoclinic) formation, and Ni_3P, which formed during annealing ($\cong 400^0C$) before decomposing to Ni_2P [7].

Even though Ni is used in metallizations to InP, the reactions between thin layers of Ni and InP have not been well characterized, especially at low temperatures. Several studies have been done on the Ni/InP system [7-13], but a comprehensive study on thin film reactions is lacking.

The purpose of the systematic study of the Ni/InP system is to characterize more completely the reaction products that form during low temperature annealing ($\leq 500^oC$) of Ni/InP thin film diffusion couples. In particular, the initial stages, i.e., the formation of an amorphous ternary phase (Ni_xInP) and the subsequent crystallization of this phase, are studied in detail. The reactions are characterized using primarily transmission electron microscopy (TEM) techniques, with corroboration from x-ray diffraction (XRD). Phases are identified through a combination of energy dispersive x-ray analysis (EDX), selected area diffraction (SAD) and convergent beam electron diffraction (CBED).

It is crucial for an ohmic contact to possess low contact resistance and high thermal stability in order to meet the ever increasing requirements of high current density and elevated temperature during device operation. Ni-based contacts to InP have been widely studied, particularly Au/Ge/Ni metallizations to n-type InP, which is the most common contact structure to n-type InP. This structure is based on a successful contact to n-type GaAs, where Au is added to NiGe-based ohmic contacts in order to improve the contact resistance. Low contact resistances ($\approx 10^{-7}\Omega\ cm^2$) [14] are attainable for Au/Ge/Ni contacts to n-type InP for annealing temperatures of the order of 400-425°C. However, these contacts exhibit poor thermal stability and lateral uniformity, due to Au inward diffusion and In outward diffusion, which results in the formation of Au-In compounds both at the metallization/semiconductor interface and the metallization surface [15]. In this study, the Au layer is removed from the deposition scheme, in an attempt to improve contact morphology and reliability.

This thesis is organized into six chapters. Chapter 2 is a comprehensive literature review including the principles of ohmic contact formation, properties of InP and the methods of specific contact resistance measurement. Chapter 3 describes the experimental procedures involved in the preparation of the metallzation systems, i.e., Ti/InP, Ni/InP and

Ge/Ni-InP, and the analysis methods, such as specimen preparation and the use of TEM and its related techniques, utilized in this study. The initial portion of of Chapter 4 presents a literature review of Ti-based contacts and then presents the experimental results and discussion of the interfacial reactions that occur in Ti/InP system during annealing. A brief summary ends this chapter. As in Chapter 4, Chapter 5 starts with a literature review about Ni and Ni-based metallizations to GaAs and InP and related semiconductors, this is followed by experimental results and discussion of the interfacial reactions that occur in the Ni/InP system during annealing. Interfacial reaction characterization and discussion of the Ge/Ni-InP system are presented in the latter part of this chapter, followed by discussion of the relationship between microstructure and electrical properties. The final chapter, summarizes the results of this work and discusses possible directions for future work.

References

1. A. Katz, B.E. Weir, S.N.G. Weir, S.N.G. Chu, P.M. Thomas, M. Solder, T. Boone and W.C. Dautremout-Smith, *J. Appl. Phys.* Vol. 67, 3782 (1990).
2. A. Katz, B.E. Weir and W.C. Dautremont-Smith, *J. Appl. Phys.* Vol. 68, 1123 (1990)
3. A. Katz, S.N.G. Chu, B.E. Weir, C.R. Abernathy, W.S. Hobson, S.J. Pearton and W. Savin, *IEEE Trans. Electr. Devices* Vol. 39 184 (1992).
4. S.N.G. Chu, A. Katz, T. Boone, P.M. Thomas, V.G. Riggs, W.C. Dautremont-Smith and W.D. Johnoson Jr, *J. Appl. Phys.* Vol. 67, 3754 (1990) .
5. D.G. Ivey, P. Jian, R. Bruce and G. Knight, *J. Mater. Sci.: Mater. in Electron.* Vol. 6, 219 (1995).
6. Mingrong Ji, Uianxin Wu, Maosheng Ma and Xianming Liu, *Vacuum* Vol. 43 1157 (1992).
7. T. Sands, C.C. Chang, A.S. Kaplan, V.G. Keramidas, K.M. Krishnan and J. Washburm, *Appl. Phys. Lett.* Vol. 50, 1346 (1987).
8. A. Appelbaum, M. Robbins and F. Schrey, *IEEE Ttrans. Electr. Devices* , Vol. ED-34, 1026 (1987).
9. A. Appelbaum, P.M. Thomas and P. A. Baarnes, in *Semiconductor-Based Heterosturctures: Interfacal Structure and Stability*, M.L. Green, E.E. Baglin, G.Y. Chin, H.W. Deckman, W. Mayo and D. Narasinham Eds, The Metallurgical Society, Inc. 409, (1986).
10. N.S. Fatemi and V.G. Weizer, *J Appl. Phys.* Vol. 73, 289 (1993).
11. G. Stremsdierfer, Y. Wang, J.R. Martin and E. Souteyrand, *Mat,Res. Soc. Symp. Proc.*, Vol. 260, 543 (1992).
12. S.E. Mohney and Y.A. Chang, *Mat. Res. Soc.Symp. Proc.* Vol. 337. 393-398 (1994).
13. S.E. Mohney and Y.A. Chang, *J. Mater. Res.* Vol. 7, 955 (1992).
14. D.G. Ivey, D. Wang, D. Yang, R. Bruce and G. Knight, *J. Electr. Mater.* Vol. 23, 441 (1994).
15. Douglas G. Ivey and Ping Jian, *Canadian Metallurgical Quarterly*, Vol. 34, No.2, 85-113, 1995.

Chapter 2

Metal-Semiconductor Contacts

Semiconductors are a group of materials having electrical conductivities intermediate between metals and insulators. The electrical resistivity values of semiconductors are defined in the range between 10^{-2} and 10^{9} Ω-cm. The conductivity of semiconductors can vary over orders of magnitude through changes in temperature, optical excitation, and impurity content.

Semiconductor materials are also classified as either elemental semiconductors, which are found in column IV and neighboring columns of the Periodic Table, or compound semiconductors, which are made up of certain combinations of elements from column III and column V or column II and column VI. InP is an example of a III-V compound semiconductor.

2-1 Properties of InP

The crystal structure of InP is zinc blende type (sphalerite structure). This consists of two interpenetrating fcc lattices, one shifted by *a*/4[111] relative to the other fcc lattice - *a* being the fcc lattice parameter. The two fcc lattices are occupied by In and P respectively.

InP is a direct band gap semiconductor. There are two classes of energy bands: direct and indirect. If the band structure of a semiconductor has a minimum in the conduction band and a maximum in the valence band for the same **k** (propagation constant) value (**k**=0), it is called a direct energy band. A semiconductor with a direct energy band is called a direct band gap semiconductor. In a direct band gap semiconductor, an electron in the conduction band can fall to an empty state in the valence band, giving off the energy difference E_g as a photon of light. Since the periodicity of most lattices is different in various directions, the (E,**k**) diagram must be plotted for the various crystal directions.

If the valence energy maximum is at a different **k** value from that of the conduction energy band minimum, a transition from the minimum point in the conduction band to the maximum point of the valence band (indirect transition) requires some change in **k**, i.e., a change of momentum for the electron. This energy band is called an indirect energy band, and gives rise to an indirect band gap semiconductor.

The calculated energy band structure of InP is shown in Figure 2-1 [1]. Both the valence band maximum and the lowest conduction band minimum occur at k = 0, the Γ point. The conduction band is derived from s-like orbitals and denoted by the representation Γ_1. The lowest conduction band minimum is at k=0. Higher conduction band minima occur in the <100> (Δ) and <111> (Λ) directions, at k=X and k=L. The difference in energy between the lowest conduction band minimum and the higher conduction band minima are 0.40 eV and 0.7 eV [1], respectively. Γ_{15} in the figure represents the valence band. The valence band maxima are derived from the p-like orbitals p_x, p_y and p_z, which remain degenerate under the tetrahedral group of the zinc blende lattice. There are six states in the valence band, which are further split by spin-orbit interaction into a four fold degenerate state and a two fold degenerate state. The lowest band corresponds to the two fold degenerate state. The four fold state refers the highest valence bands called the light hole and heavy hole bands. The value of the spin-orbit splitting for InP is 0.11eV [2], which is shown in the figure. The degeneracy of the heavy and light bands will be further split if they are subjected to a shear component of a strain applied uniaxially to the semiconductor.

InP has become an important semiconductor material because of its unique combination of electrical and optical properties. The properties of several III-V compounds, including InP, are listed in Table 2-1.

2-2 Applications of InP

The compound semiconductors are widely used in devices requiring the emission or absorption of light. Light-emitting diodes (LEDs), for example, are commonly made of GaAs, GaP and mixed compounds such as GaAsP. Fluorescent materials usually are II-VI compound semiconductors such as ZnS. Light detectors are commonly made with InSb, CdSe, or other compounds such as the lead salts, e.g., PbSe. An important microwave device, the Gunn diode, is usually made from GaAs, as are semiconductor lasers.

For high-speed electronic devices, it is desirable for a semiconductor to have high electron mobility and high saturation velocity, high thermal conductivity and high breakdown fields. InP meets all of these requirements [8,9].

InP-based materials are essential for and widely used in the semiconductor industry. The primary use of InP and its alloys with Ga and As is in the fabrication of optoelectronic devices or lightwave devices for optical fiber communication, such as long-wavelength laser diodes, light-emitting diodes (LED) [10,11], photodetectors, and solar cells [12], as well as high speed microelectronic devices, such as field effect transistors (FET) [13,14], junction field effect transistors (JFET) [2], high electron mobility transistors (HEMT), and heterojunction bipolar transistors (HBT)[15].

Compared with Si and GaAs, InP is far superior in a radiation environment due to its higher tolerance to radiation [16].

The disadvantiges of InP, such as its higher fragility, lower thermal stability and increased sensitivity to ion-induced damage compared with Si and GaAs, limit its application to industry and make it not as widely used as Si or GaAs. Ion implantation damage removal from InP and dopant activation steps for InP are more complex than for Si due to the binary nature of the InP lattice [16]. Amorphization of the In-based semiconductor is a problem in attaining the best electrical activation. Decomposition of InP and incongruent evaporation of P from the sample surface upon high temperature annealing is another problem for InP. In addition InP and its alloys are more expensive than Si and GaAs [17].

2-3 Metal-Semiconductor Contacts

Metal/semiconductor contacts are electrical communication links between the active regions of semiconductor devices and the external circuit. When a metal and a semiconductor are brought together, there exists an energy barrier to electron transport from the semiconductor side to the metal side at the metal/ semiconductor interface, due to the difference in work function between the metal and semiconductor. According to their current-voltage characteristics, contacts can be divided into two categories. The first type is a Schottky barrier or rectifying contact, which has a high contact resistance with respect to the electronic device. The other is an ohmic contact, which has a linear current-voltage characteristic due to a small contact resistance relative to the device resistance.

2-3-1 Schottky contacts

The ideal energy-band diagram for a metal and n-type semiconductor, before making contact, is shown in Figure 2-2a [5]. The vacuum level is used as a reference level. The parameter ϕ_m is the metal work function (measured in volts). ϕ_s is the semiconductor work function and χ is known as the electron affinity. The work function of various metals are given in Table 2-2 [5]. In Figure 2-2a, $\phi_m > \phi_s$ is assumed and the semiconductor is n-type. The ideal equilibrium metal-semiconductor energy band diagram, for this situation, is shown in Figure 2-2b. Before contact, the Fermi level in the semiconductor was above that in the metal. In order for the Fermi level to become a constant throughout the system in equilibrium, electrons from the semiconductor flow into the lower energy states in the metal. Positively charged donor atoms remain in the semiconductor creating a space charge region. The parameter ϕ_{Bn} is the barrier height of the semiconductor contact, i.e., the potential barrier seen by electrons in the metal trying to move into the semiconductor. This barrier is known as the Schottky barrier and is given by

$$\phi_{Bn} = (\phi_m - \chi) \tag{2-1}$$

On the semiconductor side, V_{bi} is the built-in potential barrier. This barrier is given by

$$V_{bi} = \phi_{Bn} - \phi_n \tag{2-2}$$

which indicates that V_{bi} is slightly dependent on semiconductor doping.

If a positive voltage (reverse bias) is applied to the semiconductor with respect to the metal, the semiconductor-to-metal barrier height increases, while ϕ_{Bn} remains constant in this idealized case. On the other hand, if a positive voltage is applied to the metal with respect to the semiconductor (forward bias), the semiconductor-to-metal barrier V_{bi} is reduced, while ϕ_{Bn} again remains essentially constant. In this situation, electrons can more easily flow from the semiconductor into the metal since the barrier has been reduced. The energy-band diagrams for the reverse and forward bias are shown in Figures 2-3a and 2-3b [5], where V_R is the magnitude of the reverse-bias voltage and V_a is the magnitude of the forward-bias voltage. The current-voltage characteristics are shown in Figure 2-4.

In most cases, metals will form rectifying contacts to n-type semiconductors. The same is true for metal/p-semiconductor contacts.

2-3-2 Ohmic contacts

Ohmic contacts are metal-to-semiconductor contacts, which are not rectifying contacts. An ohmic contact is a low-resistance junction providing conduction in both directions between the metal and the semiconductor. Ideally, the current through the ohmic contact is a linear function of applied voltage and the applied voltage should be very small. Two general types of ohmic contacts are possible. The first type is the ideal nonrectifying barrier and the second type is the tunneling barrier. A specific contact resistance is used to characterize ohmic contacts.

a. Ideal nonrectifying barriers

Figure 2-5 [5] shows an ideal contact to an n-type semiconductor for the case where $\phi_m < \phi_s$. In Figure 2-5a, energy levels before contact are shown and, in Figure 2-5b, the barrier after contact under equilibrium conditions is shown. To achieve thermal equilibrium in this junction, electrons will flow from the metal into the lower energy states in the semiconductor, which makes the surface of the semiconductor more n-type. The excess electron charge in the n-type semiconductor exists essentially as a surface charge density. If a positive voltage is applied to the metal (Figure 2-6a), there is no barrier to electrons flowing from the semiconductor into the metal. If a positive voltage is applied to the semiconductor (Figure 2-6b) [5], the effective barrier height for electrons flowing from the metal into the semiconductor will be approximately $\phi_{Bn} = \phi_n$, which is fairly small for a moderately to heavily doped semiconductor. For this bias condition, electrons can easily flow from the metal into the semiconductor. This junction, then, is an ohmic contact. The current -voltage relationship of ohmic contacts is almost linear as shown in Figure 2-7 [18].

For a p-type semiconductor, an ideal nonrectifying contact can be made if $\phi_m > \phi_s$, as shown in Figure 2-8 [5]. When contact is made, electrons from the semiconductor will flow into the metal to achieve equilibrium, leaving behind more empty states, or holes. The excess concentration of holes at the surface makes the surface of the semiconductor more p-type. Electrons from the metal can readily move into the empty states in the semiconductor. This charge movement corresponds to holes flowing from the semiconductor into the metal. Holes in the metal can also be visualized as flowing into the semiconductor. This junction is also an ohmic contact.

b. Barrier Tunneling

The space charge region width in a rectifying metal-semiconductor contact is inversely proportional to the square root of the semiconductor doping. The width of the depletion region decreases as the doping concentration in the semiconductor increases. Thus, the probability of tunneling through the barrier increases as the doping concentration increases.

Figure 2-9 [5] shows a junction in which the metal is in contact with a heavily doped n-type epitaxial layer [5]. The portion of the energy-band diagram to the right of the metal represents the epitaxial layer and the semiconductor substrate it connects. Electrons tunneling through the narrow depletion region are indicated by the arrows. In a heavily doped semiconductor, the depletion width is on the order of angstroms. For this type of barrier width, tunneling may become the dominant current mechanism. The tunneling current has the form

$$J_t \propto \exp(-e\,\phi_{Bn} / E_{oo}) \qquad (2\text{–}3)$$

where $$E_{oo} = e\hbar/2\,(N_d / \varepsilon_s m_n^*)^{1/2} \qquad (2\text{-}4)$$

e is the electronic charge, $\hbar$ is the modified Planck s constant ($h/2\pi$), N_d is the density of donor impurity atoms (cm^{-3}), ε_s is the permittivity of the semiconductor (F/cm^{-2}) and m_n^* is the effective mass of an electron. The tunneling current increases exponentially with doping concentration.

It should be pointed that Eq.(2-1) is referred to as the Schottky limit, which states that the barrier ϕ_B is directly proportional to the metal work function ϕ_m. It seems that Schottky theory should predict the four possible cases shown in Figure 2-10 [19]. By simply choosing a metal with the appropriate work function, one could obtain a rectifying diode or an ohmic contact. However, Schottky diodes formed on many of the III-V semiconductors do not show this behavior. Experimentally, it is found that for most III-V semiconductors, ϕ_B is almost independent of the metal used to form the contact. The Schottky limit of Eq.(2-1) is not a complete description.

ϕ_B would be independent of ϕ_m if surface states (electronic states) existed at the metal-semiconductor interface in sufficient numbers [20]. Surface states are localized at the surface of the semiconductor crystal and are produced by the interruption of the perfect periodicity of the crystal lattice. The states can be occupied or empty depending on the position in energy relative to the Fermi level at the surface. For convenience, a neutral level ϕ_0 is defined as the energy level to which the surface states are neutrally filled. If the states are filled to an energy greater than ϕ_0, the surface possesses a net negative charge and the states are acceptor-like in behavior; if the states are filled to a level below ϕ_o, the surface has a net positive charge and the states behave in a donor-like manner. If the number of surface states is large, then the Fermi level at the surface of the semiconductor will be at ϕ_o, since the charge in the surface states will fully accommodate the necessary potential difference. Thus, no change in the charge within the depletion region of the semiconductor is necessary when a metal is brought into contact with the semiconductor. Hence, ϕ_B is independent of ϕ_m. E_F^s at the surface of the semiconductor is then the same as in the metal E_F^m and one has

$$\phi_B = E_g - \phi_o \qquad (2\text{-}5)$$

This implies that the Fermi level is ≡pinned or ≡stabilized by the surface states to an energy ϕ_0 above the valence band. Eq. (2-5) is known as the Bardeen limit.

In general the value of the barrier energy ϕ_B for nonideal metal-semiconductor interfaces will be somewhere between the Schottky limit (Eq.(2-1)) and the Bardeen limit (Eq.(2-5)). It can be described as [8]

$$\phi_B^{\,o} = \gamma(\phi_m - \chi_s) + (1 - \gamma)(E_g - \phi_o) \qquad (2\text{-}6)$$

where $$\gamma = \varepsilon_i / (\varepsilon_i + qN_{ss}\delta) \quad (0 \le \gamma \le 1) \qquad (2\text{-}7)$$

The metal-semiconductor interface is shown in Figure 2-11 [19], where the semiconductor is n-type and has permittivity ε_s. The interfacial layer has thickness δ; permittivity ε_i; and the surface states are characterized by density qN_{ss} (per unit area per unit energy) and neutral level ϕ_o. Thus Schottky diodes formed on such surfaces exhibit values of ϕ_B, which are independent of the metal employed as well as the electron affinity of the semiconductor.

c. Barrier energy of InP

The barrier energy of InP is larger on p-type InP than on n-type InP, which is just the opposite from that of GaAs. The metal work function is not the dominant controlling parameter in metal/InP interface formation [19].

Chemical effects play an important role in determining ϕ_B [21]. For several metals on atomically clean n-type InP, there is a systematic dependence of ϕ_B on the reactivity of the metal with the InP. Metals (Ni, Fe and Al) which form compounds with phosphorus, that are significantly more stable than InP, yield contacts with low barrier energies and ohmic behavior. Metals (Au, Ag and Cu) which form phosphides that are less stable than InP yield Schottky diodes with ϕ_{Bn} ~0.5eV. Reactive metal-InP diodes exhibit an abrupt interface and In-rich outdiffusion, while unreactive metal-InP diodes exhibit diffuse interfaces and P-rich outdiffusion [22]. The work function of the metal is unimportant for Schottky diodes formed on n-type InP and microscopic chemical effects are dominant during metal/InP interface formation. On the other hand, the chemical effects are less pronounced on etched surfaces than on atomically clean surfaces.

d. Specific contact resistance

A specific contact resistance is used to characterize ohmic contacts. The specific contact resistance r_c is defined as the reciprocal of the derivative of current density with respect to voltage evaluated at zero bias. It can be written as

$$r_c = (\partial J / \partial V)^{-1} |_{V=0} \quad \text{(ohm-cm}^2\text{)} \qquad (2\text{-}8)$$

For an ohmic contact, r_c should be as small as possible.

For a rectifying contact with a low to moderate semiconductor doping concentration, thermionic emission current is dominant across the junction. The specific contact resistance for this case is

$$r_c = [\,(kT/e)\exp(+e\,\phi_{Bn}/kT)] / A^*T^2 \qquad (2\text{-}9)$$

where ϕ_{Bn} is the Schottky barrier height (V). The specific contact resistance decreases rapidly as the barrier height decreases.

In the case of a metal-semiconductor junction with a high impurity doping concentration, the tunneling process will dominate. Eq. (2-3) and (2-4) should be used to derive the specific contact resistance, i.e.,

$$r_c \propto \exp\{[+2(\varepsilon_s m_n^*)^{1/2}/\hbar\,].\,[\phi_{Bn}/(N_d)^{1/2}]\} \qquad (2\text{-}10)$$

which shows that the specific contact resistance is significantly dependent on semiconductor doping.

e. Measurement of the specific contact resistance, r_c

Several methods have been used to measure the specific contact resistance r_c. For a homogeneous contact of area A having uniform current density, the contact resistance R_c is

$$R_c = r_c / A \qquad (2\text{-}11)$$

R_c is approximately equal to R, which can be obtained by experimental measurement, when r_c P 10^{-2} cm^2. For smaller values of r_c, two factors have to be taken into account, i.e., R_b, the spreading resistance of the semiconductor and R_0, the series resistance of the semiconductor substrate and connecting wires, so that $R = R_c + R_b + R_0$. R_b and R_0 also depend on the particular geometry of the metal-semiconductor.

For III-V semiconductors, r_c can be determined accurately using one of the four methods: (1) the technique of Cox and Strack, (2) the four-point method, (3) the Shockley extrapolation technique, or (4) the transmission-line model [23].

(i) Cox-Strack Method

Figure 2-12 schematically shows the method of Cox and Strack [24]. The resistance of a circular contact of radius a on an n-type film of resistivity ρ and thickness t needs to be determined. The current flow pattern is axial, through the layer to the heavily doped n^+ substrate. The spreading resistance for the layer is

$$R_b = (\rho / a)\, F \tag{2-12}$$

where F is a function of the ratio a / t and was found experimentally by Cox and Strack to have the approximate form

$$F\,(a/t) \approx (1/\pi)\, \arctan\, (2t/a) \tag{2-13}$$

With F (a/t) known,

$$R= (r_c / \pi a^2) + (\rho / a)\, F + R_0 \tag{2-14}$$

The form of the Eq.(2-14) can be changed to

$$R - R_b = (r_c / \pi)(1/a^2) + R_o \tag{2-15}$$

where R_b can be calculated using Eq.(2-12).

It is obvious that R- R_b has a linear relationship with $1/a^2$. In practice, the resistance r_c is realized by measuring a series of contacts with different areas resulting in a plot of R - R_b vs. $1/a^2$. The slope of the plot is r_c / π and the intercept is R_0.

This structure requires metallization of both the back and the front surfaces of the semiconductor wafer, and can be used for either p- or n-type material and for epitaxial or bulk layers. For bulk layers, t is the thickness of the wafer.

(ii) Four-Point Method [25, 26]

This method is schematically shown in Figure 2-13 [23]. t is the thickness of the layer being contacted which can be an epitaxial layer on a nonconducting substrate or a uniformly doped bulk wafer. The spreading resistance R_b for radial current flow from a circular contact of radius a is given in the form of an infinite series [27]. The spreading resistance must be first calculated and separated from the total resistance measured. R_b depends on r_c as well as ρ, because the current is nonuniformly distributed across the contact area. R_b is less than 0.12 R_c [27] and thus the contribution of R_b to R can be ignored, if

$$\rho a^2 \; . \; r_c t \qquad (2\text{-}16)$$

This equation can be satisfied by choosing a and t, because the ratio ρ / r_c is almost independent of the doping concentration for ohmic contacts to GaAs and InP. The expression for the contact resistance was proposed as [26]

$$r_c = \pi a^2 \{ V_1 /I - (V_2 /I)[\ln(3s/2a-1/2)]/2\ln 2 - R_b \} \qquad (2\text{-}17)$$

where $a << s$ and $t << s$ is assumed. R_b can be neglected if Eq.(16) is satisfied. V_1 and V_2 are experimentally measured for a known current I. The four-point method for measurement of r_c requires metallization of only one surface of the wafer.

(iii) Shockley Technique [28, 29]

This technique can be used for evaluation of ohmic contacts to thin semiconductor layers on nonconducting substrates. As shown in Figure 2-14 [23], R_s is the sheet resistance. The current produced by V_a is nonuniformly distributed through the two contacts and the epitaxial film. There is a current crowding under each contact. The potential distribution under the contact is $V(x) = V_0 \exp(-x/L_T)$ [29], where L_T (transfer length) = $(r_c / R_s)^{1/2}$, which can be obtained by extrapolating the linear voltage drop measured between the two contacts. V_0 is the extrapolated voltage appearing across the contact. r_c is found from equation $r_c = R_s L_T^2$. Accuracy of the measurement of the minimum value of r_c is dependent on the error in determination of L_T. Assuming L_T could be measured to within ± 1μm, it should be possible to measure r_c down to about 5×10^{-7} Ω-cm^2 with ± 25% accuracy for ohmic contacts to n-type GaAs;

(iv) Transmission-Line Model (TLM) [30, 31]

The TLM method is also used to determine the resistance of ohmic contacts applied to a thin III-V semiconductor layer on a nonconducting substrate. The method is shown in Figure 2-15 [23], in which a planar contact is treated as a resistive transmission line with uniform sheet resistance R_s and specific contact resistance r_c. The total resistance R_e of the contact and the epitaxial layer under the contact is found to be [31]:

$$R_e = [\,(r_c R_s)^{1/2} / W\,] \coth [\, d(R_s/r_c)^{1/2}\,] \tag{2-18}$$

Usually $d(R_s/r_c)^{1/2} \geq 2$, thus R_e can be approximately expressed as

$$R_e = [\,(r_c R_s)^{1/2} / W] \tag{2-19}$$

R_e can be experimentally determined using the arrangement in Figure 2-16 [23], where three identical ohmic contacts are spaced at unequal distances l_1 and l_2 along the surface of the layer. If R_1 and R_2 are the resistances measured, one can easily show that

$$R_e = (-R_2 l_1 + R_1 l_2) / [2(l_2 - l_1)] \tag{2-20}$$

Relating Eq.(19) with (20) one has

$$R_e \sim (r_c R_s)^{1/2} / W$$

or

$$r_c = R_e^2 W^2 \;/ R_s \tag{2-21}$$

Substituting the experimental results for R_1 and R_2 into Eq.(20), one can obtain R_e and r_c from Eq.(2-21).

It should be pointed out that the errors in measurement of l_1 and l_2 in Figure 2-16 affect the accuracy of the TLM method. Values of r_c of less than 10^{-7} Ω-cm^2 have been measured for contacts to Si.

The advantage of using TLM is that it avoids measuring the V(x) distribution of the Shockley method. However, both methods assume that the sheet resistance between and under the contacts is identical and that the semiconducting layer is infinitely thin. In the alloyed ohmic contacts used in FETs, during contact formation, interdiffusion of the metal and semiconductor layers result in significant alteration of the sheet resistance under the contacts. In this case the finite thickness of the semiconducting layer has to be taken into account. Separately determining the sheet resistance between the contacts and under the contacts has been achieved [32]. In many cases, it is not possible to separate the sheet resistance, thus R_e is more commonly used than r_c as a measure of the quality of the ohmic contacts in III-V FET structures.

2-3-3 Metal-semiconductor ohmic contact formation

According to the theory of forming ohmic contacts, a low barrier and/or a highly doped semiconductor are necessary. It is difficult to fabricate good ohmic contacts on wide band gap materials, because low barriers are not possible on these materials. From a practical point of view, ohmic contacts are basically metal-semiconductor Schottky barriers, through which a majority of the carriers can tunnel because of the narrow barrier width, enhanced by high dopant concentration in the interface region. These interfaces are characterized by fairly low Schottky barrier heights (0.4eV), which is reflected in almost a linear relationship between the measured current and the voltage applied across the contact [33, 34].

Many unique methods have been developed to form ohmic contacts. Great efforts were made to explore the relationship between the contact formation techniques and the interface behaviourof metal / III-V semiconductor systems. Since much more work has been done on GaAs and GaAs-based materials than on InP, and the techniques developed for GaAs are likely applicable to the InP cases, the following is not limited in to InP contacts. It is significant to understand the important roles played by the contact formation technique in improving contact thermal stability, surface morphology and specific contact resistance.

a. Contacts on heavily doped semiconductors

This is the most common method of forming ohmic contacts. Field emission or tunneling dominates current flow in contacts to heavily doped ($10^{18}cm^{-3}$-$10^{20}cm^{-3}$) semiconductor surfaces leading to a low r_c value. Doping levels near the dopant solubility limit of ~10^{20} cm^{-3} have been utilized in order to achieve better ohmic contact resistance in various metallization systems. Based on the doping method, contacts can be divided into two types.

(i) Nonalloyed ohmic contacts

These are formed by incorporating a high concentration of dopants into a grown epitaxial semiconductor layer. The method does not require a heating cycle to enable the migration of the dopants into the semiconductors [35] and thus contacts that are processed onto such materials are frequently referred to as nonalloyed ohmic contacts. Katz *et al* [36], for example, doped p-GaAs with C up to a surface concentration of $5x10^{20}$ cm^{-3} prior to Pt/Ti deposition to obtain a specific contact resistance as low as $8x10^{-7}\Omega$-cm^{2}.

(ii) Alloyed contacts

These contacts are formed by introducing an external dopant diffusion source, from which the dopants will be driven into the semiconductor during heating. This approach requires thermal activation in order to form the heavily doped intermixed interfacial layer, and thus contacts to these layers are termed alloyed contacts. Shealy and Chinn used a combination of Zn and In diffusion to obtain p doping of $\sim 10^{20}$ cm^{-3} in GaAs prior to a refractory metallization, which led to a specific contact resistance of $2\text{x}10^{-7}\ \Omega\text{-cm}^2$. A similar aproach using Zn diffusion into GaAs has been reported [37, 38]

These two approaches differ from each other by the kind and geometry of the metal-semiconductor interfacial related layers. The methods are widely used in the manufacturing of ohmic contacts to InP-based devices. The surface doping concentration in the semiconductor may be limited to the impurity solubility, which is approximately $5\text{x}10^{19}$ cm^{-3} for n-type GaAs [16]. Nonuniformities in the surface doping concentration may also result in failure to reach the theoretical limit of the specific contact resistance. In practice, a good deal of empirical processing is usually required before a good ohmic contact is obtained.

b. Ion implantation

The approach of implanting the semiconductor surface is rarely applied to InP and its related materials because of the surface damage and loss of stoichiometry associated with bombarding the InP surface.

c. Epitaxial growth of a narrow band gap semiconductor

This method is realized by applying a semiconductor with an extremely narrow bandgap, such an InAs (Eg ~ 0.35eV), which can be epitaxially grown lattice matched to an InP substrate. It forms an ohmic contact with almost every metal that is deposited onto it, since this semiconductor has high electron and hole mobilities (33,000 and 460 cm^2/Vs, respectively, at 300K), and has surface states pinned in the bandgap near the conduction band edge [39, 40].

A thin capping semiconductor layer with a small band gap has been applied to many devices to achieve low contact resistance. One example includes n-type InAs-based nonalloyed ohmic contacts to n-type GaAs The Schottky barrier height, in this case, for metal contacts on InAs is less than or equal to zero (Figure 2-17a) [41]. Using an InAs thin layer, specific contact resistances ranging from 10^{-6}-$1.7\text{x}10^{-8}\Omega\text{-cm}^2$ have been obtained for both refractory materials and Ni/AuGe on GaAs and on InGaAs semiconductors [42, 43]. The discontinuity in the conduction band of InAs/GaAs or

InAs/InGaAs heterojunctions acts as a barrier to the flow of current from the metal to the semiconductor (Figure 2-17b). This is improved by adding a graded epitaxial layer of In_x Ga_{1-x} As (the In mole fraction graded from x=0 at the GaAs/In_xGa_{1-x} As interface to x=1 at the In_x Ga_{1-x} As/metal interface). It is believed that the heterojunction barrier is eliminated, forming a contact with a zero Schottky barrier height (Figure 2-17c). The use of a graded InGaAs cap layer has also led to low values of contact resistance. Values of 5.3×10^{-7} and $2.6\times10^{-7}\Omega\text{-cm}^2$ for nonalloyed and alloyed Ni/Ge/Au/Ti/Au contacts were obtained [44], respectively. Peng *et al* [45] demonstrated a refinement of InAs on GaAs in order to replace the thick InGaAs graded layer. A strained layer superlattice (SLS), metal/InAs/SL/GaAs, was used in this study. SLS layers offer several advantages. First of all, at the heterojunction, the effective barrier height can be reduced by SLS layers, since SLS layers can contribute carriers to the small band gap material at equilibrium. Secondly, SLS layers conduct current extremely well via carrier tunneling through the thin GaAs barriers. Thirdly, SLS layers can reduce the possibility of Fermi-level pinning at the interface, since SLS layers can prevent high defect state densities (dislocations) from generating or propagating from the surface of the InAs contact layer into the substrate. An excellent contact specific resistance of $1.5\times10^{-8}\Omega\text{-cm}^2$ on n-GaAs has been obtained.

Analogous to the InAs case on n-type semiconductors, GaSb, in which the Fermi level is known to be pinned close to the valence-band edge, can be used for contacts on p-type GaAs. A $GaAs_xSb_{1-x}$ intermediate layer has been used, in which the layer was graded from GaAs at the channel to GaSb at the interface with the metal [46]. A GaSb/GaAs SLS and a GaSb cap layer on a p-type contact structure have also been studied [47]. The contact resistance in both cases is between $\sim10^{-6}$ and $10^{-7}\Omega\text{-cm}^2$.

Capping layers of SiO_2, $W_{60}N_{40}$, TiN, ZrB_2, TiB_2, Ti and Pt, as protective films on contacts, have been studied [48-55]. They can potentially suppress outdiffusion and vaporization of III-V semiconductor materials. Therefore surface morphology, edge definition, and specific contact resistance are improved and thermal stability of contacts is enhanced.

2-3-4 Techniques of improving contact quality

a. Semiconductor surface treatment

Semiconductor surface treatment before metal deposition is important in contact formation. Contact quality can be improved by providing a clean semiconductor surface. Several methods of surface preparation are currently used, such as chemical cleaning, sputtering and plasma techniques.

Residual oxides or other contaminants exist on the surface of a semiconductor substrate. After deposition, the oxide or contamination will possibly affect, although how it does has not been well studied, the metal/semiconductor interaction if not eliminated. Commonly used chemical solutions for semiconductor surface cleaning are $HCl:H_2O$ (1:1) or NH_4OH: H_2O (1:10) [43].

Sputtering is also used to preclean the semiconductor surface before deposition. The contamination caused by exposure to atmosphere is eliminated after sputtering. Radio-frequency (rf) [56, 57] sputtering has been applied to GaAs surfaces before the deposition of NiAuGe contacts, yielding uniform r_c values. The contacts were stable after annealing at 410°C for 57 hours. Ar sputtering [58] was reported for cleaning InP and InGaAs for nonalloyed Ti/Au contacts. There is also argument as to whether the surface treatment plays a role in reducing specific contact resistance. Barnard [59] conducted Ar^+ sputtering tests on the surface of InP with a sulfur doping level of (3-5) x 10^{18} cm^{-3} for several different contact systems, including Au/PtTi, Au/Ni/Ti and Au/Ru/Ti. The results were compared with the same systems without surface sputtering of InP. He concluded that the Ar^+ sputtering step was unnecessary in the fabrication of ohmic contacts to highly doped InP. The reason for this is that sputtered InP surfaces showed abnormally high concentrations of oxygen and carbon in the Ti layer, which is thought to be related to the decomposition of the photoresist during the sputtering of the InP surfaces. The carbon and /or oxygen reacts with the hot Ti during deposition and forms an oxidized and /or carbonized layer.

Plasma techniques have been used to treat the surface with O_2 and NH_4OH. Photoresist residues can be removed, therefore contact stability characteristics are improved [60].

b. Diffusion barriers

Diffusion barriers are used in the case where the metal has a finite solubility for the semiconductor, which can lead to contact degradation. Materials which can reduce the interactions between the metal and semiconductor without degrading the quality of the contact can be chosen as barrier materials. The function of a barrier is to produce good surface morphology and to improve the thermal stability. Ti, TiN, ZrB_2, Si_3N_4, W and W-N and Ni-P have been investigated [61-65]. Ti is considered to be a good diffusion barrier and is applied to GaAs-based ohmic contacts. This will be discussed in the next section. TiN is a good diffusion barrier layer for Pd:Mg and Ru metallizations to both n-type and p-type GaAs. Stable contacts were obtained after annealing at 400-450°C for 5 hours. ZrB_2 has been used as a barrier for the Au/ZrB_2/NiAuGe system, Si_3N_4 for Zn and W and W-N for p-GaAs contacts. The contacts were thermally stable at annealing temperatures up to 550°C for 5 hours. The Ni-P system not only serves as an ohmic contact but also as a III-V compound diffusion barrier to both n-type InP and p-type InGaAs.

2-3-5 Ohmic contacts to InP

In designing an ohmic contact to a high-speed InP-based device, operated under a high current density and elevated-temperature conditions, a few constraints and requirements have to be taken into account in order to provide a suitable contact technology to support both short-and long-term device operation [16].

(i) An ohmic contact with the lowest possible resistance should be obtained by optimizing the contact design.

(ii) The ohmic contact should be stable over a wide temperature range. Limited intermetallic reactions should occur, providing an abrupt metal-semiconductor interface throughout contact processing.

(iii) The ohmic contact should be stable throughout the device operating conditions.

(iv) Stresses in the metal films, the underlying dielectric patterning layer, and the underlying semiconductor should be minimized.

(v) The contact should be compatible with the metal system used for the interconnection technology.

(vi) The fabricating process should fit the overall device manufacturing scheme.

It is essential for the above-mentioned constraints to be met in the micron-size device technology currently applied for both electronic and photonic devices. For submicron and deep submicron technologies in the future, stable and low-resistance contacts will be even more crucial due to higher current densities and small contact geometry definition. Some metallurgical phenomena, which play a role in determining the electrical properties of the metal-InP contacts, will be introduced in the following sections.

References

1. M.L. Cohen and J.R. Chelikowsky, *Electronic Structure and Optical Properties of Semiconductors*. Springer-Verlag, Berlin (1988).
2. J.C. Phillips, *Bonds and Bands in Semiconductors*, New York: Academic Press, 1973.
3. C. Kittel, *Introduction to Solid State Physics*, P. 183. John Wiley and Sons, Inc., New York (1986).
4. B.G. Streetman, *Solid State Electronic Devices*, P.56. Prentice-Hall, Inc., Engelwood Cliffs, N.J. (1980).

5. D.A. Neamen, *Semiconductor Physics and Devices: Basic Principles*, Richard D. Irwin Inc., 1992.
6. M.G. Holland, *Semiconductors and Semimetals*, Vol. 2, ed. R.K. Willardson and A.C. Beer, New York: Academic Press, 1966, p.3.
7. V. Swaminathan, *Indium Phosphide and Related Materials: Processing, Technology, and Devices*, p.11, ed. A. Katz, Artech House, Inc., Boston, London,1992.
8. J.M. Golio and R.J. Trew, *IEEE. Trans. Electron. Devices*, Vol. ED-30, 1411 (1983)
9. H. Morkoc, J.T. Andrews and S.B. Hyder, *IEEE. Trans. Electron. Devices*, Vol. ED-26, 238, (1979)].
10. H. Temkin, R.A. Longan, R.K. Karlicek, Jr., K.E. Strege, J.P. Blaha, and P.M. Gabla, *Appl.Phys. Lett.*, Vol. 53, 1988, pp.1156-1158.
11. M. Fukada, O. Fujita, and S. Uehara, *J. Lightwave Technol. G.*, 1987, pp. 1808-1811.
12. D.L. Meier and D.R. Schroeder, *IEEE Trans. Electron. Dev.*, Vol. Ed-31, 1984, pp. 647-651.
13. T.C. Eschbich, R.D. Carroll, R.N. Sacks, and W.J. Tanski, *IEEE Trans. Electron. Devices*, Vol. 36, 1989, pp. 1213-1215.
14. J.A. Del Alamo and K. Mizutani, *Solid State Electron.*, Vol. 31, 1988, pp. 1635-9.
15. A. Yoshida, H. Tamura, T. Fujii, and S. H.sauo, *Extended Abstracts of 1987 International Superconductivity Electronic Conference*-ISEC, 1987, pp. 368-371.
16. A. Katz, *Indium Phosphide and Related Materials: Processing, Technology, and Devices*, p.307, ed. A. Katz, Artech House, Inc., Boston, London,1992.
17. D.G. Ivey and P. Jian, *Canadian Metallurgical Quarterly*, Vol.34, No. 2,pp. 85-113, 1995.
18. D.S. Yang, *Fundamentals of Semiconductor Devices*. McGraw-Hill, New York (1978).
19. C.W. Wilmsen, *Physics and Chemistry of III-V compound Semiconductor Interfaces*, Chapter 3, p73-163, ad. Carl W. Wilmsen, 1985 Plenum Press, New York.
20. J. Bardeen, Surface States and Rectification at a Metal-Semiconductor Contact, *Phys. Rev.* Vol. 71, 717-727 (1947).
21. R.H. Williams, V. Montgomery, and R.R. Varma, Chemical effects in Schottky barrier formation, *J. Phys.* Vol. C 11, L735-L738 (1978).
22. L.J. Brillaon, C.F. Brucker, A.D. Katnani, N.G. Stoffel, R. Daniels, and G. Margaritondo, Fermi Level Pinning and Chemical Structure of InP-Metal Interfaces, *Physics and Chemistry of Semiconductor Interfaces Conference*, Asilomar, Calif. (1982).
23. C.W. Wilmsen, *Physics and Chemistry of III-V Compound Semiconductor Interfaces*, Chapter 4, p129, ad. Carl W. Wilmsen, 1985 Plenum Press, New York.
24. R.H. Cox and H. Strack, Ohmic Contacts for GaAs Devices, *Solid-State Electron.* Vol. 10, 1213-1218 (1967)
25. L.E. Terry and R.W. Wilson, Metallization Systems for Si Integrated Circuits, *Proc. IEEE* Vol. 57, 1580-1586 (1969).
26. E. Kuphal, Low Resistnace Ohmic Contacts to n-and p-InP, *Solid-State Electron.* Vol. 24, 69-78 (1981).
27. Y.K. Fang, C.Y. Chang, and Y.K. Su, Contact Resistance in Metal-Semiconductor Systems, *Solid-State Electron,* Vol. 22, 933-938 (1979).
28. W. Shockley, Research and Investigation of Inverse Epitaxial UHF Power Transistor, *Final Technical Report*, No. Al-TDR-64-207, AFAL (AFSC), W-PAFB (1964).

29. P.L. Hower, W.W. Hooper, B.R. Cairns, R. D. Fairmen, and D.A. Tremere, The GaAs field-effect transistor, in: *Semiconductors and Semimetals* (R.K. Willardson and A.C. Beer, eds.), Chapter 3, Vol. 7, Part A, pp. 147-200, Academic Press, New york (1973).
30. H. Murrmann and D. Widman, Current Crowding on Metal Contacts to Planar Devices, *IEEE Trans. Electron. Devices,* Vol. ED-16, 1022-1024 (1969).
31. H.H. Berger, Models for Contacts to Planar Devices, *Solid-State Electron*, Vol. 15, 145-158 (1972).
32. G.K. Reeves and H.B. Harrison, Obtaining the Specific Contact Resistance from Transmission Line Model Measurements, *IEEE Electron Devices Lett.*, Vol. EDL-3, 111-113 (1982).
33. S.M. Sze, *Physics of Semiconductor Devices*, John Wiley & Son, 1981.
34. S.H. Rhodeerich and R.H. Williams, *Metal-Semiconductor Contacts*, Clarendon, 1988.
35. C.W. Wilmsen, *Physics and Chemistry of III-V Compound Semiconductor Interfaces*, Chapter 4, p133, ad. Carl W. Wilmsen, 1985 Plenum Press, New York.
36. A. Katz, C.R. Abernathy, and S.J. Pearton, *Appl. Phys. Letter*, Vol. 56, 1208 (1990).
37. G.E. Bulman, G.F. Gwilliam III, and F.A. Chambers, *J. Electrochem. Soc.*, Vol. 136, 2423 (1989).
38. A. Bose and H.T. Henderson, *J. Electrochem. Soc.*, 134, 2372 (1987).
39. K. Kojiyama, Y. Mizushima, and S. Sakata, *Appl. Phys. Lett.*, Vol. 23, 458-460 (1973),
40. T.E. Fischer, F.G. Allen, and G.W. Giobeli, *Phys. Rev.*, Vol. 163, 1967, p.703.
41. J.M. Woodall and J.L. Freeouf, *J. Vac. Sci. Technol.* Vol. 19, 794 (1981).
42. S.L. Wright, R.F. Marks, S.Tinari, T.N. Jackson, and H.Baratte, *Appl. Phys. Lett.*, Vol. 49, 1545 (1986).
43. C.K. Peng, J. Chen, and H. Morkol, *Appl. Phys. Lett.*, Vol. 53, 1738(1988).
44. I. Mehdi, U.K. Reddy, J. Oh, J.R. East, and G.I. Haddad, *J. Appl. Phys.* Vol. 65, 867 (1989)
45. C.K. Peng, G. Ji, N.S. Kumar, and H. Morkoc, *Appl. Phys. Lett.*, Vol. 53, 900 (1988).
46. M. A. Rao, E. J. Caine, S.I. Long, and H. Kroemer, *IEEE Electron Devices Lett.*, Vol. 8, 30 (1987).
47. J. Chyi, J. Chen, N.S. Kumar, C. Kiely, C.K. Peng, A. Rockeet, and H. Morkoc, *Appl. Phys. Lett.*, Vol. 55, 570 (1989).
48. A.A. Lakhani, *J. Appl. Phys.*, Vol. 59, 2082 (1986).
49. E.T.S. Pan, A. Venezia, E. Kolawa, J.M. Molarius, M.A. Nicolet, and L. Tanton, *Thin Solid Films,* Vol. 166, 63 (1988).
50. M.F. Zhum A.H. Hamdi, M.A. Nicolet, and J.L. Tandon, *Thin Solid Films* Vol. 119, 5 (1984).
51. J. Herniman, D.A. Allan, and P.J. O sullivan, *IEEE Proc.*, Vol. 135, 67 (1988).
52. J.R. Shappirio, R.T. Lareau, R.A. Lux, J. Finnegan, D.D. Smith, L.S. Heath, and M. Taysing-Lara, *J. Vac. Sci. Technol.*, Vol. A 5, 1503 (1987).
53. W.P. Hong, K.S. Seo, P.K. Bhattacharya, and H. Lee, *IEEE Electron devices Lett.*, Vol. 7, 320 (1986).
54. K.B. Alexander and W.M. Stobbs, *Master. Res. Soc. Symp. Proc.* Vol. 181, 363 (1990).
55. Y. Jin, *Solid-State Electron*. Vol. 34, 117 (1991).
56. A. Callegari, D. Lacey, and T.S. Pan, *Solid-State Electron*. Vol. 29, 523 (1986).
57. A. Callegari, E.T-S Pan and M. Murakami, *Appl. Phys. Lett.* Vol. 46, 1141 (1985).

58. H.G. Bach, N. Grote, and U. Niggebruegge, Publ. by Les Editions de Physique. Les Ulis, Fr, 461 (1986).
59. W.O. Barnard, G. Myburg, F.D. Auret, J. B. Malherbe and C.W. Louw, *Applied surface Science* Vol. 70/71, 515-519 (1993).
60. C.S. Wu, K.K. Yu, M. Hu, and H. Kanber, *J. Electron. Mater*. Vol. 19, 1265 (1990).
61. B.K. Liew, J.L. Tandon, and M.A. Nicolet, *Solid-State Electron*. Vol. 30, 571 (1987).
62. M.P.Grimshaw, A.E. Staton-Bevan, *Mater.Sci. Eng. B:Solid-State Mater. Advanced Technol*. **B5**, 21 (1989).
63. T.S. Kalkur, Y.C.Lu, and C.A. Araujo, *Solid-State Electron*. Vol. 32, 281 (1989).
64. F.C.T. So, E. Kolawa, J. Tandon, and Marc-A. Nicolet, *J. Electro-Chem. Soc*. Vol. 134, 1755 (1987).
65. A. Appelbaum, M. Robbins, and F. Schrey, *IEEE trans. Electron. Devices* Vol. 34, 1026 (1987).

Table2-1. Properties of III-V compounds compared with Si, Ge ($T=300^0K$) (to be continued) [3- 7].

Semiconductor	Lattice constant (nm)	Density (gm cm^{-3})	Melting point (K)	Debye temperature (K)	Thermal expansion coefficient^{*1}(K^{-1})	Thermal conductivity [W(cm $^oC)^{-1}$]	Resistivity ρ (Ω-cm)
Si	0.543	2.33	1415		2.6	145	$2.5x \times 10^{5\ *2}$
Ge	0.565	5.33	937				43
AlP	0.5467	2.40	2823	588	4.5	0.9	10^{-5}
AlAs	0.5660	3.70	2013	417	4.9	0.8	0.1
AlSb	0.6136	4.26	1338	292	4.0	0.57	5
GaP	0.5451	4.138	1740	456	4.5	0.77	1
GaAs	0.5653	5.3161	1513	344	6.86×10^{-6}	0.46	$4 \times 10^{8\ *2}$
GaSb	0.6096	5.6137	985	266	7.75	0.39	0.04
InP	0.5869	4.81	1335	321	4.75×10^{-6}	0.68	8×10^{-3}
InAs	0.6058	5.667	1215	249	4.52	0.273	0.03
InSb	0.6480	5.7747	800	203	5.37	0.166	0.06

Table 2-1. Properties of III-V compounds compared with Si, Ge (T=300°K) (continued)

Semiconductor	Band gap energy (eV)	Electron affinity, χ, (V)	Dielectric constant	N_c *3 (x 10^{19})	N_v *4 (x 10^{19})	Intrinsic carrier concentration (cm^{-3})	Mobility (cm/V-s)		Effective mass (m^*/m^0)			
									e		h	
							μ_n	μ_p	m_l^*	m_t^*	m_{lh}^*	m_{hh}^*
Si	1.12	4.01	11.7	2.8	1.04	1.5x 10^{10}	1350	480	.98	.19	.16	.49
Ge	0.66	4.13	16	1.04	0.6	2.4x 10^{13}	3900	1900	1.64	.082	.044	.28
AlP	2.43						80				.20	.70
AlAs	2.16						1800		1.5	.19	.15	.76
AlSb	1.6						200		1.64	.23	.14	.94
GaP	2.26						300		7.25	.313	.16	.54
GaAs	1.42	4.07	13.1	0.047	0.7	1.8x 10^{6}	8500	400	.067		.08	.49
GaSb	0.7						5000	1000	.044		.044	.34
InP	1.35						4000	100	.075		.12	.56
InAs	0.36						22600	200	.024		.025	.37
InSb	0.18						10^5	1700	.014		.016	.39

*1 near room temperature.
*2 intrinsic resistivity.
*3 the effective density of electron states in the conduction band.
*4 the effective density of electron states in the valence band.

Table 2-2. Work functions of some elements and electron affinity of some semiconductors [5]

Element	Work function, ϕ_m (V)	Semiconductor	Electron affinity, χ (V)
Ag	4.26	Ge	4.13
Al	4.28	Si	4.01
Au	5.1	GaAs	4.07
Cr	4.5	AlAs	3.5
Mo	4.6	InP	4.38
Ni	5.15		
Pd	5.12		
Pt	5.65		
Ti	4.33		
W	4.55		

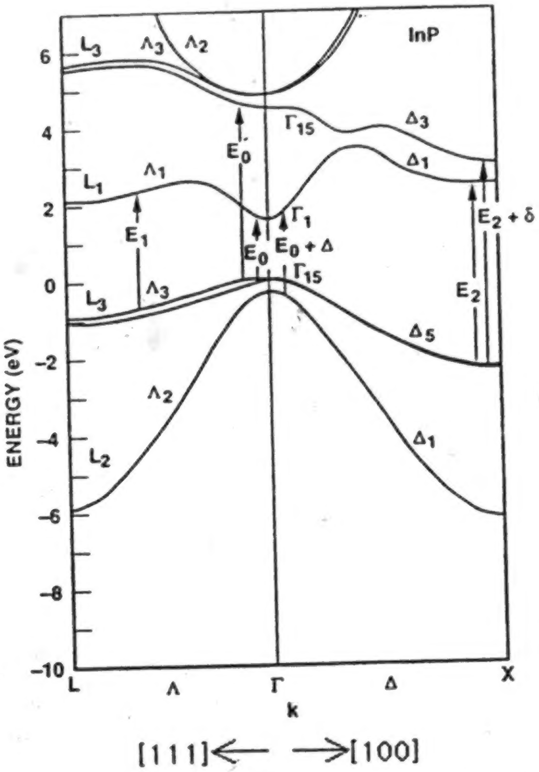

Fig. 2-1 Calculated energy band structure of InP in two principal directions in the Brillouin Zone. The various critical point energies are indicated [1].

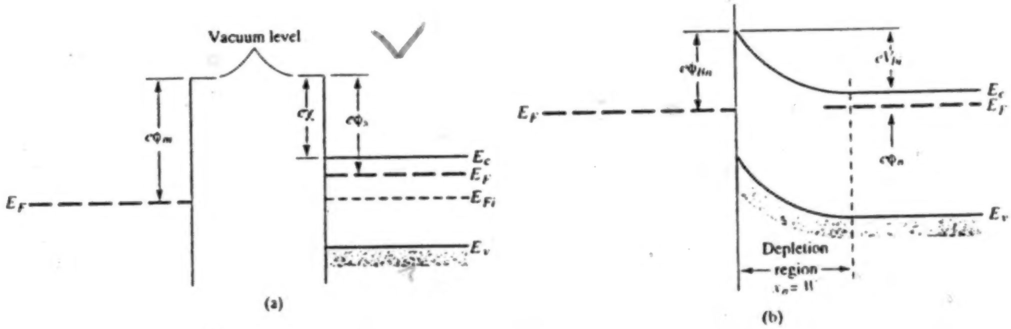
Vacuum level
eφm
eχ
eφs
Ec
EF
EFi
Ev
EF
(a)
eφBn
eVbi
Ec
EF
eφn
Ev
EF
Depletion region
xn = W
(b)

Fig. 2-2 (a) Energy-band diagram of a metal and semiconductor before contact. (b) Ideal energy-band diagram of a metal-n-semiconductor junction for $\phi_m > \phi_s$ [5].

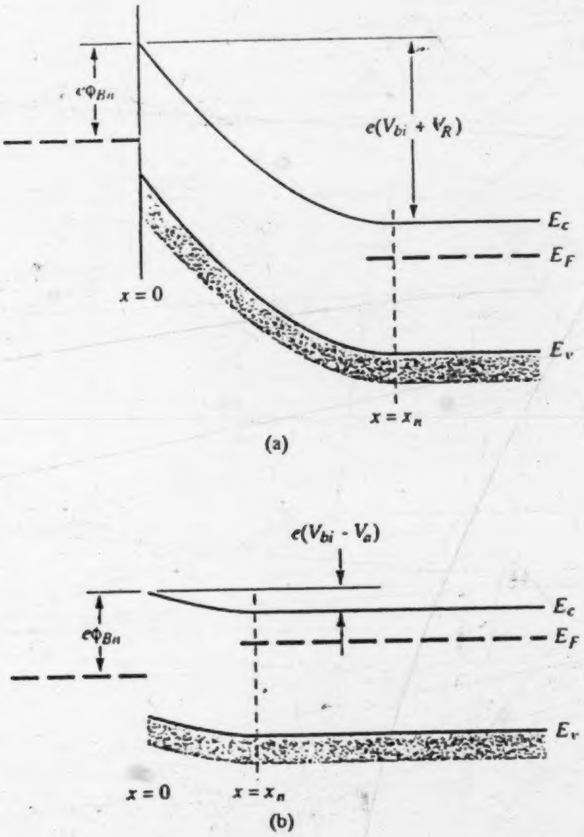
$e\Phi_{Bn}$
$e(V_{bi} + V_R)$
E_c
E_F
E_v
$x = 0$
$x = x_n$
(a)
$e(V_{bi} - V_a)$
$e\Phi_{Bn}$
E_c
E_F
E_v
$x = 0$
$x = x_n$
(b)

Fig. 2-3 Ideal energy-band diagram of a metal-semiconductor junction (a) under reverse bias and (b) under forward bias [5].

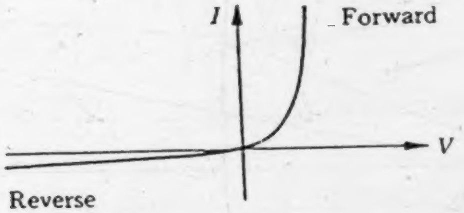

Fig. 2-4 Current-voltage characteristics of a Schottky contact.

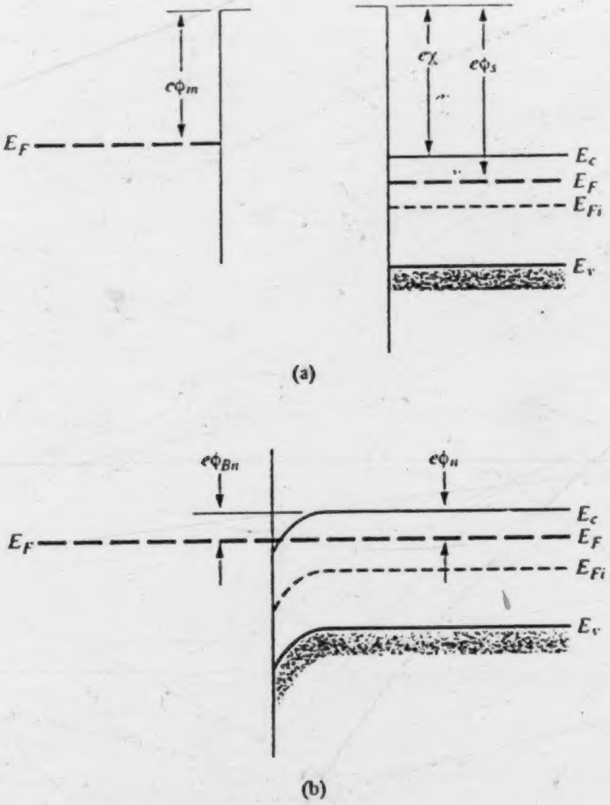
$e\phi_m$
E_F
$e\chi$
$e\phi_s$
E_c
E_F
E_{Fi}
E_v
(a)
$e\phi_{Bn}$
$e\phi_n$
E_F
E_c
E_F
E_{Fi}
E_v
(b)

Fig. 2-5 Ideal energy-band diagram (a) before contact and (b) after contact for a metal-n-semiconductor junction for $\phi_m < \phi_s$ [5].

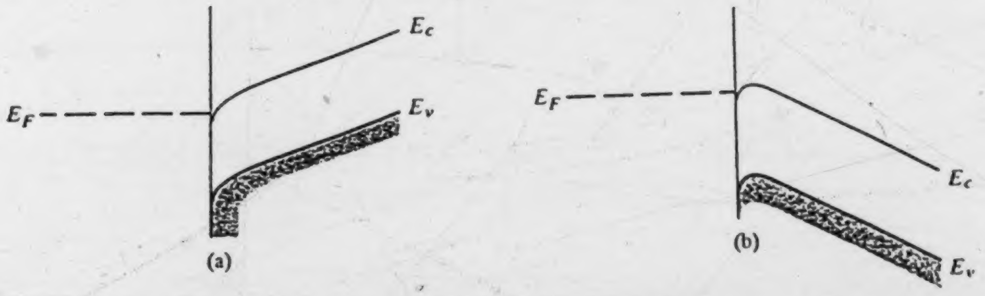
E_c
E_F
E_v
(a)
E_F
E_c
(b)
E_v

Fig. 2-6 Ideal energy-band diagram of a metal-n-semiconductor ohmic contact (a) with a positive voltage applied to the metal and (b) with a positive voltage applied to the semiconductor [5].

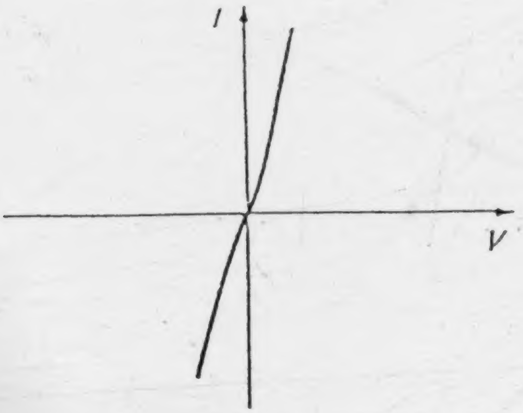

Fig. 2-7 Current-voltage characteristics of an ohmic contact [18].

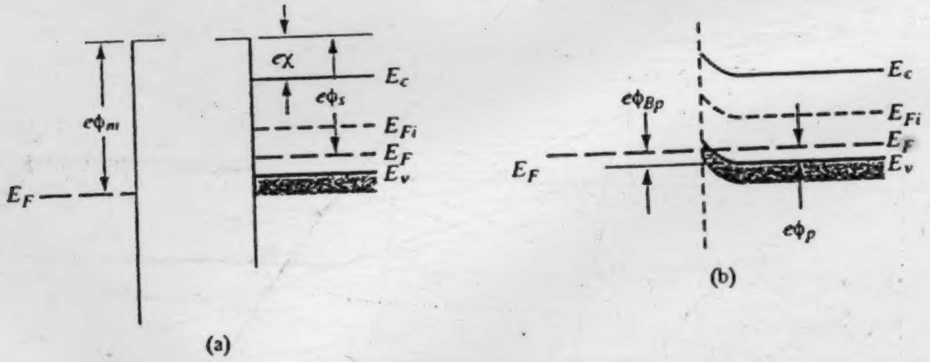
eχ
eφ_s
E_c
E_Fi
E_F
E_v
eφ_m
E_F
(a)
eφ_Bp
E_c
E_Fi
E_F
E_v
E_F
eφ_p
(b)

Fig. 2-8 Ideal energy-band diagram (a) before contact and (b) after contact for a metal-p-semiconductor junction for $\phi_m > \phi_s$ [5].

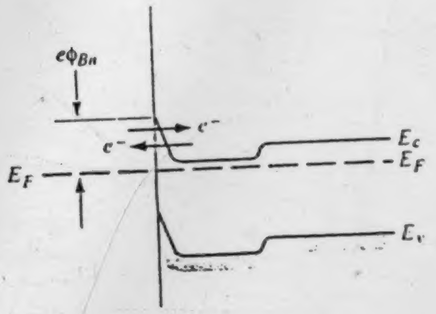
eφ_Bn
e⁻
e⁻
E_c
E_F
E_F
E_v

Fig. 2-9 Energy-band diagram of a heavily doped n-semiconductor to a metal junction [5].

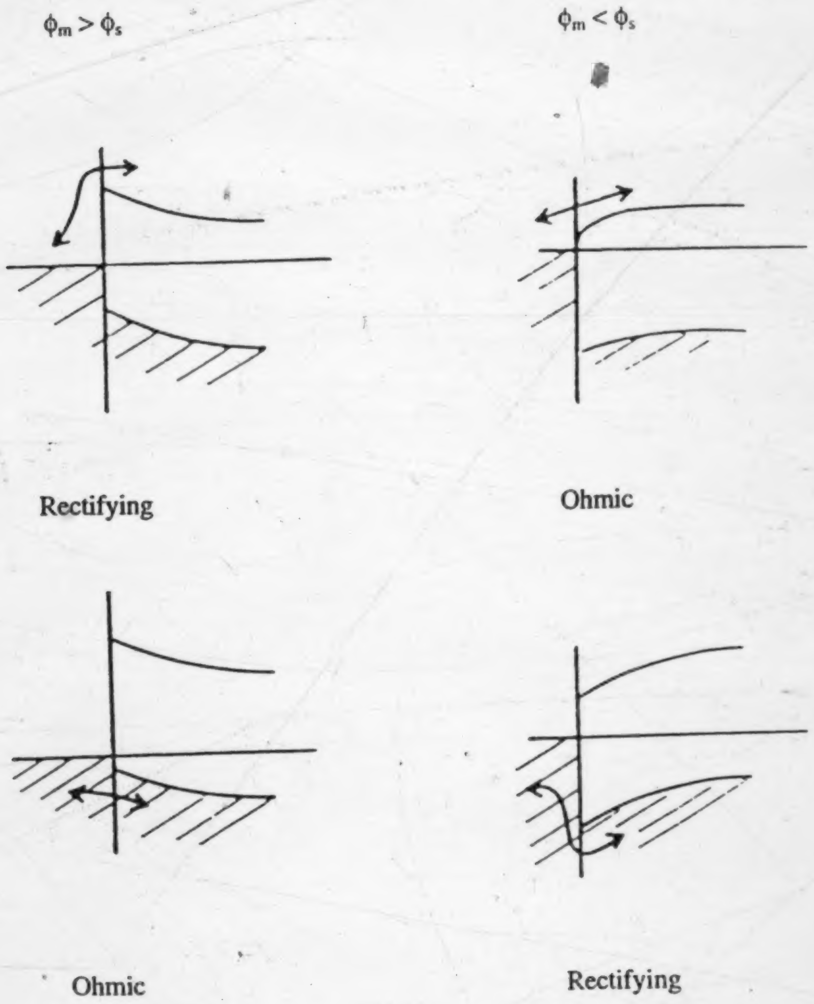
$\phi_m > \phi_s$
$\phi_m < \phi_s$
Rectifying
Ohmic
Ohmic
Rectifying

Fig.2-10 Band diagrams describing the Schottky theory of the metal-semiconductor interface. Four types of conduction are possible depending on the difference $\phi_m - \phi_s$ and the semiconductor type. The arrows indicate majority-carrier current flow [19].

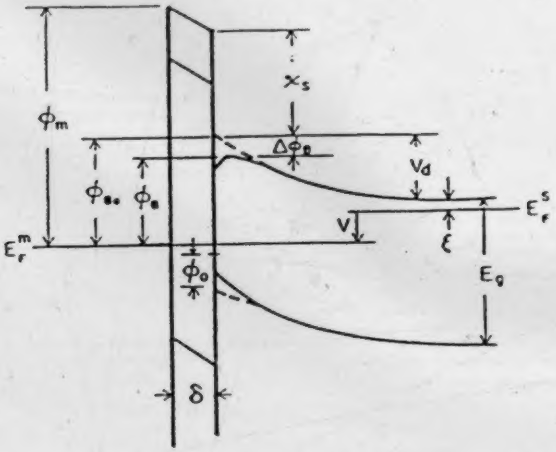

ϕ_m
χ_s
$\Delta\phi_o$
V_d
ϕ_{Bo}
ϕ_B
E_F^s
V
ξ
E_F^m
ϕ_o
E_g
δ

Fig. 2-11 Band diagram for a nonideal metal-semiconductor interface under forward bias V. An insulating layer of thickness δ exists between the metal and semiconductor and surface states are filled to level ϕ_o [19].

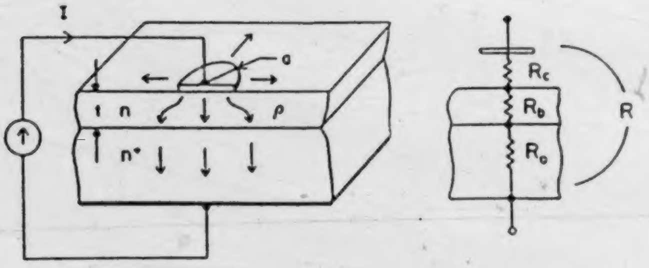

I
a
n
ρ
n⁺
R_c
R_b
R_o
R

$$r_c = \pi a^2 \left[R - \frac{\rho}{a} F\left(\frac{a}{t}\right) - R_o \right]$$

Fig.2-12 Measurement of the specific contact resistance r_c using the Cox-Strack method. The circular ohmic contact has radius *a* [23].

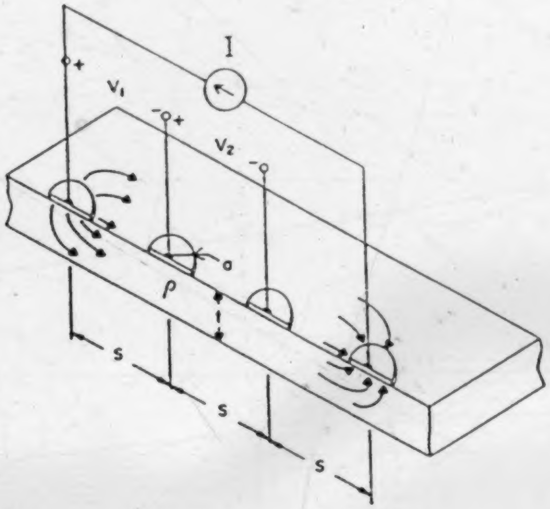

Fig. 2-13 Measurement of the specific contact resistance r_c by the four-point method [23].

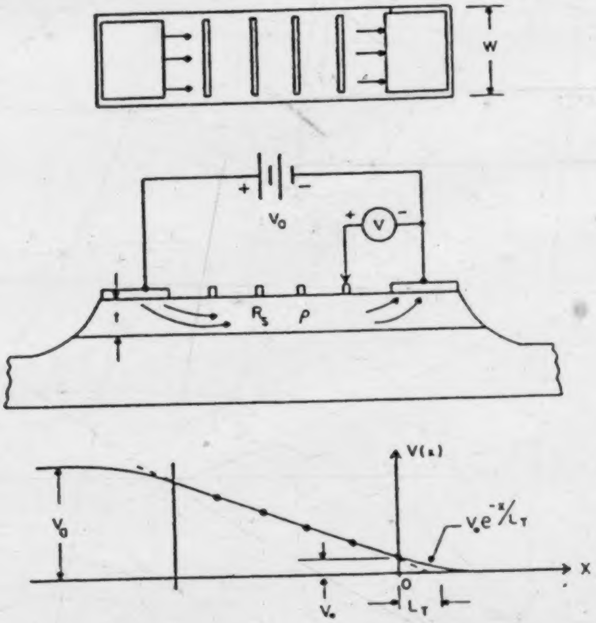

Fig.2-14 Measurement of the specific contact resistance r_c by the Shockley technique. The voltage applied to the coplanar ohmic contacts is V_a. The linear voltage distribution between the contacts is extrapolated to obtain the transfer length L_T [23].

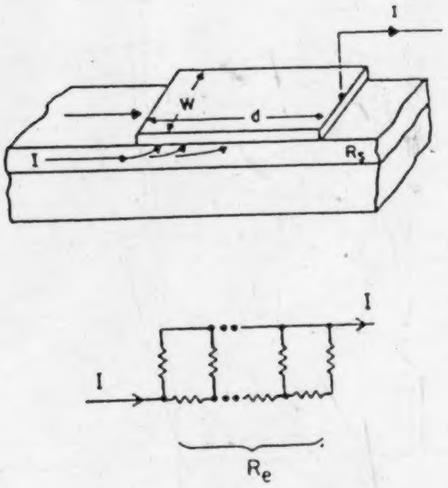

Fig.2-15 Measurement of the specific contact resistance r_c by the transmission-line model (TLM) technique. R_e is the total resistance of the metal-semiconductor interface and the epitaxial layer under the contact [23].

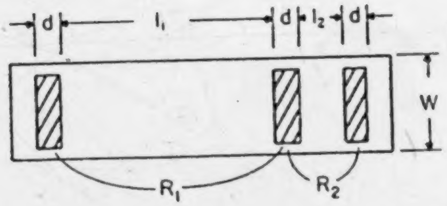

Fig.2-16 A simple method of determining R_e using a linear array of unequally spaced ohmic contacts. The shaded regions are the contact areas [23].

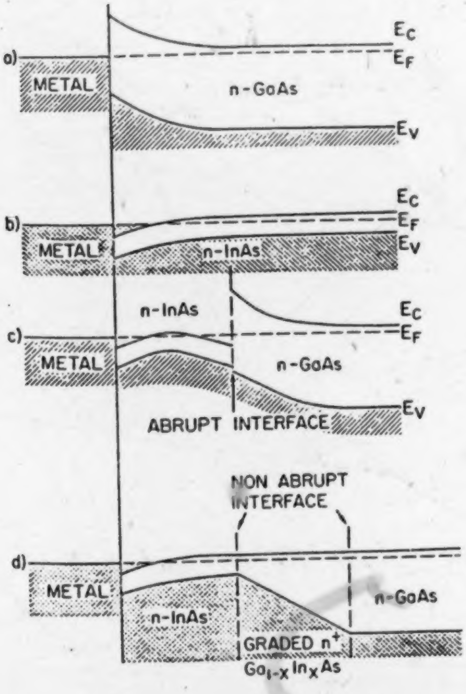
a)
METAL
n-GaAs
E_C
E_F
E_V
b)
METAL
n-InAs
E_C
E_F
E_V
c)
METAL
n-InAs
n-GaAs
E_C
E_F
E_V
ABRUPT INTERFACE
d)
NON ABRUPT INTERFACE
METAL
n-InAs
n-GaAs
GRADED n+
Ga1-x InxAs

Fig.2-17 Band bending for various semiconductor interfaces: (a) metal on n-InAs; (b) metal on n-InAs/GaAs and (c) metal on n-InAs on graded n^+-$Ga_xIn_{1-x}As$/GaAs.

Chapter 3

Experimental Methods

3-1 Film deposition

Deposition of metal thin films was done at NORTEL Technology. Metal layers were deposited on the InP substrates by means of electron beam evaporation. Prior to deposition, the substrates were polished with a 5% Br in CH_3OH solution, rinsed in methanol, degreased with a solution of equal parts HCL and H_2O, rinsed again and then etched and cleaned in a 1% Br in CH_3OH solution. The metals, i.e., titanium, nickel and germanium, were rinsed in methanol. Metal layers were then deposited on the InP substrates by means of electron beam evaporation using a 10 kV beam at 100-500 mA. The deposition sequences and layer thicknesses for the Ti and Ge/Ni metallizations are:

(1) 100 nm Ti on InP for the Ti/InP system;
(2) 50 nm Ni on InP for the Ni/InP system;
(3) 25 nm Ni on InP followed by 52.5 nm Ge on Ni for the Ge/Ni/InP system.

The thicknesses of the metallizations in Ge/Ni/InP system were chosen so that the atomic ratio of Ge / Ni slightly exceeds 1. Different ratios will result in different reaction products which will affect contact morphology. When the atomic ratio of Ge/Ni is less than 1, the products are expected to be Ge-Ni compounds and excess Ni, which may react with InP. If, however, the atomic ratio is greater than 1, NiGe is expected to form, leaving excess Ge. The excess Ge is expected to act as a dopant to make InP heavily doped, and therefore improve contact resistance.

3-2 Annealing

Wafers were sectioned into 5mm x 10mm pieces and then annealed at temperatures ranging from 250°C to 550°C for the Ti/InP system and 160°C to 450°C for the Ge-Ni /

InP system for various times. Annealing was carried out in a furnace with a flowing forming gas (95% N_2 +5% H_2) or nitrogen for the Ti/InP and GeNi/InP systems. Samples for Ni/InP system were first sealed in quartz under a vacuum of at least 10^{-4} torr and then annealed at temperature ranging from 190°C to 500°C.

3-3 X-ray diffraction (XRD) analysis

XRD analysis was done on all samples prior to specimen preparation for transmission electron microscopy (TEM) analysis. XRD spectra were obtained using a Rigaku Ru-200A-E1326 XRD System, equipped with a monochromator for x-ray diffraction and a rotating anode, operating at 30kV and 110mA. Spectra were then indexed with the aid of a computer software package named "Jade". Diffraction patterns were utilized primarily to identify phase changes and transformations.

3-4 Transmission electron microscopy (TEM)

TEM was utilized as the main characterization tool. Its high resolution capabalities, in terms of imaging, crystallography and compositional analysis, are well suited to the submicron features examined here. TEMs equipped with x-ray detectors allow interfacial reaction products to be qualitatively or semi-quantitatively identified by energy dispersive x-ray (EDX) analysis. The microscopes employed include a JEOL 2010 TEM equipped with a Noran, ultra thin window, Ge x-ray detector, a Hitachi H-7000 TEM and a Philips EM-410 TEM.

3-5 TEM specimen preparation

Both plan view specimens and cross section TEM specimens were examined in order to obtain a three dimensional representation of the microstructure. Unlike the specimens used for many other analysis methods, cross-section specimens for TEM can be quite difficult to prepare. However, cross-section specimens are particularly useful for TEM, since imaging parallel to the metal/semiconductor interface is possible. The morphology of interfacial reaction products can be revealed in detail. Plan view specimens permit imaging normal to the surface of the metallization, providing a larger field of view.

Excellent diffraction patterns can be obtained from a well prepared plan view specimen, making phase identification possible. A distinct layer as thin as 10 nm is attainable using chemical etching techniques combined with ion milling. Detailed procedures of specimen preparation have been reported in a number of articles, e.g., [1,2]. Specimen preparation procedures are briefly described below.

3-5-1 Cross section specimen preparation

The procedure for preparing a cross section specimen is shown schematically in Figure 3-1, and described below:

(i) Two sample pieces, approximately 5 mm long and 1 mm wide, are cleaved from the metallized wafer along with pieces of the same size from a scrap InP wafer (Figure 3-1a).

(ii) The two sample pieces are glued together face-to-face with pieces of scrap InP wafer glued to both sides to form a "sandwich" or "raft" (Figure 3-1b). The number of scrap InP pieces on both sides should be the same and should form a raft-like structure more than 3 mm wide. The epoxy is cured at ~100°C.

(iii) A disc 3 mm in diameter is cut from the raft and then polished to a thickness of ~200 μm (Figure 3-1c).

(iv) Both surfaces are dimpled and polished to produce a small hole in the centre. 1μm diamond paste is used for the final polish to produce a mirror finish on the surface. The final diameter of the hole should be less than 0.5 mm (Figure 3-1d).

(v) The specimen is ion milled for about ~40 min at 4 kV and an incident angle of ~12-13° to the surface, followed by ~20 min at 2-3kV.

InP tends to sputter much more rapidly than the metal layers. InP itself is also subject to preferential sputtering, i.e., P tends to sputter faster than the In, leaving globs or islands of In on the surface [3]. Specimen cooling with liquid nitrogen was used during ion milling in order to minimize preferential sputtering effects to produce electron transparent regions for TEM examination.

3-5-2 Plan view specimen preparation

The procedure for preparing a plan view specimen is shown in Figure 3-2, and is described as follows:

(i) A 3-mm disc is cut from the metallized wafer and ground to approximately ~150μm (Figure 3-2a).

(ii) The sample is dimpled from the semiconductor side down to a thickness about 30-50μm (Figure 3-2b).

(iii) Thinning to perforation is achieved by single-sided chemical jet polishing from the InP side using a solution of 1% of Br in ethanol.

For multilayer metallizations, or a monolayer metallization after annealing, several layers may form. Isolation of specific layers was used for phase identification purposes. This is realized by a combination of chemical polishing and sputtering from either the semiconductor or the metallization side for a brief period of time at low energy. Usually, several samples are necessary to identify each phase (or layer).

3-6 EDX analysis

EDX analysis was realized from the area of interest on a cross section specimen using the JEOL 2010 TEM. Quantification can be achieved using the following equation [4].

$$C_A / C_B = K_{AB} (I_A / I_B) \qquad (3\text{-}1)$$

or

$$X_A / X_B = K_{AB} (I_A W_B / I_B W_A) \qquad (3\text{-}2)$$

where, C_A and C_B are the concentrations of elements A and B in weight percent respectively. I_A and I_B are the intensities of the EDX spectra from elements A and B respectively. X_A and X_B are the concentrations of elements A and B in atomic percent and W_B and W_A are atomic weights of elements A and B respectively. K_{AB} is the Cliff-Lorimer proportionality factor, which is independent of the specimen composition and thickness (below a critical value).

3-7 Electron diffraction

Electron diffraction is a powerful technique used in TEM analysis for phase identification. Unlike other methods, it can utilized to solve the crystal structures of a new or an unknown phase. Two techniques were employed here, i.e., selected area diffraction (SAD) and convergent beam electron diffraction (CBED).

3-7-1 Selective area diffraction (SAD)

SAD is used in identifying polycrystalline materials, epitaxially grown phases and even single crystal grains from an area of interest. SAD results in a pattern consisting of a series of rings corresponding to a polycrystalline phase or phases, or a simple array of bright spots corresponding to a single crystal phase. A polycrystalline ring pattern is from a large number of crystal grains. Each ring is the result of the diffraction from grains with the same orientation in the beam direction but different orientation in the other two dimensions, which implies that polycrystals with preferred orientation can be identified from ring patterns. A simple equation, $L\lambda = Rd$, is used to index the diffraction patterns, where $L\lambda$ is the camera constant (L is the camera length and λ is the electron wavelength). R is the radius of the rings or the distance from the central spot to a given reflection in spot patterns and d is then the spacing of a specific crystal plane. $L\lambda$ is usually obtained from a standard crystal. InP was used as a built-in standard in this work. SAD patterns in this experiment were obtained using Hitachi H-7000 TEM and a computer software package (Diffract Version 1.5a) was utilized to solve or simulate diffraction patterns in this study.

3-7-2 Convergent beam electron diffraction (CBED)

CBED patterns can provide three-dimensional structural information. Spatial resolution on the order of 5 nm or less is attainable. In order to achieve the very high spatial resolution of CBED, a small convergent probe must be used, and such probes are obtainable with probe-forming analytical electron microscopes (AEM) (JEOL 2010 in this case). In CBED, a convergent beam is focused on the specimen, and diffraction discs are formed in the back focal plane. The diffraction discs can contain an intensity distribution that, when properly interpreted, can provide three-dimensional crystallographic information. Additional higher-order Laue layers can sometimes be observed. However, these reflections are generally less intense due to weak electron scattering that occurs at high scattering angles.

A central incident beam parallel to certain zone axes or one or several reflections meeting the Bragg condition is often required in order to obtain different CBED patterns. Some commonly used CBED patterns include zone axis patterns, which present the two-dimensional symmetry and three dimensional symmetry of a specimen, two beam CBED patterns and symmetrical many-beam CBED patterns, which can be used to determine a center of symmetry or other symmetry elements [5-7]. These methods are particularly useful when the crystal structure is an unknown.

The conventional way to solve a CBED pattern is the same as that for a SAD pattern. In most cases, particularly for the solution of a unknown crystal structure, lattice parameters, crystal symmetries, the type of unit cell and space group need to be determined. This is a complex procedure [8, 9] and its success is dependent on many conditions.

3-8 Phase identification

Phase identification was carried out by means of electron diffraction combined with EDX analysis. EDX analysis provides information about the composition of the phase examined. Quantitative analysis is often difficult to realize, therefore phase identification cannot only rely on this type of analysis. Semi-quantitative analysis is used here, which permits identification of the elements present as well as the approximate composition. When used in combination with electron diffraction, conclusive phase identification is generally possible. In this study, a JEOL 2010 TEM was employed for EDX analysis. A beam size as small as 2 nm is attainable, however, beam intensity and subsequent x-ray generation is limited.

3-9 Contact resistance measurement

Measurements of contact resistances were carried out using a modified transmission line method. In the more commonly used transmission line model with rectangular contacts, the current flow at the edge of the contacts can significantly affect the contact resistance measurement results due to nonuniform current flowing. A mesa etch is required to eliminate the unwanted current flow pattern. By using a circular test pattern, all the current is confined and flows uniformly from the positive to the negative, because of the inherent self-isolation of the circular symmetry, which eliminates the need for the mesa and therefore simplifies the fabrication procedure [10]. Specific contact resistance r_C were measured with a circular transmission line resistor with varying gaps - the smallest being 2 μm. Details of the technique and resistance calculations are given in references [10,11].

References

1. D.G. Ivey and G.R. Piercy, *J. Elect. Microsc. Tech.*, Vol. 8, 233 (1988).
2. J.C. Bravman and R. Sinclair, J. *Elect. Microsc. Tech.*, Vol. 1, 53 (1984).
3. N.G. Chew and A.G. Cullis, *Appl. Phys. Lett.*, Vol. 44, 142 (1984).
4. J.I. Goldstein, D.B. Williams and G. Cliff, Quantitative X-Ray analysis, from "*Principles of Analytical Electron Microscopy*", D.C. Joy, A.D. Romig and J.I. Goldstein, eds., Plenum Press, New York, (1986).
5. A.E. Green and J.A. Eades, in *Proceeding of the 44th Annual EMSA Meeting*, Ed. G.W. Bailey, San Francisco Press, Sanfrancisco, p.624, (1986).
6. P. Goodman, *Acta Cryst.*, A Vol. 31, 804, (1975).
7. M. Tanada, R. Saito and H. Sekii, *Acta Cryst.*, A Vol. 39, 357-368, (1983).
8. A. Howie, *Philos. Mag.*, Vol. 14, 223, (1966).
9. M.V. Berry, *J. Phys.*, C Vol. 4, 697-722, (1971).
10. A. Scorzoni and M. Finetti, *Mater. Sci. Rep.*, Vol. 3, 79 (1988).
11. G.S. Marlow and M.B. Das, *Solid-State Electron.*, Vol. 25, 91 (1962).

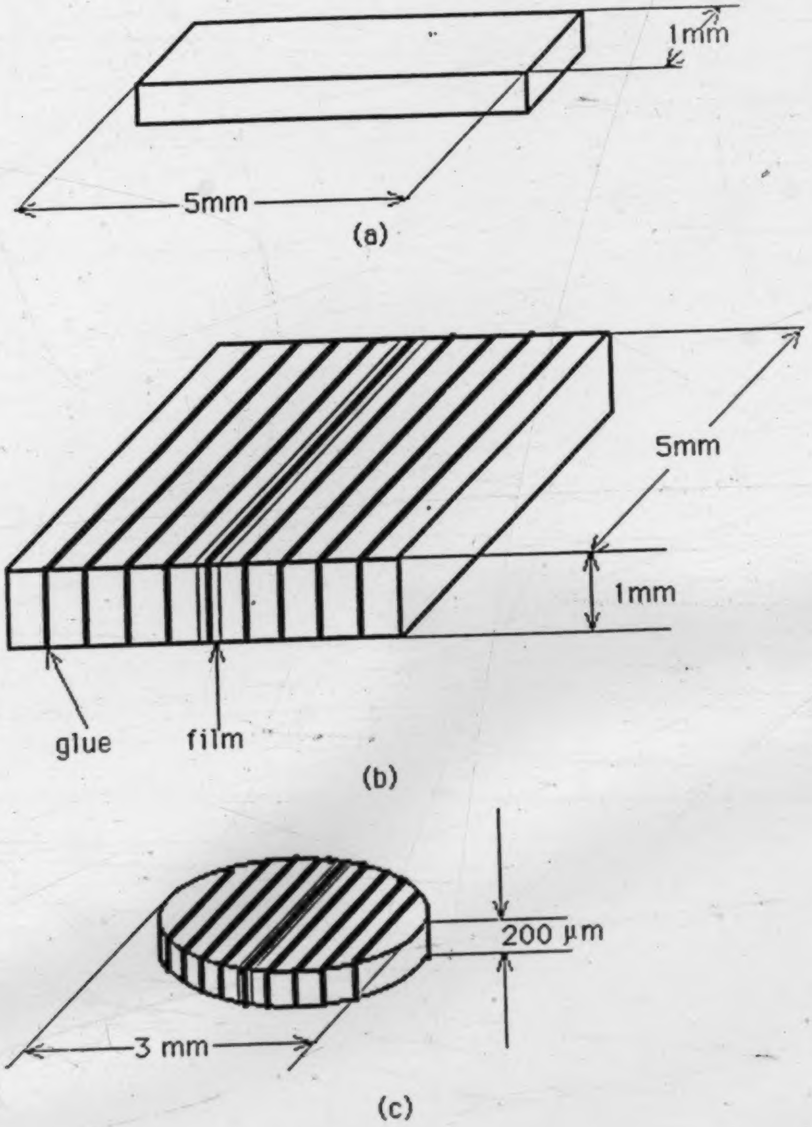
1mm
5mm
(a)
5mm
1mm
glue
film
(b)
200 μm
3 mm
(c)

Fig. 3-1 Schematic of procedure for cross section specimen preparation: (a) sample piece; (b) "raft-like" structure; (c) a disc.

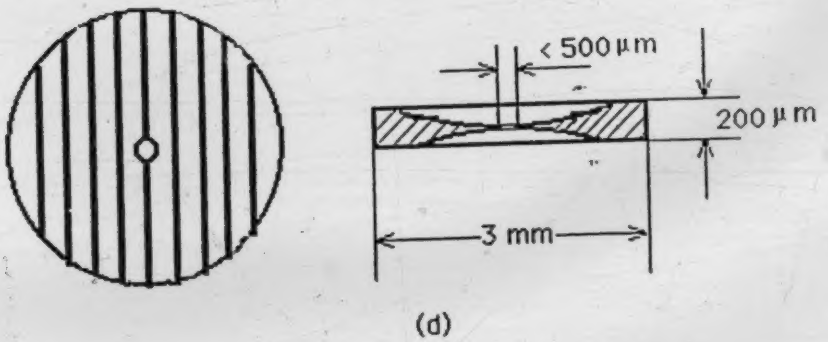
< 500 μm
200 μm
3 mm
(d)

Fig. 3-1 Schematic of procedure for cross section specimen preparation: (d) a disc after polishing.

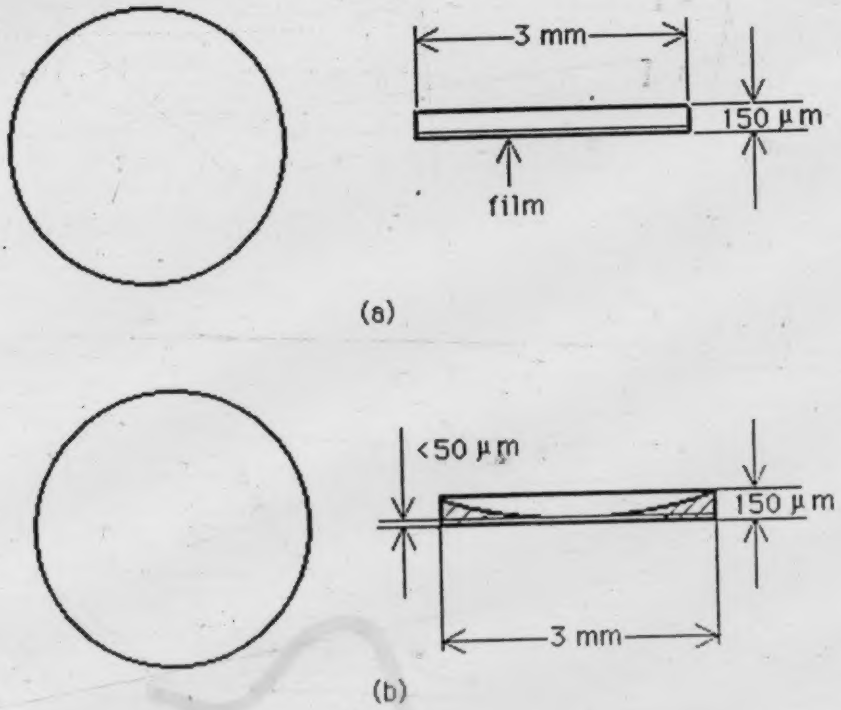
3 mm
150 μm
film
(a)
<50 μm
150 μm
3 mm
(b)

Fig. 3-2 Schematic presentation of procedure of plan view specimen preparation: (a) a specimen disc 3mm in diameter: (b) a disc dimpled from the semiconductor side.

Chapter 4

Interfacial Reactions Between Ti Metallizations and InP

4-1 Ti-based ohmic contacts

In this section, Ti-based metallizations to InP and related semiconductors will be reviewed. Since metallizations to GaAs and related materials have been studied more thoroughly than InP, and some metallizations to InP are based on successful metallizations to GaAs, metallizations to GaAs will also be briefly described for the purpose of comparison.

4-1-1 Ti metallizations

Chemical properties of transition metals have been one of the most actively studied fields . Since Ti is an element near the beginning of the transition metal series, it has attracted attention from researchers.

In microelectronic devices, Ti is commonly used as a gate metal in the fabrication of GaAs field-effect transistors [1]. Titanium has also been employed in contact fabrication, since it improves adhesion to the semiconductor.

Titanium, both by itself and its nitride, is considered to be a good diffusion barrier. The main advantage of using Ti or other refractories (such as W or Mo) is to obtain contact thermal stability both during processing and in real applications. Refractory metal contacts are expected to withstand high temperatures encountered during device processing. In addition, they can act as barriers preventing or at least minimizing outdiffusion of substrate material such as Ga and As in the case of GaAs, or In and P in the case of InP.

4-1-2 Ti-semiconductor Interactions

a. Ti metallizations to GaAs

The first study of the Ti/GaAs (110) interface was made by Ludeke and Landgren [1] using high-resolution photoelectron core-level spectroscopy to follow chemical and electronic changes. Photoemission experiments showed that strong chemical reactions occur at clean Ti/GaAs (110) interfaces formed at room temperature in ultrahigh vacuum. Interactions between Ti and GaAs occur for coverages beginning far below a monolyaer (ML) (1 ML is equivalent to a GaAs (110) surface atom density of $8.86 \times 10^{17} cm^{-2}$). Gallium, as a reaction by-product, is not distributed as a individual layer at the interface, but appears to be diffused over several GaAs lattice planes beneath the interface. The corresponding distribution of Ti or As is not known. No evidence for Ti clustering in the monolayer range was found although some interfacial reaction between Ti and GaAs was observed. Considerable out-diffusion of Ga and As into the growing Ti film was observed throughout the coverage. Gallium was found dispersed in the metal film. Arsenic appeared to be segregated on the surface. A metal-As compound was believed to form, which is based on the observation of diffusion of Ga in Ti. The Schottky-barrier height for Ti to both n-type and p-type GaAs (Si or Zn doping level of $5\text{-}10 \times 10^{17} cm^{-3}$) was determined to be 0.73eV.

Wu and Yang reported their study on the structural characterization of Ti thin films on GaAs (100), with the aim of trying to explain the Schottky barrier behaviourof Ti/Pt/GaAs and Pt/Ti/GaAs bimetal Schottky diodes [2]. Characterization was based on AES depth profiling in conjunction with TEM, and indicated that substrate atom out diffusion was very limited at annealing temperatures upto 300°C for 5 min. It is difficult to tell the detailed interface morphology at very low coverage (<0.5 nm) due to the limited depth resolution of AES. Therefore, possible clustering of Ti during initial growth is claimed by the authors, although this possibility was ruled out by Ludeke and Landgren [1]. Titanium oxide formed at the Ti/GaAs interface due to Ti's high reactivity [3-5].

b. Ti metallization to InP

Studies on Ti metallizations to InP-based materials are still far behind those on GaAs-based systems. Attention has recently been paid to the interface structural analysis of Ti metallizations to InP. Ji *et al* [6] studieded that the Ti/InP (110) interface by x-ray photoelectron spectroscopy (XPS) and ultraviolet photoelectron spectroscopy (UPS). They found that breaks in In-P bonds, which result in decomposition of InP, were confirmed to be caused by deposition of Ti on the surface. Indium was found to diffuse into Ti films at room temperature. Ti and P, released from the decomposition of InP, interact at temperatures ≥ 350°C to form TiP compound.

The interfacial study carried out using photoelectron spectroscopy (PES) showed high sensitivity in identifying reactions, where the existence and the state (i.e., as a compound or single element) of an element can be determined by the difference in bonding energy for the element. However, this technique, like other methods, such as Auger electron spectroscopy (AES), has limited applicability in showing the interface microstructures and providing phase identification.

4-1-3 Ti-based metallizations

As mentioned before, one of the most common methods to produce ohmic contacts is to highly dope the surface region of the semiconductor and then deposit a single layer of appropriate metal. Single layer metallizations to semiconductors are not often ideal contacts, so that the metallization scheme is modified by adding other metals in order to achieve better contact behavior. In practice, contacts are multilayered structures. Reactions occur during annealing leading to the formation of several intermetallic compounds between the metals and semiconductor.

A number of metallization schemes have been proposed. Only recently have metallizations been systematically classified and reviewed [7,8]. Ti-based contacts generally refer to any metallization scheme which contains Ti. These can be a single component Ti system or a multilayer scheme such as Ti/Pt/Au. The common feature of these contacts lies in the role of Ti, i.e., to act as a diffusion barrier. Ti is one of the refractory metals, which include W, Ti and Mo, and is often used as in conjunction with other elements to form ohmic contacts to III-V semiconductors.

a. Ti-based contacts to GaAs

All refractory metal contacts, with the exception of Ti, to n-GaAs have very low specific contact resistances and are stable at ≈400°C. This temperature is compatible with the wiring and packaging process [9].

Titanium is also applied in ohmic contacts to p-type semiconductors, e.g., Au/Zn-based metallizations to p-type GaAs. The addition of Ti to Au/Zn-based metallizations results in a low contact resistance, in which Ti plays a role in restricting lateral and vertical diffusion of Zn [10]. Zn is used to dope the semiconductor.

It is reported that contact resistances as low as $10^{-6}\Omega\text{-cm}^2$ were achieved in Pt/Ti contacts to p-type GaAs (Zn-doped to $5\text{x}10^{18}\text{cm}^{-3}$) [11]. The reaction sequence is schematically illustrated in Fig 4-1 [9]. At 400°C, Ti reacts with GaAs to form TiAs at the interface. As the ambient temperature increases to 450°C, Ga out diffuses toward the contact surface forming PtGa at the Pt/Ti interface.

An investigation [12] of Au/Pd/Ti (400nm/75nm/75nm) ohmic contacts to a 0.3μm thick p^+GaAs layer (Zn-doped to $5\text{x}10^{18}\text{cm}^{-3}$) grown on GaAs was carried out using a combination of TEM, EDX, secondary ion mass spectroscopy (SIMS) and electrical measurements. There is only limited reaction between the metalization and semiconductor on heat treatment. Annealing at temperatures up to 380°C for 8 min did not change the layered structure. The layer sequence was retained as: Au-rich, Pd-rich and Ti-rich layers. Minimal depth penetration ($\leq$2 nm) into the p^+GaAs epilayer was determined by high resolution dark field imaging indicating that the Ti had exibited limited inward diffusion. An amorphous Ti oxide thin layer ($\approx$6 nm thick) was present at the GaAs interface. Phase identification was not conclusively achieved. The Au-rich layer (Au solid solution phase containing Ga) increased in thickness as the anealing time increased. The presence of Au in Pd layer indicated that Au migration into the Pd film occurred during annealing. Titanium showed remarkable stability, i.e., almost pure Ti was retained. Possible Zn dopant diffusion from the epilayer into the metal may have resulted in the high measured contact resistance value (2.72 Ω-mm ±0.40 Ω–μm for a sample annealed for 8 min at 380 °C).

b. Ti-based contacts to InP

The standard n-type contacts, used for the InP-based optoelectronic devices, are alloyed Au-Sn, Au-Ge-Ni, or Au-Ge metallization schemes [13-15]. Although these contacts have relatively low specific contact resistances, i.e., in the range of 2×10^{-6} to 2×10^{-7} Ω-cm^2, their low eutectic melting temperatures (280°C for Au-Sn and 361°C for Au-Ge) suggest that they have relatively poor thermal stability. Therefore, thick, uneven, and spiky interfacial reaction products occur in the contacts. Thermally stable microstructures and electrical properties, for both p-type and n-type ohmic contacts, are a basic requirement for high-speed optoelectronic devices operating under high current density and long duration at elevated temperatures. Specific attention has to be paid to the reliability and performance of the ohmic contact in the vicinity of the active region. The most appropriate metals to meet these requirements are the refractory metals, which are utilized to form high-quality nonalloyed contacts to both p^+-InGaAs(P) and n-InP [16-18] layers.

Katz and his co-workers have extensively studied Ti/Pt-based ohmic contacts, starting with Pt/Ti metallizations to S doped n-type InP (5×10^{17}, 1×10^{18} and 5×10^{18} cm^{-3} respectively) [19]. The contacts to the lower doped substrates (5×10^{17} cm^{-3} and 1×10^{18} cm^{-3}) were rectifying at annealing temperatures lower than 350°C. Higher processing temperatures resulted in conversion to ohmic behaviourwith minimum specific contact resistances of 1.5×10^{-5} and $5\times10^{-6}$$\Omega$cm^2, respectively.

Ti/Pt nonalloyed ohmic contacts were found to provide superior performance over conventional AuBe and AuGe metallization to InP. Thus, Ti/Pt metallizations may serve as a common contact for both p- and n-type InP-based optoelectronic devices. A $8\times10^{-7}$$\Omega$-cm^2 specific resistance was obtained at 450°C for 30 s (RTP annealing) for the contacts with a dopant level of 5×10^{18}cm^{-3}.

Interfacial reactions were characterized using AES and Rutherford back scattering spectroscopy (RBS). Limited Ti/InP interfacial reactions have been suggested. According to AES analysis, an almost abrupt interface was obtained. Heating at temperatures higher than 500°C resulted in a mutual migration and reaction of the Ti and the semiconductor elements. RBS spectra showed, in this case, that the Pt layer became permeated with lighter elements, and Ti had moved into the underlying InP layer. The structures annealed at 350°C and 450°C retained their layered configuation, but in comparison to the as deposited sturucture, some intermixing had occurred. According to an RBS utilities and manipulation package (RUMP) simulation, a thin layer (~100 nm) of In_xTi_y was proposed to form at the Ti/InP interface at 350°C and the layer thickened (to ~200 nm) at 450°C. Phosphous was not detected using RBS, due to its low mass.

The results obtained by different means seem to be contradictory. A wide range of studies in the field of ohmic contact characterization has been done by Katz's group using AES and RBS, with some limited TEM analysis [11,16,17,19,20]. However, phase identification was poorly demonstrated in each study because of the limitation of the research methods utilized. Each claim seems to be somewhat questionable. Very limited TEM work and AES analysis cannot sufficiently support the conclusions they make.

Another effort was made by Katz to study Pt/Ti contacts to p-type InP along with other systems (InAs, GaP and GaAs) [20]. A number of techniques, such as SEM, TEM, STEM, AES, RBS and SIMS, were employed in this study. Similar results were reported for the four systems, i.e., a Pt-Ti intermixed layer about 5 nm in thickness formed at a temperature of ~300°C and expanded as the annealing temperature increased. As with InAs and GaAs, decomposition of InP occurred at ≈350°C leading to outward diffusion of its components, which penetrated into the Ti layer. A ternary interfacial layer including Ti and both substrate elements formed at the Ti/InP interface and thickened at 450°C. Unlike Pt-Ti/GaAs and Pt-Ti/InAs systems, in which one of the substrate elements, such as As in InAs or Ga in GaAs, underwent outward diffusion through the Ti layer to accumulate at the Pt/Ti interface, In or P outward diffusion through the Ti layer did not occur in the InP system. Higher temperature annealing (500°C) led to a significant increase in the thickness of the ternary mixed layers between the substrate and the metal layers (see Figure 4-2). A number of phases, including Pt_3Ti, Ti_3In_4, Pt_3In_2 and In_2Pt, were suggested as possible reaction products at 450°C, but no conclusive identification was done. It should be pointed out that this phase identification was based only on a limited number of d spacings from a single SAD pattern. Another important point is that the Pt-Ti contact to InP, as well as GaP, remained rectifying regardless of the annealing conditions.

It is interesting to note that Ti is also used as a codopant with Fe in InP to suppress the interdiffusion of Fe and p-type dopants [21]. Full depletion of Fe from nominally Fe-doped semiconductor substrates or epitaxial layers has been observed. P-type dopants were found to rapidly diffuse into InP:Fe (InP is doped with Fe) causing an increase in conductivity by several orders of magnitude. Codoping of InP:Fe with Ti was selected to solve the problem of interdiffusion. Titanium gives rise to a deep donor level near the midgap in InP. Studies showed that the problem occurred in systems where InP:Zn epitaxial layers were deposited on InP:Fe. The Zn diffusion front extends far into the Fe-doped material. This concentration is of the order of the residual shallow donor concentration N_D in MOVPE grown InP. Thus, the net shallow impurity concentration can be easily converted to p-type ($N_A > N_D$). Since Fe is capable of acting as a compensator in n-type material, a decrease in resistivity by several orders of magnitude results. In addition, Zn can diffuse to the region underneath the interface to replace iron, resulting in a depletion region of iron in the nominally Fe-doped material. Fe extracted from this region is homogeneously distributed in the Zn-doped top layer. Different results are obtained if Fe+Ti-codoped epitaxial layers are used instead of InP:Fe. The high thermal stability of Ti in InP causes an abrupt doping profile at the interface of the two layers. Ti acts as a barrier against the interdiffusion of Fe and Zn. The out diffusion of Fe atoms into the top layer is reduced by at least a factor of five. In particular, no depletion of Fe from regions underneath the interface occurs.

A complete contact metallization scheme requires the deposition of a bonding pad on the top of the contacting metals. Gold caps are required on both the p and n contacts to enable wire bonding and solder bonding of the device to a suitable submount. The Au can be deposited during the ohmic contact deposition process or after contact annealing. Au/Pt/Ti contacts are currently used in p-type GaAs electron devices [22-24] and InGaAs inverted rib waveguide lasers.

Au bonding pads on top of Pt/Ti contacts to n-type InP ($1\text{x}10^{18}$ cm^{-3} S-doped) have been studied and similar results to Pt/Ti contacts have been obtained [25]. Limited reaction occurs at the Au-Pt and Pt-Ti interfaces, without any significant intermixing of the Ti and Au. This is due to the Pt's role as a diffusion barrier. As mentioned above, considerable outdiffusion of In was observed contacts to InP annealed at 450°C for 30 s. An annealing temperature in the range 400°C-450°C results in the lowest specific contact resistance, lowest induced biaxial stress in the metallization films and in the bonding pad structure and a stable contact microstructure. Pt serves as an efficient diffusion barrier during the heating cycle, preventing penetration of Au into the Ti layer and underlying InP, thereby preventing the degradation of the contact electrical properties and morphology. Only limited reaction occurred between the metallization elements, at least within the limit of RBS detection resolution. For the case of a thin Au cap layer, annealed at 450°C, some out diffusion of Pt to the contact surface and very limited interdiffusion at the Pt/Ti interface were observed. The specific contact resistance was measured to be $8\mathrm{x}10^{-6}\Omega\text{-cm}^2$, which is similar to the values for the Pt/Ti contact.

Several different Ti-based contacts to n-type InP systems, i.e., Au/Pt/Ti, Au/Ni/Ti and Au/Ru/Ti, have been studied [21] using AES for structural analysis and the Cox and four-point methods for specific contact resistance measurement. For the Au/Pt/Ti system, smooth surfaces were obtained for temperatures up to 400°C. Island formation, however appeared on the contact surface when annealed at higher temperatures. AES analysis on the island area revealed that all elements, except Pt, diffused to the outer surface of the contact. The reason for island formation was proposed to be due to localized decomposition of the InP surface [26], in which enhanced reaction occurred between Ti and P and between Au, P and In. Ti failed to act as an effective diffusion barrier. Ti, P and In, as well as O and C (present at the Ti/InP interface due to contamination), diffused towards the outer surface, which was not revealed in the studies made by Katz's group. The Pt diffused little in either direction. The Au diffused through the Pt layer to react with the P and In, likely forming Au-P and Au-In compounds [27]. The reactions at the Ti/InP interface are believed to result in a Ti-P intermetallic compounds, which is in good agreement with the result proposed by Katz's group [19]. A minimum r_c value of about $2\mathrm{x}10^{-5}\Omega\text{-cm}^2$ was obtained at 450°C.

Similar results to the Au/Pt/Ti system were obtained for the Au/Ni/Ti system. Poor surface morphology occurred after annealing at 400°C, although better than for the Pt/Ti contacts. Island formation appeared after annealing at ~450°C. AES analysis showed a dramatic difference in composition profiles between island areas and homogeneous areas. In the homogeneous areas, a Ni-P compound was claimed to have formed and acted as an additional diffusion barrier, preventing Au reaction with InP. However, the failure of Ti and Ni, or perhaps the Ni-P compound, to act as an effective diffusion barrier in the island areas is claimed to be related to localized decomposition of the InP surface. A minimum r_c value of $1\mathrm{x}10^{-5}\Omega\text{-cm}^2$ was obtained at 450°C , which is a little better than for the Au/Pt/Ti system.

Very smooth surface morphology for the Au/Ru/Ti contacts was obtained after 450°C annealing. This contact appeared to be more stable than the other two systems. According to the AES profile, Au and Ru depth distributions in the Ti layer did not change until 450°C. Gold diffused through the Ru to interact with InP as in the other two systems. Ti appeared to react with P and some Ti also diffused out towards the surface. Due to the chemical inertness and the limited solid solubility that Ru has for other elements [28,29]. the localized decomposition of the InP surface and the interactions with the metal overlayers did not affect the surface morphology. Ru is believed to be a very stable diffusion barrier in this case. Gold did diffuse through Ru and Ti to the InP surface, although Ti diffusion was decreased. A $1\times10^{-5}\Omega\text{-cm}^2$ specific resistance again was obtained after annealing at 450°C for this contact system. It should be pointed out that all compositions are based on AES depth profiles. Conclusive phase identification is not possible using AES. Therefore, the true relationship between contact microstructure and electrical properties cannot be revealed by means of AES analysis alone.

c. Ti-based contacts to other III-V semiconductors

Pt/Ti contacts to other p-type III-V binary and related ternary materials, such as InAs, GaP, GaAs [19, 30-32], $In_{0.53}Ga_{0.47}As$, $In_{0.52}Al_{0.48}As$ and $In_{0.7}Al_{0.3}As$ [14,32-34], show similar trends in the interdiffusion behaviourfor the as deposited and sintered conditions.

For GaAs and GaP systems, reaction between Ti and Ga started at ~400°C and continued at 450°C. Ti reacted with group V elements at the Ti/semiconductor interface at ~500°C and Ga out diffused to the Ti/Pt interface. Annealing at 550°C led to Ga and Ti outward diffusion leading to accumulation of these elements on the surface of the metallizations.

For the InAs system, as with in InP, Ti/semiconductor reactions started at 350°C and were enhanced at higher temperatures.

For the ternary systems, intermixing between Pt and Ti started at 300°C. The thickness of the intermixed layer increased as the annealing temperature was increased. Limited reactions were present at Ti/semiconductor interface for $Pt/Ti/In_{0.53}Ga_{0.47}As$ system. A quaternary intermixed layer containing Ti, In, Ga and As was found at the $Ti/In_{0.53}Ga_{0.47}As$ interface at 300°C. The thickness of this layer increased to 50 nm as the temperature was increased to 500°C, which implies that higher temperatures enhanced In, Ga and As outward diffusion through the Ti layer. Ti/semiconductor reaction for the $Pt/Ti/In_{0.52}Al_{0.48}As$ system took place at higher temperatures (at 450°C) than that for the $Pt/Ti/In_{0.7}Al_{0.3}As$ system (at 300°C).

Pt/Ti contacts to p-type InP, as well as to GaAs, GaP, $In_{0.52}Al_{0.48}As$ and $In_{0.7}Al_{0.3}As$ are Schottky barriers in the as deposited condition. Contacts to GaAs, $In_{0.52}Al_{0.48}As$ and $In_{0.7}Al_{0.3}As$ become ohmic at annealing temperatures ranging from 300-450°C, while Pt/Ti contacts to p-type InP and GaP retained their rectifying behaviouron annealing. Pt/Ti contacts to InAs and $In_{0.53}Ga_{0.47}As$ are ohmic in the as deposited condition. The best specific contact resistances are displayed after 450°C annealing.

It is obvious that contact electrical properties are linked to changes in contact microstructure caused by annealing at different temperatures. Titanium, as a diffusion barrier, plays an important role in obtaining an abrupt interfacial structure. However, the exact relationship between contact behaviourand microstructure has not been realized due to uncertain interfacial reaction characteristics or phase identification. Most interfacial reaction characterizations were based on AES and RBS analysis, which can only provide information on intermixing.

It is essential to understand the relationship between the microstructure and the electrical properties of the metal/semiconductor contacts in order to fabricate high-quality and reliable contacts. Almost all the modern analytical techniques have been utilized in the field of contact interfacial reaction characterization. Each has its advantages and at the same time its disadvantages. Transmission electron microscopy (TEM) combined with EDX analysis is one of the best techniques to analyze the microstructural changes which occur during annealing. Recently, TEM has been utilized to study Au/Pt/Ti contacts to p-type InGaAs [35]. In this study a 0.2μm thick layer of InGaAs, doped to a level of 7x $10^{18}cm^{-3}$ with Zn, was grown on Fe-doped <001> oriented InP. Annealing at 375-425°C resulted in the inward diffusion of Ti and outward diffusion of In and As, leading to the formation of TiAs, metallic In and Ga-rich InGaAs at the Ti/InGaAs interface. It was concluded that the Pt layer was concluded to act as a good barrier (below ~425°C), prohibiting In outward diffusion and eliminating Au inward difussion to the semiconductor interface. Electrical property measurements showed that as deposited contacts were Schottky barriers and became ohmic on annealing to 375-425°C. A minimum contact resistance of $2x10^{-5}\ \Omega cm^2$ was obtained. Phase identification was conclusively achieved (see Figure 4-3).

d. Other Ti-based contacts

Recently, self-aligned gate (SAG) technology [36-40] has been well developed to fabricate high-speed GaAs high electron mobility transistors (HEMT's) to produce source series resistance and improved FET performance. In this technology, the gate is used as an implantation mask during the formation of source and drain regions. In order to activate the implanted ions, high temperature annealing must be used. Therefore, the gate metals used in the SAG process require high thermal stability as well as good electrical characteristics. Many refractory metals have been investigated for SAG purposes. TiW nitride is one of those materials showing good thermal stability to GaAs after high temperature annealing. TiW-nitrides ($TiWN_x$) are also used as Schottky contact metals to n-type InP-based materials, e.g., TiWN$_x$ to Ga$_{0.51}$In$_{0.49}$P. Ga$_{0.51}$In$_{0.49}$P has superior properties in applications involving optoelectronic and high-speed devices. The study showed that the thermal stability of the TiWN$_x$ films increases with increasing nitrogen content. The electrical properties of TiWN$_x$ / Ga$_{0.51}$In$_{0.49}$P contacts depend on the nitrogen content in the TiWN$_x$ film and the phases formed after thermal annealing. TiWN$_x$ Schottky contacts demonstrate excellent electrical and physical characteristics, even after annealing at temperatures as high as 800°C. The barrier heights range from 0.81 to 1.05 eV depending on the the nitrogen content and the annealing conditions. No interactions were found at the TiWN$_x$ / Ga$_{0.51}$In$_{0.49}$P interface of both as depositedand annealed samples. It is believed that the excellent characteristics of the contacts were attributed to the high bandgap of Ga$_{0.51}$In$_{0.49}$P and the incorporation of nitrogen into the TiW films [41].

Above all, Ti is an important constituent in multicomponent metallization to InP and InP-based compound semiconductors. Titanium plays the primary role of providing improved metallization adhesion and thermal stability in various contacts. However, very little has been done to characterize in detail the reactions at Ti/semiconductor interface. In this study, identification of interfacial reactions occurring during annealing of Ti metallizations on InP substrates is carried out using TEM techniques combined with EDX analysis.

4-2 Reactions between Ti and InP

4-2-1 Experimental results and discussion

Ttitanium layers, ~120 nm thick, were deposited onto Fe-doped <001> oriented InP substrates. A bright field micrograph of a cross section specimen of an as deposited sample is given in Figure 4-4a, along with an EDX spectrum (Figure 4-4 b). The as deposited Ti layer consists of fairly uniform grains (≈25 nm in size), which can be seen from a bright field micrograph of a plan view specimen in Figure 4-5a. An SAD pattern from the as deposited plan view specimen (Figure 4-5a) is shown in Figure 4-5b. The Ti grains show a <001> preferred orientation perpendicular to the surface of the substrate.

Samples were examined after annealing at 250°C and 300°C for up to 10 min. No interfacial reactions were detected for these conditions. Initial reactions were identified in specimens annealed at 325°C for 5 minutes (see Figure 4-6). Two regions exhibiting different contrast were visible at the Ti/InP interface. The layers were too thin to identify conclusively at this point. EDX analysis indicates that the inner darker contrast region was In-rich while the adjacent lighter contrast region contained Ti and P. It is evident that decomposition of InP or reactions between Ti and InP occurred in this case. InP is known to decompose in vacuum on heating to 350°C [42]. The fact that InP decomposed at a lower temperature is likely due to the presence of Ti. This is in agreement with results obtained in the XPS study [6], in which deposition of Ti on the surface of InP (110) at room temperature has been reported to introduce breaks in the In-P bonds and subsequent diffusion of In atoms into the Ti film.

Longer time annealing at the same temperature resulted in further decomposition of InP. EDX analysis indicated that virtually pure In was present at the interface adjacent to InP. This layer was identified as In from samples annealed at higher temperatures. Ti and P were detected in the region between the Ti and In-rich layers. Identification of the structure of the Ti-P layer was not possible, as it was too thin. The Ti-P phase diagram (Figure 4-7) [43] shows that the solubility of P in Ti is very low, which implies that Ti-P region in Figure 4-6 is a Ti-P compound and not a solid solution phase.

Higher temperatures and longer annealing times resulted in significant decomposition of InP and reaction between Ti and P. Both In and a Ti-P compound were found as reaction products in the specimen annealed at 350°C for 2 hours. A bright field TEM image of a cross section specimen is shown in Figure 4-8. The compositions of each layer were determined by EDX analysis. The In layer was continuous and fairly uniform in thickness (≈50 nm). The outermost region of remaining titanium had oxidized. Bright field micrographs of individual layers were obtained. Indium, the inner layer, is shown in Figure 4-9. The grains of In were fairly uniform in size (~ 40 nm). Very thick grain boundaries are present in the In layer. This is possibly due to chemical thinning process. or ion milling. Large areas of grain boundaries might also be the reason for the faint SAD patterns taken from this region. A Ti-P compound layer was obtained from a plan view specimen shown in Figure 4-10a. The crystal grains of the Ti-P compound were very small (≈10nm). This implies that the crystal growth of the Ti-P compound was just at its initial stage. Through a combination of EDX analysis and SAD analysis, the identity of the Ti-P compound was narrowed down to Ti_4P_3 or TiP (see Figure 4-10b for the EDX spectrum and Figure 4-10c for the SAD pattern). A comparison between the d-spacings of these compounds and the d-spacings in Fig 4-10c are shown in Table 4-1. A better fit was obtained for TiP, where only one d-spacing at 0.259nm could not be indexed to TiP. Nevertheless, Ti_4P_3 should not be absolutely excluded. It is possible that both phases coexist at this point, while TiP appears to be the major phase. Assuming that TiP formation is preferred over Ti_4P_3, the following equation can be used to describe the reaction taking place in the interface between InP and Ti:

$$InP + Ti = In + TiP \qquad (4\text{-}1)$$

The amount of reaction products can be estimated From Equation (4-1). Assuming that the primitive volumes of the unit cells of In and TiP are 0.02615 nm^3 and 0.0301 nm^3, (or 0.1025 nm^3 for Ti_4P_3), mass balance calculations yield a thickness ratio of In to TiP of 1: 1.15 (or 1/1.31 for In:Ti_4P_3, assuming $3InP + 4Ti = 3In + Ti_4P_3$). In fact, the thickness ratio of In to TiP (or Ti_4P_3) is much higher than the ideal value (Figure 4-8). A greater amount of In relative to TiP indicates that reaction is not mass balanced and only a small amount of P reacted with Ti to form TiP compound. This is likely due to evaporation of most of the P produced from the decomposition of InP. It is easier for P, compared with In, to evaporate since P possesses a higher vapor pressure. Phosphorous was indeed detected by EDX analysis at the surface of the metallization. The interfacial reaction is more accurate if it is described by the following equation:

$$InP + mTi = In + mTiP + nP_{ev} \qquad (4\text{-}2)$$

$m + n = 1$, and $m/n \approx 0.21$ (according to the measurment of the thicknesses of the TiP and In layers), which implies that only ≈17at% of P produced by decomposition of InP reacted with Ti to form TiP.

The low rate formation of TiP must be attributable to kinetics. A reaction mechanism can be suggested, i.e., Ti induced decomposition of InP at low temperature, based on the study mentioned above [6]. In this case, InP decomposes at 325°C, which is lower than the 350°C reported previously [42]. This can be considered to be due to the existence of Ti. Titanium induced InP decomposition acts only at the initial stage. When Ti is in contact with InP, the decomposition of InP relies on Ti-induced breaks in the In-P bonds, which may result in the formation of TiP. Once a continuous In layer forms at the interface between TiP and InP, the Ti layer is separated from InP. Formation of TiP is realized through P diffusion through the In layer. The fact that a larger than ideal ratio of In to TiP was obtained indicates that the decomposition rate of InP is faster than that of the formation rate of TiP. Not all the P diffused to Ti is consumed to form TiP. Thermodynamic conditions may be feasible for both decomposition of InP and formation of TiP, however kinetics must favour decomposition of InP over the formation of TiP. Therefore, the reaction procedure is TiP formation controlled. Formation of TiP and P out diffusion (or evaporation) take place simultaneously. On the other hand, one can expect that increasing the temperature would change the relative rates of InP decomposition and TiP formation. This can be seen in the next section.

Ti-P compound formation between Ti and InP at the Ti/InP interface proceeded at more reasonable rates at higher annealing temperatures. A TEM micrograph from a cross section specimen annealed at 450°C for 1.5 hrs (Figure 4-11) shows an inner layer of In at the interface, a considerably thicker Ti-P compound adjacent to it and the remaining Ti film. A micrograph from the Ti-P compound and its SAD pattern are also shown in Figures 4-12a and b respectively. The crystal structure of the Ti-P compound is confirmed to be TiP rather than Ti_4P_3 in this case (Table 4-2). The grain size of TiP is approximately 30 nm. Comparison of Figure 4-8 (325°C anneal) with Figure 4-11 (450°C anneal) shows that the thickness ratio of In to TiP is close to theoretical value, which means that TiP formation is more kinetically favourable at higher temperatures.

It is obvious that P outward diffusion is a significant factor affecting the TiP growth rate. Since the InP decomposition rate at lower annealing temperatures is higher than the TiP formation rate, sufficient P is provided for Ti-P compound formation. If P out diffusion is inhibited by the presence of a barrier, TiP formation would be enhanced, which is shown for a Ti/Pt/Au metallization to InP in Figure 4-13 [35]. Platinum acts as a diffusion barrier limiting P outward diffusion, which results in a thicker TiP layer.

Specimens annealed at 550°C for 30 minutes show no significant change in the type of phases. EDX analysis indicates that the inner layer is In. TiP is adjacent to it. Indium appears to be non-uniform in thickness (thickness varies from 20-100 nm). Longer annealing times (>2 hrs) at this temperature results in a discontinuous In layer. In some area TiP grains extend through the In to contact with InP. The TiP phase, from a plan view specimen, is shown in Figure 4-14a along with its SAD pattern (Figure 4-14b). The grain size has increased (~40nm) compared with the 450°C anneal.

The fact that the In layer appeared to be thinner as annealing temperature and time were increased indicates that higher annealing temperature would favor, from the thermodynamic (or kinetic) point of view, the formation of TiP. Indium out diffusion would be more prominent due to its low melting point. Assuming that the diffusion rate of In through the TiP and Ti layers is equal to or faster than the consumption rate of P (P was consumed partially by the formation of TiP and partially by its diffusion through TiP and Ti layer), TiP will form in contact with InP. This can be seen in Figure 4-15, where a rough TiP/InP interface is shown to have developed after 4 hours at 550°C. Larger TiP grains are shown in Figure 4-15b, as is a TiP SAD pattern (Figure 4-15c). Indium outward diffusion (through Ti grain boundaries) resulted in its accumulation at the metallization surface in the form of an oxide, In_2O_3 (Figure 4-16).

A schematic illustration of the reactions between Ti and InP at temperatures ranging from as deposited temperature to 550°C is shown in Figure 4-17.

4-2-2 Ti-In-P phase diagram

Based on the results presented above, one can draw at least part of an isothermal section of the Ti-In-P phase diagram, for temperatures ranging from ≈350-550°C. This is shown in Figure 4-18, where the overall system composition is denoted by an X. Assuming a closed system, a three phase triangle, containing pt. X, can be drawn; the three phases are TiP, In and InP. The system is, in fact, not closed, as P out diffusion was detected. This results in a shift of pt. X to a more In-rich composition, but the three-phase region remains.

4-3 Conclusions

1) The deposited-Ti film possesses a <001> preferred orientation. The grain size is about 25 nm. No interfacial reactions take place in the specimens annealed at temperatures less than 325°C.
2) Initial reactions were observed after annealing at 325°C for 5 minutes, i.e., an In-rich region and a Ti-P region were present at the Ti/InP interface.
3) The reaction products between InP and Ti were found to be In (adjacent to InP), and mainly TiP (between Ti and In) in specimens annealed from 350-550°C.
4) Higher temperature or longer times annealing (500°C, >30 min) resulted in further decomposition of InP. The In layer became discontinuous as a result of significant out diffusion of In to the surface to form In_2O_3, leaving TiP in contact with InP in places.

References

1. R. Ludeke and G. Landgren, *Physical Review* B Vol. 33, No8.5526- 5535(1986).
2. X. Wu and E.S. Yang, *Journal of Electronic Materials*, Vol. 19, No. 8, 1990
3. R. Butz, G.W. Rubloff and P.S. Ho, *J. Vac. Sci. Technol.*, Vol. A1, 771 (1983).
4. M.A. Taubenblatt and C. R. Helms, *J. Appl. Phys.*, Vol. 53, 6308 (1982).
5. C.P. Lofbau and W.E.Swartz, *Thin Solid Films* Vol. 52, 271 (1978).
6. Ji Mingrong, Wu Jianxin, Ma Maosheng and Liu Xianming, *Vacuum* Vol. 43 No.11, 1157-1158 (1992).
7. T. Sands, *Materials Science and Engineering*, Vol. BI 289-312 (1989) .
8. D.G. Ivey and P. Jian, *Canadian Metallurgical Quarterly*, Vol. 34, No. 2, 85-113, (1995).
9. T.C. Shen, G.B. Gao and H. Morkoc, *J.Vac. Sci Technol.* B Vol. 10(5), Sep/Oct, 2113-2132 (1992).
10. M. Hirano and F.Yanagawa, *Jpn. J. Appl. Phys.* Vol. 25, 1268 (1986).
11. A. Katz, C.R. Abernathy, and S.J. Pearton, *Appl. Phys. Lett.*, Vol. 56, 1208 (1990).

12. B.M. Henry, A.E. Staton-Bevan, V.L. M. Sharma, M. A. Crouch, and S.S. Gill, *J. Electronic. Materials,* Vol 21, No.9, 929-933 (1992).
13. E. Kuphal, *Solid-State Electron*. Vol. 24, 69 (1981).
14. I. Camlibel, A.K. Chin, F. Ermanis, M.A. DiGiuseppe, J.A. Lourenco, and W.A. Bonner, *J. Electrochem. Soc*. Vol. 129, 2585 (1982).
15. G. Bahir, J.L. Merz, J.R. Abelson, and T.W. Sigmon, *J. Electronic Mater*. Vol. 16, 257 (1987).
16. A. Katz, W.C. Dautremont-Smith, P.M. Thomas, L.A. Koszi, J.W. Lee V.G. Rigs, R.L. Brown, J.L. Zilko and A. Lahav, *J. Appl. Phys*. Vol. 65, 4319 (1989).
17. A. Katz, W.C. Dautremont-Smith, S.N.G. Chu, P.M. Thomas, L.A. Koszi, J.W. Lee, V.G. Riggs, R.L. Brown, S.G. Napholtz, J.L. Zilko, and A. Lahav, *Appl. Phys. Lett*. Vol. 54, 2306 (1989).
18. A.R. Goodwin, I.G.A. Davies, R.M. Gibb, and K.H. Murphy, *J. Lightwave Technol*. Vol. 6, 1424 (1989).
19. A. Katz, B.E. Weir, S.N.G. Chu, P.M. Thomas, M. Soler, T. Boone, and W.C. Dautremout-Smith, *J. Appl. Phys*. Vol. 67 (8), 3872 (1990).
20. A. Katz, S.N.G. Chu, B.E. Weir, C.R. Abernathy, W.S. Hobson, S.J. Pearton and W. Savin, *IEEE Transactions on Electron Devices*, Vol. 39, No.1, January 1992.
21. T. Wolf, T. Zinke, A. Krost, D. Bimberg, *1993 IEEE 5th International Conference on Indium Phasphide and Related Materials, 93 IEEE 5 Int Conf Indium Phosphide Relat Mater 1993*. Publ by IEEE, IEEE Service Center, Piscataway, NJ, USA, p707-710.
22. K. Nagata, O. Nakajima, and J. Ishibashi. *Jpn. J. Appl. Phys*. Vol. 25, L510 (1986).
23. G.E. Bulman, G.F. Guillian III, and F.A. Chambers, *J. Electrochem. Soc*. Vol. 136, 2423 (1989).
24. R.F. Broom, H.P.Meier, and W. Walter, *J. Appl. Phys*. Vol. 60, 1832 (1986).
25. A. Katz, B.E. Weir, and W.C. Dautremont-Smith, *J. Appl. Phys*. Vol. 68 (3),1123-1127 (1990).
26. B. Sartorius, M. Schlah, M. Rosenzweig and K. Parschke, *J. Appl. Phys*. Vol. 63, 4677 (1988).
27. W.O. Barnard, J.B. Malherbe, F.D. Auret and G. Myburg, *Thin solid Films,* Vol. 215, 42(1992).
28. G. Qwilkinson, Ed., in: *Comprehensive Co-ordination Chemistry,* Vol. 3 (Pergamon, Oxford, 1987) p.279.
29. T.B. Massalski, Ed., in: *BinaryAalloy Phase Diagrams*, American Society for Metals, Metals Park, OH, 1987.
30. A. Katz, S. Nakahara, W. Savin, and B.E. Weir, *J. Appl. Phys.*, Vol. 68, p.4133, (1990).
31. A. Katz, S.N.G. Chu, B.E. Weir, W.C. Dautremont-Smith, R.A. Logan, and T. Tanbunek, *J. Appl. Phys.*, Vol.68 p.4141 (1990).
32. S.N.G. Chu, A. Katz. T. Boone, P.M. Thomas, V.G. Riggs, W.C. Dautremont-Smith, and W.D. Johnston, Jr., *J. Appl. Phys.*, Vol. 67, p.3754 (1990).
33. A. Katz, C.R. Abernathy, S.J. Pearton and B.E. Weir, *J. Appl. Phys.*, Vol.69 p.2276 (1991).
34. A. Katz, B.E. Weir, and W.C. Dautremout-Smith, *J. Appl. Phys.*, Vol. 67, p.1123 (1990).
35. D.G. Ivey, P, Jian, Robert Bruce, Gordon Knight, *J. Mater. Sci.: Mater. in Electronics*, Vol. 6 219-227 (1995).
36. T. Oshni, N. Yokyama, H. Onodera, S. Suszuki, and A. Sbatomi, *Appl. Phys. Lett.*, Vol. 43, 600 (1983).

37. N. Yocomaya. T. Oshini, H. Onodera, and M. Abe, *IEEE Trans. Electr. Dev.*, Vol. ED-29, 1541 (1982).
38. Naaki Yokoyama, Toyokazu Onishi, and Hiroyuki Onodera, *IEEE Journal of Solid State Circuits*, Vol. Sc-18, 520 (1983).
39. M. Suzuki, and Y. Kuriyama, *IEEE Electr. Device Lett.*, Vol. EDL-6, 542 (1985).
40. J.R. Wardrop, *J. Appl. Phys.*, Vol. 41, 350 (1982).
41. E.Y. Chang, Y. Lai, K. Lin, C. Chang, and F.Y. Juang, *Mat. Res. Soc. Symp. Proc*. Vol. Vol. 300, 279-284 (1993).
42. A. Katz, *Indium Phosphide and Related Materials: Processing, Technology, and Devices.* Chpter 9, P307-335.
43. *ASM Handbook Vol. 3, Alloy Phase Diagrams,* ASM International The materials Information Society, 1992.

Table 4-1: Indexing of SAD pattern in Figure 4-10c

Experimental	Ti_4P_3		TiP	
d (nm)	d(nm)	h k l	d (nm)	h k l
0.306			0.303	1 0 0
0.297			0.293	1 0 1
0.272			0.269	1 0 2
0.259	0.2628	2 2 0		
0.238	0.2349	3 1 0	0.239	1 0 3
0.212			0.210	1 0 4
0.188	0.1985	3 2 1	0.185	1 0 5
0.176			0.175	1 1 0
0.166	0.1662	4 2 0	0.164	1 0 6
0.148	0.1517 0.1457	4 2 2 5 1 0	0.150 0.147 0.146	1 1 4, 2 0 1 2 0 2 1 0 7, 0 0 8
0.128	0.1205	6 1 1	0.127	2 0 5
0.113	0.1175 0.1146	6 2 0 5 4 1	0.112	2 0 7 1 1 8

Note: Ti_4P_3 is cubic with a=0.743 nm. TiP is hexagonal with a=0.349 nm & c=1.165 nm. Diffraction patterns were taken from a specimen annealed at 350°C for 2 hrs.

Table 4-2: Indexing of SAD pattern in Figure 4-12b.

Experimental	Ti_4P_3		TiP	
d (nm)	d(nm)	h k l	d (nm)	h k l
0.585			0.585	0 0 2
0.309			0.303	1 0 0
0.297			0.293	1 0 1
0.271	0.2628	2 2 0	0.269	1 0 2
0.241	0.2349	3 1 0	0.239	1 0 3
0.215			0.210	1 0 4
0.188	0.1985	3 2 1	0.185	1 0 5
0.177	0.1662	4 2 0	0.175	1 1 0
0.165	0.1517 0.1457	4 2 2 5 1 0	0.164	1 0 6
0.153			0.150	1 1 4 2 0 1

Note: Ti_4P_3 is cubic with a=0.743 nm. TiP is hexagonal with a=0.349 nm & c=1.165 nm. Diffraction pattern was taken from a specimen annealed at 450°C for 1.5 hrs.

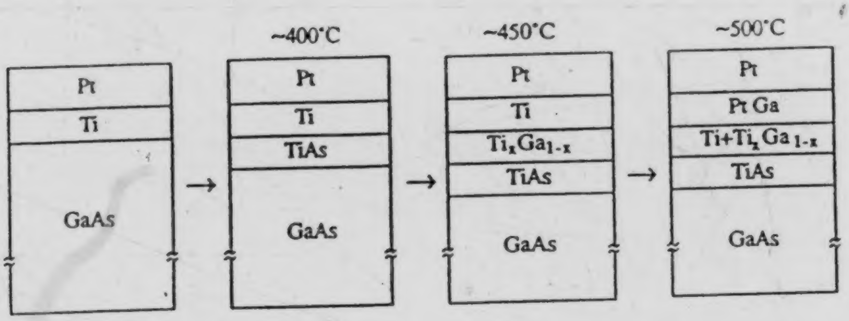
Pt
Ti
GaAs
~400°C
Pt
Ti
TiAs
GaAs
~450°C
Pt
Ti
Ti_xGa_{1-x}
TiAs
GaAs
~500°C
Pt
Pt Ga
$Ti+Ti_xGa_{1-x}$
TiAs
GaAs

Fig. 4-1. Schematic illustration of alloying sequence of Pt/Ti metallization to p^+-GaAs [11].

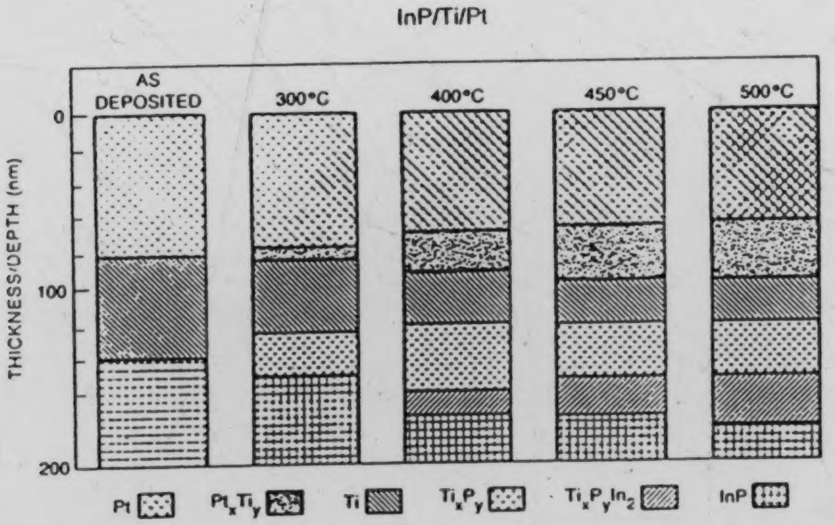
InP/Ti/Pt
AS DEPOSITED
300°C
400°C
450°C
500°C
THICKNESS/DEPTH (nm)
0
100
200
Pt
Pt_xTi_y
Ti
Ti_xP_y
$Ti_xP_yIn_z$
InP

Fig. 4-2. Schematic representation of the layer composition and thickness of Pt (60 nm)/Ti (50 nm) contacts to InP, in the as-deposited conditions and after RTP at 300, 400, 450 and 500°C for 30 sec [20].

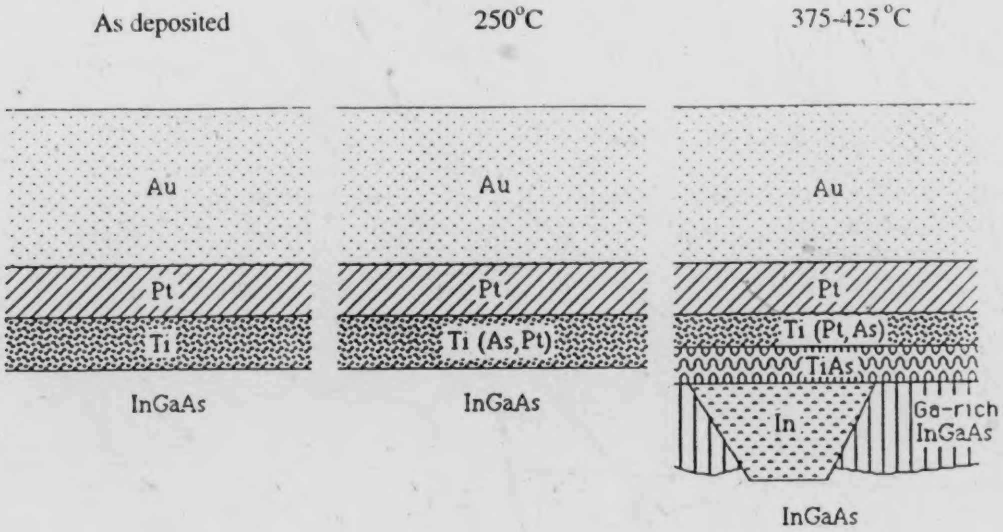
As deposited
250°C
375-425 °C
Au
Pt
Ti
InGaAs
Au
Pt
Ti (As,Pt)
InGaAs
Au
Pt
Ti (Pt,As)
TiAs
In
Ga-rich InGaAs
InGaAs

Fig. 4-3. Schematic representation of the reactions that occur during annealing of Ti/Pt/Au contacts to InGaAs.

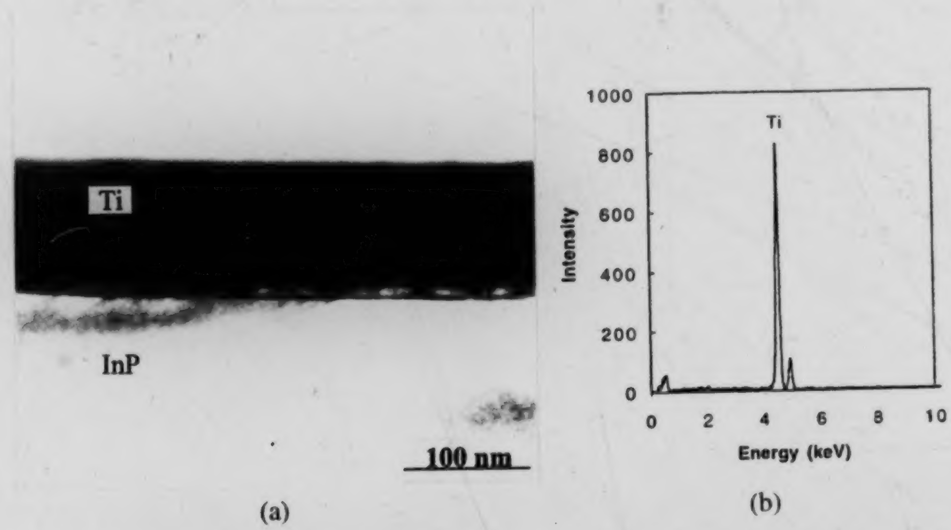

(a) (b)

Fig. 4-4 (a)Bright field micrograph of an as deposited cross section specimen showing that the thickness of Ti film is about 120 nm. (b) EDX spectrum of the as deposited Ti layer.

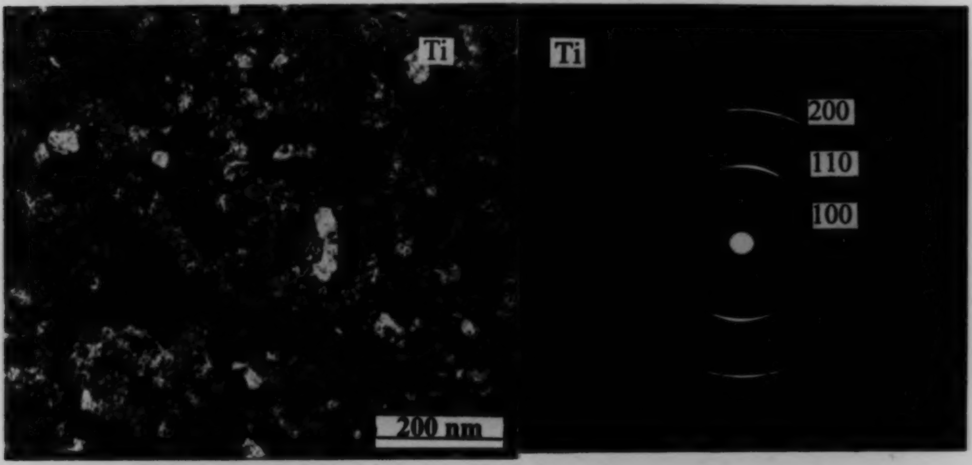

Fig. 4-5 (a) Bright field micrograph of an as deposited plan view specimen showing that the grain size is approximate 25 nm. (b) SAD diffraction pattern from the as deposited plan view specimen showing the Ti film is <001> preferentially oriented.

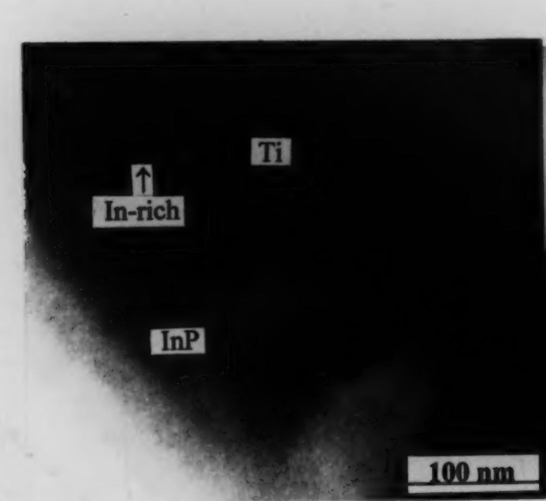

Fig. 4-6 Bright field micrograph of a cross section specimen annealed at 325°C for 5 minutes. Two regions, exhibiting different contrast are shown.

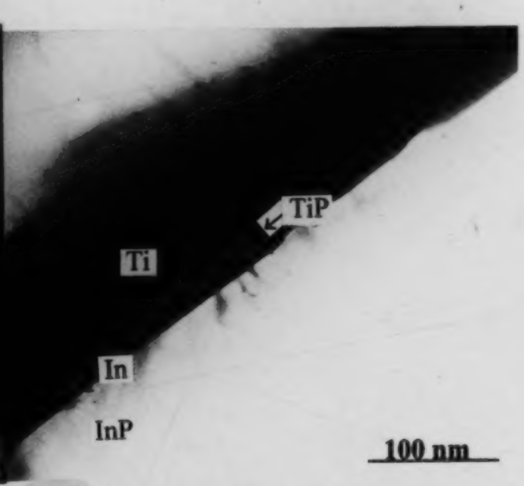

Fig. 4-8 Bright field micrograph of a cross section specimen annealed at 350°C for 2 hrs.

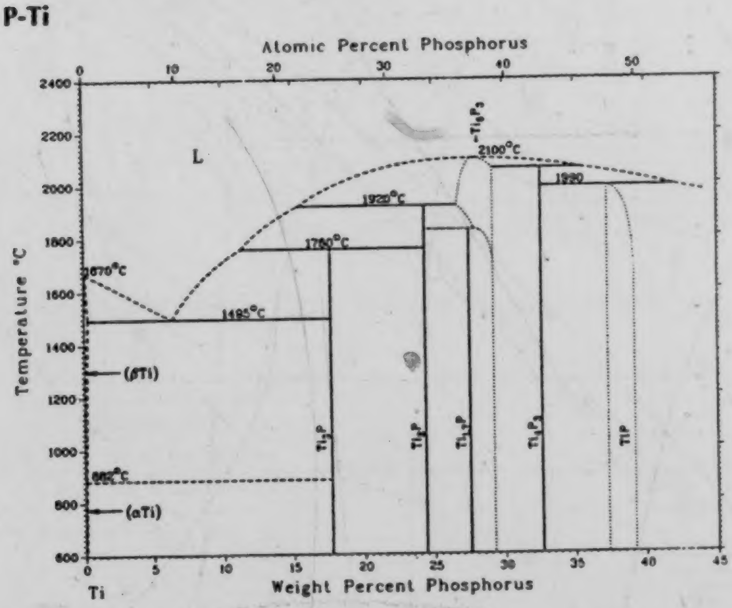

Fig. 4-7 Ti-P phase diagram showing that solubility of P in Ti is very low [43].

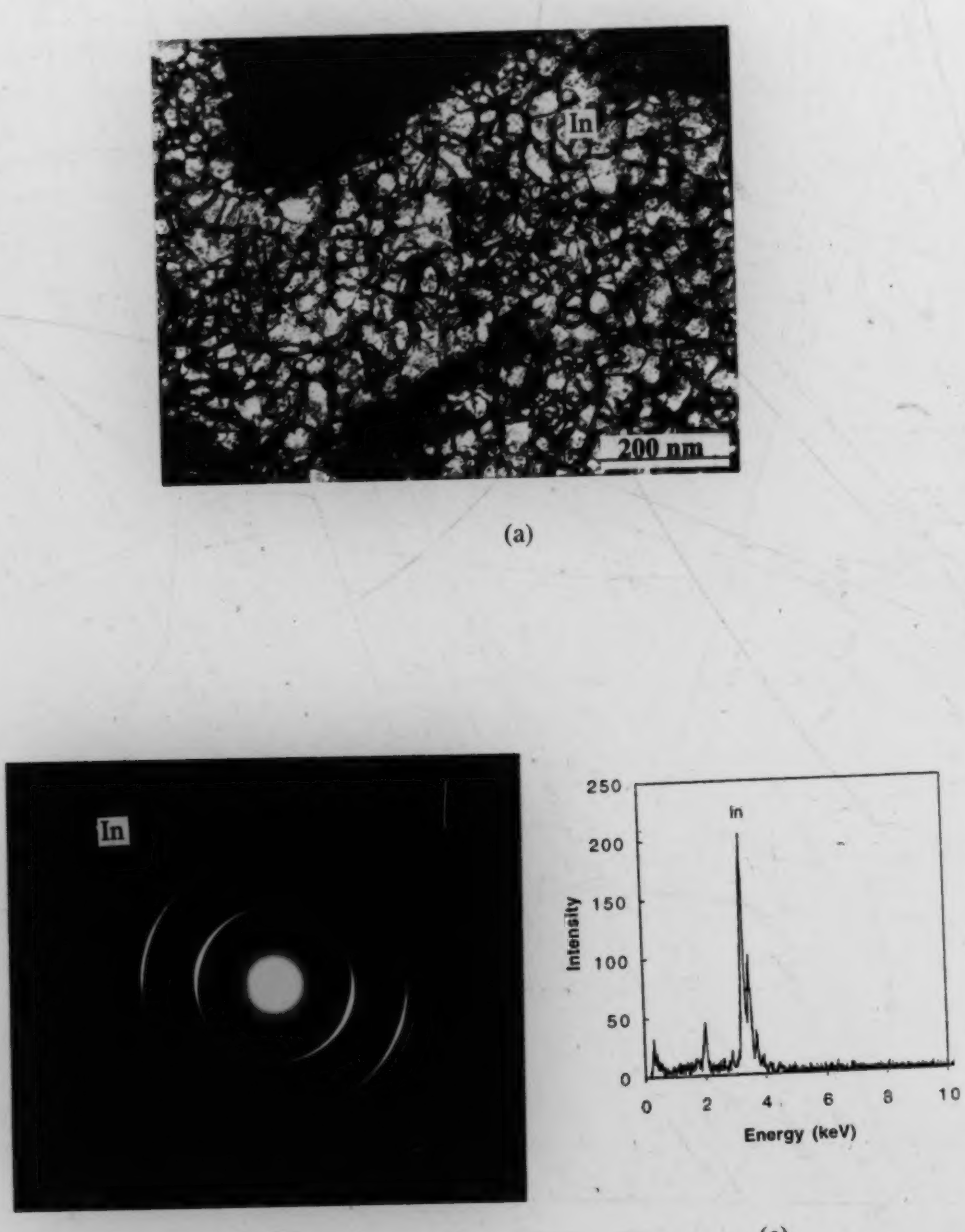
In
200 nm
In
250
200
150
100
50
0
Intensity
In
0
2
4
6
8
10
Energy (keV)

(a)

(b)

(c)

Fig. 4-9 (a) Bright field micrograph of the inner layer (In) from a plan view specimen annealed at 350°C for 2 hrs. (b) Diffraction pattern and (c) EDX spectrum from (a).

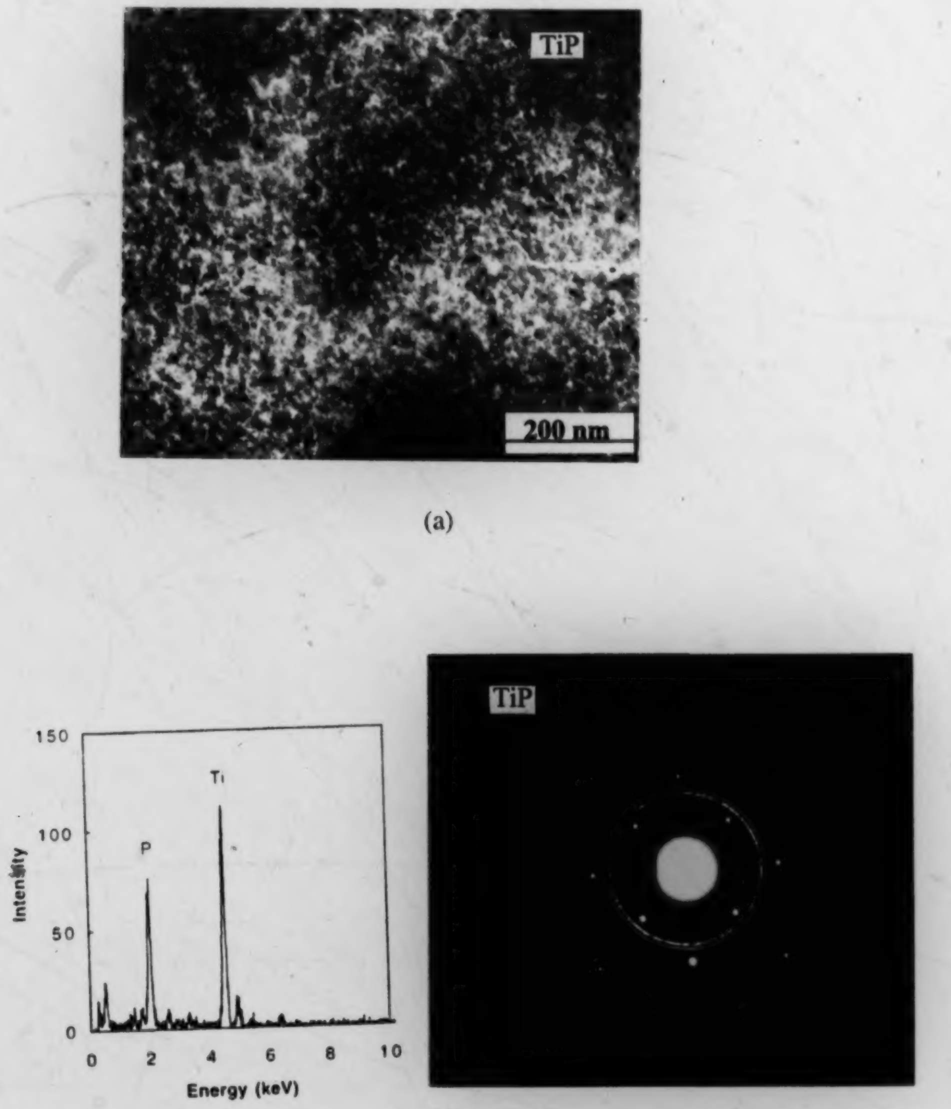
TiP
200 nm
150
100
50
0
Intensity
P
Ti
0
2
4
6
8
10
Energy (keV)
TiP

(a)

(b)

(c)

Fig. 4-10 (a) Bright field micrograph of Ti-P compound from a plan view specimen annealed at 350 °C for 2 hrs. (b) EDX spectrum from the Ti-P compound, and (c) SAD pattern showing that the Ti-P compound is TiP.

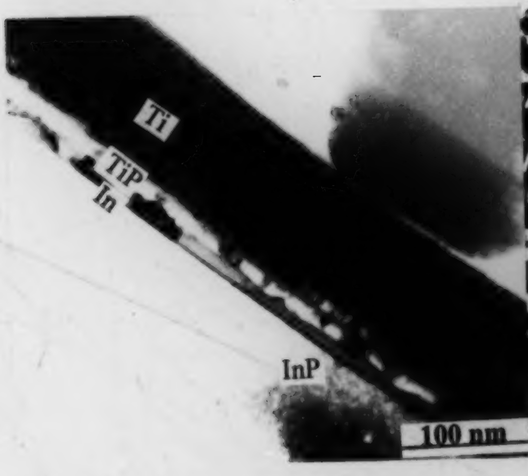
Ti
TiP
In
InP
100 nm

Fig. 4-11 Micrograph of a cross section specimen annealed at 450°C for 1.5 hrs.

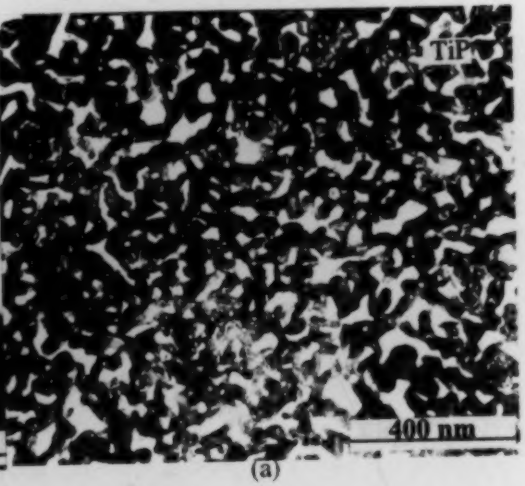

(a)

Fig. 4-12 (a) Micrograph of the Ti-P layer from the plan view specimen annealed at 450°C for 1.5 hrs.

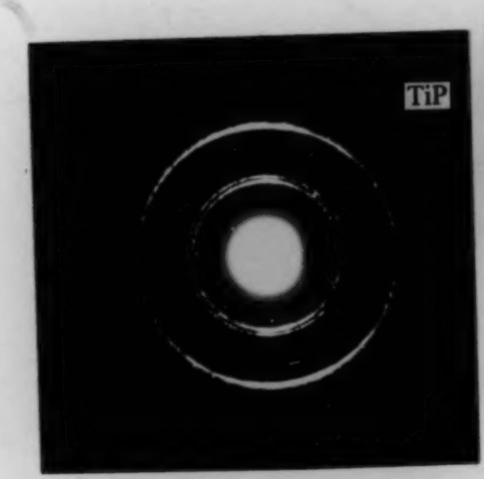

(b)

Fig. 4-12 (b) SAD pattern from (a) indicates that the Ti-P compound is TiP.

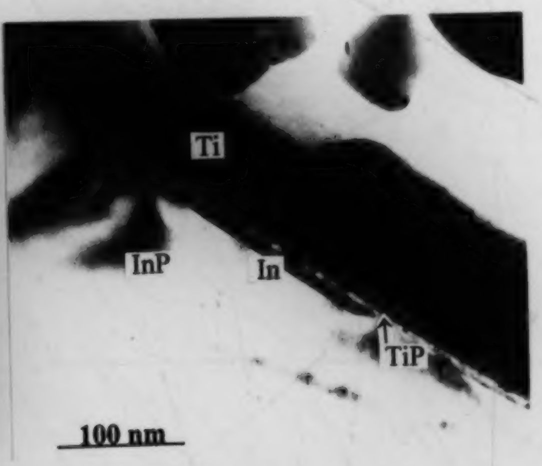
Ti
InP
In
TiP
100 nm

Fig. 4-13 Bright field image of Ti/Pt/Au-InP cross section specimen annealed at 400°C for 2 min.

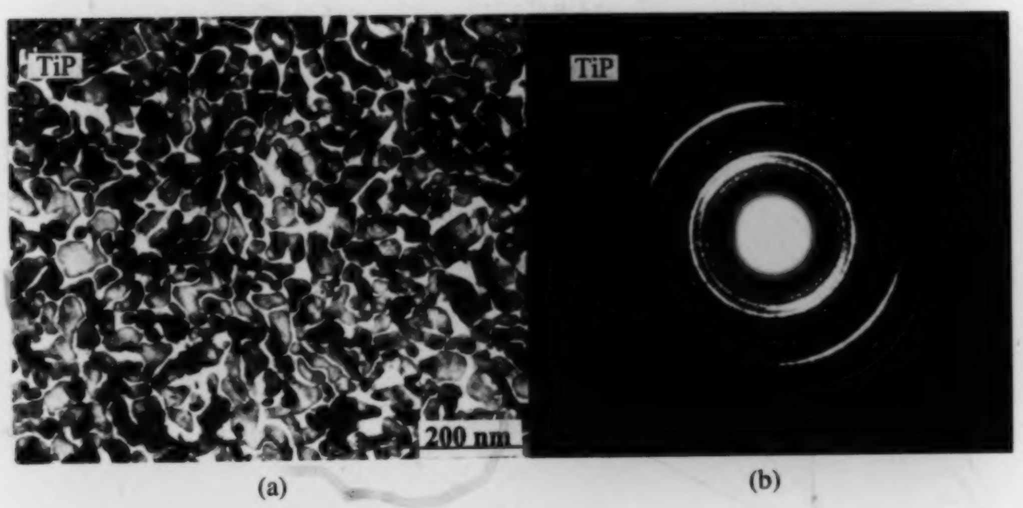

(a) (b)

Fig. 4-14 (a) Bright field micrograph of the TiP layer from a plan view specimen annealed at 550°C for 30 min. (b) SAD pattern from (a).

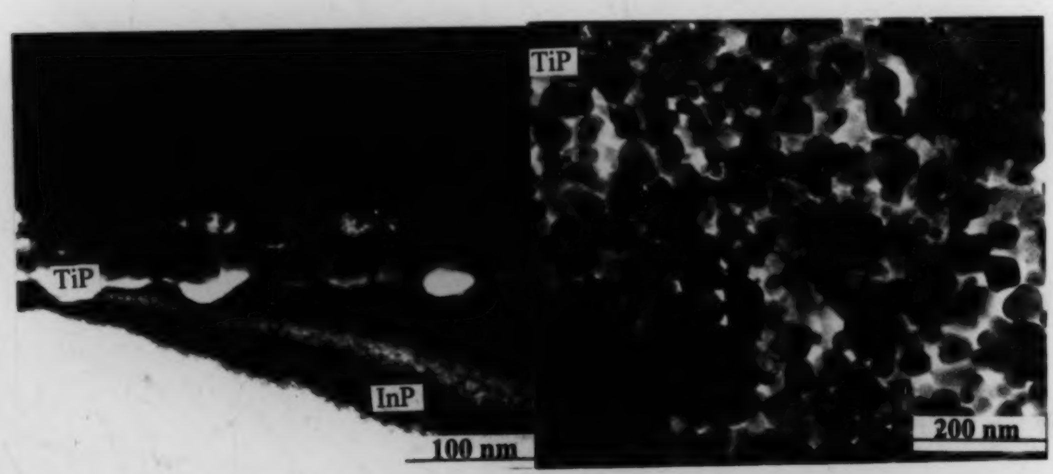

(a) (b)

Fig. 4-15 (a) Bright field image of a cross section specimen annealed at 550°C for 4 hrs. (b) Micrograph of the TiP layer from a plan view specimen annealed at 550 °C for 4hrs.

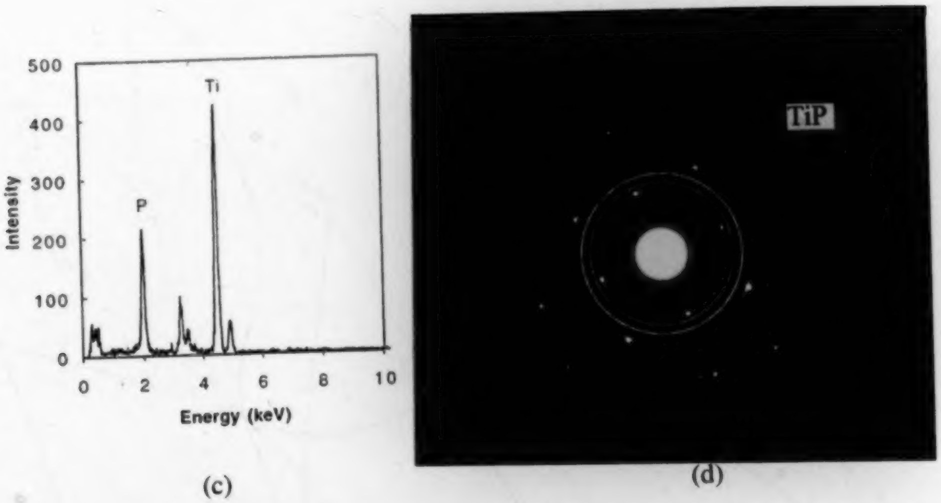

(c) (d)

Fig. 4-15 (c) EDX spectrum from the grains of TiP and (d) SAD pattern from the region shown in (b) indicate that the Ti-P compound is TiP.

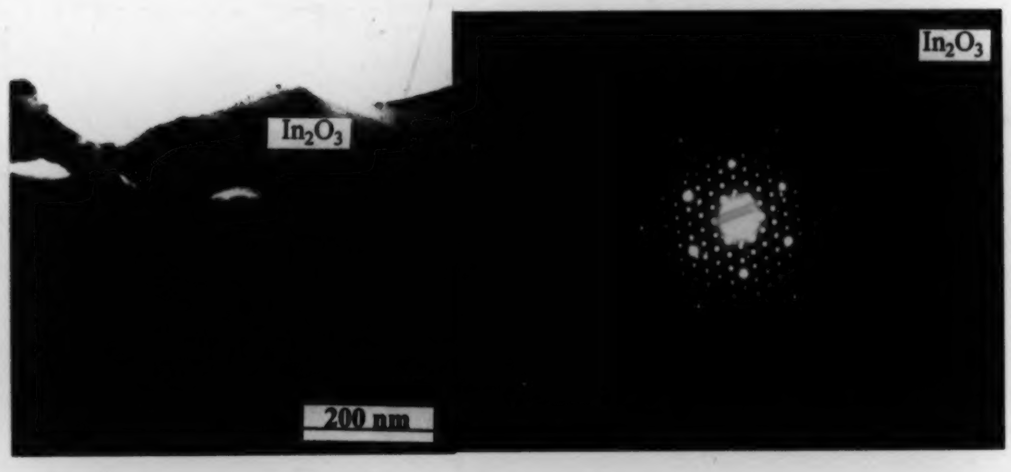

(a) (b)

Fig. 4-16 (a) Micrograph of a cross section specimen (the top of the film) annealed at 550°C for 4 hrs. (b) CBED pattern from the region shown in (a) indicating that In was oxidized to form In_2O_3.

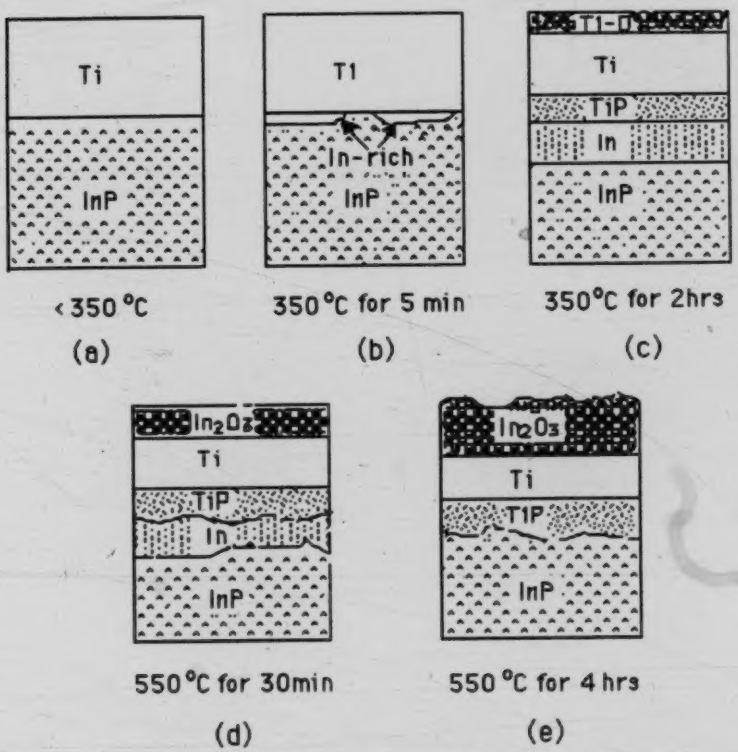
Ti
InP
<350 °C
(a)
Ti
In-rich
InP
350 °C for 5 min
(b)
Ti-O
Ti
TiP
In
InP
350°C for 2hrs
(c)
In2O3
Ti
TiP
In
InP
550 °C for 30min
(d)
In2O3
Ti
TiP
InP
550 °C for 4 hrs
(e)

Fig. 4-17 Schematic representation of reactions between Ti films and InP substrate.

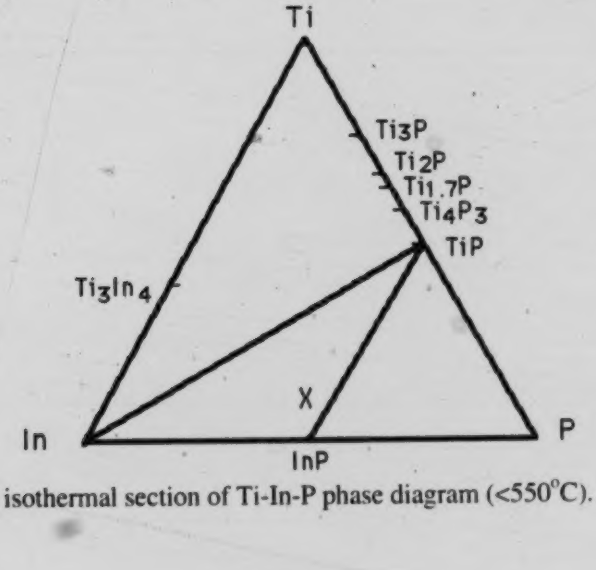
Ti
Ti3P
Ti2P
Ti1.7P
Ti4P3
TiP
Ti3In4
X
In
InP
P

Fig. 4-18 Predicted isothermal section of Ti-In-P phase diagram (<550°C).

Chapter 5

Ohmic Contact Formation in Ge/Ni Metallizations to n-type InP

5-1 Ni-based metallizations

Ni-based metallizations are utilized in ohmic contacts to n-type InP. Ni-based multilayer metallizations consisting of, besides Ni, Au or Au and Ge with various arrangements of the multilayers have been widely studied. Au/Ge/Ni metallizations to n-type InP are one of the most commonly used contacts. Many efforts [1-12] have been made to reveal the mechanism of ohmic contact formation and bridge the relationship between the contact structures and electrical properties. The result reported in the studies [1-12] is a variation in the reaction products, morphology and electrical properties. Since Ni appears to play an important role in the onset of ohmic behavior, this chapter will start with a review of Ni/InP metallizations and then Ni-based contacts to InP, and focus on Au/Ge/Ni metallizations to InP.

5-1-1 Ni/InP contact

Nickel is a common metal in ohmic contacts to InP. This is, in part, because it shows potential on its own to form an ohmic contact to n-type InP. For instance, specific contact resistances as low as $10^{-6}\ \Omega\text{-cm}^2$ have reported for a directly evaporated Ni_2P film on InP ($8\times10^{18}cm^{-3}$) [13].

It has been reported that Ni can act as a p-type dopant [14-16], by diffusing into the surface layer of the InP during annealing to form a p+ region. A highly doped region would then reduce the width of the depletion layer associated with the potential barrier formed at the metal/semiconductor interface. Tunneling of charged carriers in both directions across the interface would then be possible making the contact essentially ohmic. However, whether a Ni metallization to n-type InP would compensate the n-type doping and consequently increase the specific contact resistance or ruin the ohmic behaviourhas not been reported.

Another important role played by Ni is in improving the wetting characteristics of multilayer metallizations (e.g., Au/Ge), thereby lowering the contact resistance [17].

Reactions involving Ni films on n-type InP during annealing at 200-500°C in forming gas (5%H_2, 95% N_2) [18-20] or helium [16] have been reported by several groups.

Work done by Sands [19] on SiO_2 capped Ni films on InP indicates the formation of an amorphous ternary phase at the Ni/InP interface during low temperature annealing (~200°C). The composition of the ternary amorphous phase is approximately 2.7Ni :1In :1P.

Annealing at 300 °C resulted in dendritic growth of large randomly oriented grains (several microns in diameter) of a hexagonal Ni_xInP phase ($2 \le x \le 3$) (a= 0.412nm c= 0.483nm). After annealing at 360°C for 60 min, an additional ternary phase Ni_2InP was identified. This was determined, through electron diffraction, to be monoclinic with a= 0.681nm, b= 0.529nm, c= 1.280nm and β= 95°. This phase was stable up to 500°C.

Fatemi and Weizer[18] have reported that two phosphides, Ni_2P and Ni_3P form during annealing (≅400°C) of Ni/InP couples in forming gas. Long term annealing (~40 min) results in the decomposition of Ni_3P, leaving only Ni_2P. Phase identification was carried out using EDX and AES.

Appelbaum et al. [16] studied Ni/InP reactions (annealed in He) using Auger analysis. An intermixed region containing Ni, In and P formed during annealing to 250°C (< 60 min), with In and P uniformly distributed in the Ni layer. This intermixed region is quite likely the same amorphous phase detected by Sands et al [19]. A Ni-P rich region and Ni-In-rich mixture, with some P in the outer layer, were detected in a specimen annealed at 250°C for 90 min or at higher temperatures for shorter times, i.e., 300°C for 10 to 60 min. Accordingly, this phenomenon is considered to be phase separation to form a Ni_2P layer and a Ni-In phase. Annealing at 400°C resulted in Ni_2P formation and metallic In diffusion to the surface. Appelbaum also reported the presence of a ternary phase (cubic with a= 0.57nm) of undetermined composition after annealing at 400°C in forming gas. In other study, a binary Ni_2In phase was proposed to form in a Ni-In/Ni-P/InP system also exposed to a helium ambient [20].

Because of the limitation of depth profiling using Auger analysis, phase identification is inconclusive. Differential sputtering rates during analysis can lead to misinterpretations. In addition, no structure information is available.

According to the discussion above, reactions at Ni/InP interface are different from research group to group, even though the same annealing conditions (temperatures and time) were claimed. Differences could be attributable to different annealing ambients and possibly different metallization schemes. For instance, Stremsdoerfer et al [20] showed that if the annealing was carried out in an open-tube furnace with flowing dry nitrogen, the first phase to form is Ni_3P which then changes to Ni_2P. A more significant cause for the differences may lie in the uncertainties associated with the analytical techniques utilized.

Recently, an investigation of the Ni/InP system was reported by Mohney and Chang [21]. According to their early study on the Ni-In-P system, Ni_2InP is in thermodynamic equilibrium with InP at 470°C [22]. Ni_2InP was identified to be monoclinic with a= 0.6795 nm, b= 0.5269 nm, c= 0.6436 nm and β= 94.73° [21]. The ternary phase is similar to the one reported by Sands et al [19], the main difference being the c parameter . The difference of a factor of 2 in parameter c is suggested to be caused by the formation of a superlattice structure. Thus, Ni_2InP would be expected to be in equilibrium with InP after Ni is completely consumed in a thin film Ni/InP system. In order to bridge the gap between different research results, bulk Ni/InP diffusion couples were examined after annealing at 470-600°C for upto to several months. The layer sequence in all couples was found to be Ni/NiIn/Ni_2P/InP. No Ni_xInP was observed. The explanation for this, according to Mohney and Chang [21], is that ternary phases form in thin film couples because their composition is close to that phase. Distribution of the III, V elements is not required. These kinds of ternary phases do not necessary persist, however, as the diffusion evolves. Studies of thick film Ni/InP (300 nm or 500 nm) systems shows that the amorphous layer has an approximate composition of $Ni_{2-3}InP$ in the initial stage of reaction at 250°C. Annealing at higher temperatures, up to 450°C for 30 s, did not result in any ternary phase formation.

Ohmic behaviouris determined by the types of phases that form at the metal contact/semiconductor interface. Ohmic behaviourhas been achieved for Ni/InP contacts consisting of nickel phosphides. Appelbaum et al [16] found that sputtered Ni_2P layers form ohmic contacts to n-type InP, with low specific contact resistance (3×10^{-6} Ω-cm^2, n= $8\times10^{18}cm^{-3}$). This implies that additional dopants are not necessary to obtain low specific contact resistance, thereby eliminating the need for a high temperature electrical activation treatment.

Weizer et al. [23] reported that the low contact resistance in Ni/InP contacts is due to Ni_3P formation in the interface adjacent to InP. They argued that in Ni-InP contacts annealed at 400°C for a few minutes, the r_c drops from the as deposited value in the low $10^{-4}\Omega$-cm^2 range to a minimum value in the mid $10^{-7}\Omega$-cm^2 range, This is due to Ni_3P in direct contact with InP. Further heat treatment results in an increase in contact resistance back to the $10^{-4}\Omega$-cm^2 range because the Ni_3P layer at the Ni/InP interface changes to Ni_2P.

The effect on electrical properties, of Ni/InP contacts, due to only the ternary phase has not yet been reported.

5-1-2 Au/Ge/Ni-GaAs contacts

Since most ohmic contacts to n-type InP are based on successful ohmic contacts to GaAs, it is useful to summarize the main features of interfacial structures of AuGeNi ohmic contacts to GaAs.

Au/Ge/Ni is widely used as a metallization scheme in ohmic contacts to GaAs. A great deal of research on the metallurgical structure and the electrical properties of AuGeNi/GaAs contacts [24-34] has been done. Contact microstructures vary depending on the deposition sequence, formation techniques and annealing conditions. As with other contact systems, results vary from research group to research group. Some of the common features are briefly discussed below.

a. Contact design

Traditional metallization structures for this contact system consist of the deposition of eutectic (12.5wt% Ge) Au-Ge alloy and a nickel layer of various thicknesses, with either the Au-Ge alloy layer or the Ni layer adjacent to the semiconductor.

Nickel is added to maintain a smooth surface morphology during the alloying process. Nickel can also enhance the diffusion of Ge into the semiconductor, facilitating the reaction of Au with the semiconductor. Nickel improves the wetting characteristics of AuGe and lowers the contact resistance [35].

Gold is necessary for bonding wires to the external circuit and acts as a protective, non-oxidizing layer for the metallization during annealing. Gold also lowers the contact resistance in n-type contacts to GaAs. On the other hand, gold will dissolve GaAs, primarily Ga. The solubility of Ga in Au increases with increasing temperature [36]. The Au-Ga reaction also results in the formation of Au-Ga compounds, once the solubility is reached, that have low melting points [37]. The presence of an Au-Ga eutectic at 340^{o}C implies that partial or complete melting may occur during annealing above this temperature, resulting in a non-uniform interface or rough surface morphology.

Ge in the Au-Ge-Ni system plays a crucial role in reducing r_c to very low values on GaAs [37,38]. The mechanism involves Ge diffusion into GaAs to occupy Ga sites, which locally makes GaAs more n-type. Thus, a tunneling ohmic contact forms resulting in low specific contact resistance.

b. Metallurgical reactions and ohmic behaviour[25,27-32]

Reactions among the metallizations and GaAs are as follows:

(i) At temperatures < 300°C, Ge reacts with Ni to form NiGe or Ni_3Ge, with Ni and Au diffusing toward the GaAs substrate. The contacts are not ohmic at this stage.

(ii) At temperatures from 300 to 400°C, GaAs decomposes through the interaction between Au and Ga, as well as its reaction with Ni. The reaction products are Au-Ga phases (including a Au (Ga,As) solid solution phase, β-AuGa. Au_7Ga_2 [29]), NiAs and NiGe. The contact resistance is still high ($>10^{-4}\Omega\text{-cm}^2$).

(iii) At 400-500°C, additional Ge, which is present in NiGe, diffuses towards NiAs and GaAs to form Ni_2AsGe or NiAs(Ge), or enters Ga sites in the GaAs crystal forming a heavily doped n-type layer. The morphology of the contact consists of binary β-AuGa grains and Ni_2AsGe (or NiAs(Ge)) grains. Ohmic character is attained beginning at ~400°C [29]. The lowest contact resistance ($<10^{-6}$ $\Omega\text{-cm}^2$, $N\approx10^{18}\text{cm}^{-3}$) is observed at temperatures between 400-500°C. Higher annealing temperatures also result in the melting of β-AuGa (~375 °C), giving in poor contact morphology, which can affect the electrical properties.

(iv) At > 600°C, or lower temperatures for longer annealing times (for instance, 400°C for 90 hours), the contact resistance increases due to NiAs(Ge) grain growth, reducing the contact area between the NiAs(Ge) grains and GaAs substrate.

The NiAs(Ge)/GaAs interface is believed to be important in lowering the contact resistance, because the contact resistance is inversely proportional to the area fraction of the NiAs(Ge)/GaAs interface [25]. The exact mechanism is still not clear, however, a heavily doped n^+ GaAs layer is believe to be formed at the interface by the diffusion of Ge from NiAs(Ge) across the boundary. The uniformity of the contact metal/GaAs interface affects the spread in resistance values. An ideal interface structure for a Au/Ge/Ni-GaAs ohmic contact is one with a two-layer structure [27], with a high density of the NiAs(Ge) grains in the bottom layer contacting GaAs and a homogeneous β-AuGa phase in the top layer. β-AuGa plays an important role in the reduction of the contact resistance after contact formation. The formation of β-AuGa creates Ga vacancies in the GaAs substrate near the surface, which are needed for Ge doping. Therefore, β-AuGa compounds are considered to be essential for reduction of the contact resistance of AuGeNi ohmic contacts. However, due to its low melting point, formation of low melting point β-AuGa compounds at the interface causes deterioration of the electrical properties and surface morphology of AuGeNi contacts. AuGeNi contacts are thermally unstable at temperatures above 350°C even though the contacts are prepared at temperatures higher than 400°C [31,32]. Values of specific contact resistance (r_c) for several AuGeNi contacts to n-type GaAs are summarized in Table 5-1.

5-1-3 Au/Ge/Ni-InP contacts

Au/Ge/Ni contacts are the most common contacts to n-type InP. As mentioned above, the structure is based on similar successful contacts to n-type GaAs. Various arrangements have been studied, such as Ni/Au-Ge/InP [1,2], Ni/Au/Ge/InP [16-18], Au/Ni/Ge/Ni/InP [7,8], Au/Ni/Au-Ge/InP [9,10] and Au/Ge/Ni/InP [6,23,24]. (The deposition sequence is such that the first metal listed is furthest from the InP substrate. "Au-Ge" means deposition of both elements from different sources simultaneously, and in most cases the Ge content is 12 wt.%, which is the eutectic composition with Au.)

The general features of AuGeNi/InP contacts, from the above references, can be summarized as follows:

(i) Ge moves from the Au-Ge (which is touching InP) or Ge layer to the Ni layer to form GeNi [1,3], or Ge diffuses into InP substrate [2].

(ii) Ni, when in contact with InP, reacts with InP at low temperatures (<250°C) to form a Ni-rich ternary amorphous phase. In the case where Ni is at the metallization surface, it diffuses through the metallization layer toward the surface of the InP substrate and reacts with InP to form Ni_2P, Ni_xInP [3,6] or exists as a single layer adjacent to InP [3].

(iii) P outward diffusion from InP takes place, which may lead to binary compound formation with Au [2] and Ni [24]. For example, Au_2P_3 (a= 0.586 nm, b= 1.4439 nm, c= 0.467 nm and β=108.39) has been claimed to form [5], as well as Ni_2P and NiP [24]. Ternary reaction products, i.e., AuGeP have also been reported [6], as has P evaporation [2].

(iv) In, produced by decomposition of InP, diffuses outward to the Au layer, Reaction products between In and Au had not been conclusively identified until a recent study was published [55].

(v) Au migrates to the InP substrate and reacts with In to form various binary compounds.

Reaction products claimed in some publications are questionable due to the characterization techniques utilized. Anderson's group [5] has taken the advantages of TEM technique in their study of a Ni/Au/Ge/InP system (r_c= $3x10^{-5}$ Ω-cm^2 for a initial doping level of $3x10^{16}$ cm^3), i.e., phase identification is conclusive. Unfortunately, cross sections were not prepared for TEM examination in their studies. Therefore, interfacial structures were not reported. An interfacial structure model was proposed (see Figure 5-1), however, in which Au_2P_3 (possibly mixed with GeNi) extends into InP, while a Au-Ge-P phase and Ni are adjacent to each other, with Au(In) on top.

Specific contact resistances for the different systems mentioned above are listed in Table 5-2. Factors that affect contact resistance have been suggested. The work done by Erickson [3] (for a Ni/Au/Ge/InP system) showed that Ni plays an important role in reducing r_c. Anderson's group [5] utilized TEM in their study on the same system. They pointed out that large Au_2P_3 particles offer a conduction path of lower resistance, since there was a dramatic change in the temperature dependence of the resistance when those particles were present in the interfacial layer. The work done by Graham *et al* [6] on the Au/Ge/Ni /InP system (Ni in contact with InP) using high-resolution luminescence showed that Au_2P_3 exhibits metallic conductivity, playing an important part in contact ohmic properties. In the investagation of the Ni/Au-Ge system [1], Ni, AuGe or more complex compounds are proposed as responsible for the ohmic contact formation at 300°C.

As mentioned above, Ge is proposed to act as a dopant to made InP more n-type, leading to lower specific contact resistance values. Graham *et al* [6] used high-resolution luminescence to investigate the nature of n-type InP directly beneath a AuGeNi ohmic contact (Ni in contact with InP), annealed at various conditions. Cathodoluminescence (CL) showed that the underlying InP is significantly modified up to distances of several microns from the contact interface, due to the interaction of the contact components with the semiconductor. No evidence of the anticipated n^+ doping was obtained, although Ge was present several microns into InP.

Other researchers claim that Ge is not necessary to achieve low contact resistances [4,16]. Heat treated Ni-InP and Au/InP systems had contact resistances in the low 10^{-7} Ω-cm^2 and low 10^{-6} Ω-cm^2 ranges respectively. Au-Ni/InP contact resistances are in the 10^{-8} Ω-cm^2 range. These valuse are comparable to those obtained for Au-Ge-Ni systems.

As to contact morphology, which is one of the important factors affecting the contact resistivity, excellent surface morphology and edge definition remained at up to 460°C in the Ni/Au-Ge system [1]. The smooth surface morphology of the contacts is believed to be due to solid state processes leading to Au-In and Au-P compound (the exact compounds were not determined) formation. Work done by Erickson [3] on the Ni/Au/Ge/InP system showed that higher temperature annealing resulted in increasingly non-uniform surface morphology and more scatter in the r_c data. However, annealing at 360 °C (which is the melting point of Au -Ge eutectic alloy) did not result in an abrupt change in electrical behavior.

Overall, the results for the Au-Ge-Ni system show a wide variation in the reaction products, morphology and electrical properties. This is mainly due to the difference in metallization schemes chosen for the experiments and the experiment methods utilized for the characterization of interfacial reactions. Most studies have been carried out using AES or RBS, while a few studies utilized TEM techniques. TEM techniques applied to cross section and plan view specimens, although less common and more difficult to perform, are better suited to thin film phase identification and interfacial reaction characterizations.

A recent study in our laboratory [55] on a Au (40nm)/Ge(50 nm)/Ni(25 nm) system to n-type InP (initially doped to a level of $1x10^{17}cm^{-3}$ with Si) using TEM showed conclusive results in phase identification and interfacial reactions. The study is summarized in the following and in the schematic in Figure 5-2.

(i) In the as deposited condition, the deposited Ge layer was amorphous, while between the Ge and polycrystalline Ni layer was an amorphous mixture of Ni and Ge. An amorphous ternary phase Ni_xInP (x=2-3) had formed adjacent to InP, indicating that Ni reacts with InP during deposition or at the low temperatures occurring during specimen preparation.

(ii) The Ge and Ge-Ni layer crystallized and the amorphous Ni_xInP layer grew during annealing at 250 °C. Small amounts of In diffused outward and dissolved in the Au layer.

(iii) Annealing at temperatures ranging from 325-400°C resulted in significant Au diffusion to the InP surface and thickening of the GeNi layer. Ni_xInP decomposed and was replaced by $Ni_2P(Ge)$ and $Au_{10}In_3$. Some Ni was retained. Indium outward diffusion resulted in the transformation of the Au layer to $Au_{10}In_3$.

(iv) Annealing at 400°C resulted in $Au_{10}In_3$ transformation to Au_9In_4 and Ni_2P transformation to NiP. NiP and GeNi were intermixed in the middle region of the metallization and were in contact with InP. Au_9In_4 was present at the InP surface in the form of islands.

Below 250°C the contacts were non-ohmic. Ohmic behaviourwas achieved at 325°C (r_c= $8x10^{-5}$ Ω-cm^2). A minimum specific contact resistance of 10^{-7} Ω-cm^2 was obtained at 400°C. The transition from non-ohmic to ohmic behaviourappears to correspond to the decomposition of the Ni-In-P (Ni_xInP) phase and the formation of Ni_2P and $Au_{10}In_3$ at the semiconductor surface. The attainment of minimum specific contact resistance values corresponds to the formation of NiP from Ni_2P and Au_9In_4 from $Au_{10}In_3$. The mechanism of ohmic contact formation may be due to Ge doping of InP as is often claimed by many researchers, because Ge is detected in Ni_2P which is in contact with InP. As mentioned above, it has been argued that Ge is not necessary to produce ohmic contacts and that Ni is more important. Neither barrier height lowering nor Ge doping alone can explain the behaviourof the contacts reported in [24]. The contact resistance decreased by almost three orders of magnitude (from r_c= $8x10^{-5}$ to 10^{-7} Ω-cm^2), when the annealing temperature was increased from 325 to 400°C. The attainment of ohmic behaviourat 325°C may be a result of a lower barrier height, due to interfacial contact between Ni_2P and InP. At temperatures above 350 °C, however, Ni_2P is no longer present, as it transforms to NiP. At this temperature, a substantial decrease in contact resistance occurred. In this case, Ge diffusion is likely more important (GeNi is in contact with InP).

The role of Au in these contacts is to drive the decomposition of the Ni-In-P ternary phase, in which In combined with Au (inward diffusion) to form Au-In low melting point binary compounds, resulting in contact laterally non-uniformity.

The work reported in the following section of the thesis is divided into two parts. In the first part, reactions between Ni thin films and InP are examined. The purpose is to gain a basic understanding of Ni/InP interfacial reactions.

In the second part, a Ge/Ni multilayer metallization to n-type InP is studied. This metallization is similar to the more conventional Au/Ge/Ni metallization, except that Au was removed in an attempt to improve contact stability and reliability. The atomic ratio of Ge/Ni was chosen to be slightly greater than 1. It was expected that this ratio would result in the formation of NiGe, as a thermally stable phase in contact with InP. A ratio<1 would result in the formation of additional Ni-rich Ni-Ge compounds. The excess Ge was expected to provide the necessary n-type doping.

5-2 Ni metallizations to InP

5-2-1 Experimental results and discussion

a. Ni/InP interfacial reactions

Ni reacted with InP during deposition to form an amorphous ternary phase (≈7-9 nm thick; Figure 5-3). The formation of an amorphous ternary phase has been reported previously by Sands *et al.* [19] for low temperature annealing (≈200°C) of 40nm Ni films on InP. Similar reactions have also been reported for Pd thin films on InP, which is another near noble metal/InP system [44,45]. The remaining Ni layer is approximately 50nm thick, indicating that the amount of deposited Ni was slightly more than the nominal thickness of 50nm. An SAD pattern from the Ni layer is also shown in Figure 5-3, indicating no preferred orientation of Ni grains. The Ni grain size was fairly uniform, with an average value of about 10 nm, determined from a plan view specimen.

Annealing of the films at low temperatures resulted in growth of the amorphous layer (≈30 nm at 190°C; Figure 5-4a), leading to complete consumption of the Ni by 250°C. A fairly uniform layer, 125-150 nm thick, is shown in Figure 5-4b for the sample annealed at 250°C for 30 min. Energy dispersive x-ray microanalysis (EDX) of the layer showed it to be fairly uniform with a composition corresponding approximately to Ni_3InP (Figure 5-4c). This is very close to the value reported by Sands *et al.* ($Ni_{2.7}InP$) [19].

The first signs of crystallization of the amorphous layer were apparent in samples annealed in the 250-300°C range. Several phases were identified, including a ternary phase which appeared to match the one reported by Sands *et al.* [19], i.e., Ni_2InP, and two binary phases, Ni_2P and In_2O_3. The crystallization process was, in fact, very much laterally non-uniform as indicated in the cross section TEM micrographs shown in Figure 5-5. Figure 5-5a shows a region from a cross section specimen that is entirely amorphous, with some In_2O_3 on the surface, Figures 5-5b and 5-5c show regions that are completely transformed, made up of Ni_2InP and In_2O_3 or Ni_2InP and Ni_2P. The TEM micrograph, from a plan view specimen (annealed for 5min at 280°C) in Figure 5-6, shows two regions. One area is made up of single crystalline Ni_2InP and a mixed area of polycrystalline Ni_2InP and Ni_2P. Ni_2InP lies next to the InP substrate (indicating that Ni_2InP likely initially nucleated at the amorphous layer/InP interface) and exhibits an orientation relationship with respect to the InP, i.e., [001] Ni_2InP // [001] InP (verified through both electron diffraction and XRD). Preferred orientation was also reported by Sands *et al.* [19]. The structure and orientation dependence of Ni_2InP will be discussed further in later paragraphs.

XRD analysis of samples annealed from 300-400°C indicated the same preferred orientation. The above examples illustrate the heterogeneous nature of the reactions and also emphasize the importance of examining both cross section and plan view specimens. Cross section specimens permit observation of samples parallel to the interface, but only provide a very limited field of view. Plan view specimens, on the other hand, provide a much better picture of the overall microstructure and phase distribution.

Annealing at 400°C resulted in very little change in microstructure. The same major phases (Ni_2P and Ni_2InP) were present, as is evident in the micrograph in Figure 5-7. The structure of Ni_2InP was studied in more detail in samples annealed at 400°C for 8 or 15 min, which will be discussed in later sections.

The highest annealing temperature employed was 500°C. The main change in microstructure was the partial decomposition of the ternary phase (Ni_2InP), resulting in additional Ni_2P formation and release of metallic In (Figure 5-8).

$$Ni_2InP \rightarrow Ni_2P + In \tag{5-1}$$

Some of the released In diffused to the surface where it oxidizes to form In_2O_3 and a complex In-P oxide (possibly $In_4(P_2O_7)_3$), which indicates some loss of P as well.

Additional samples were annealed at longer times (up to 2 hrs), with little change in XRD patterns, other than differences in peak intensities. Thus, at first glance, it might appear that the results at 500°C are contradictory to those of Mohney and Chang [42], who have determined isothermal sections of the Ni-In-P phase diagram. According to their results, Ni_2InP is stable to 526°C in a closed system. The presence of oxygen in our sealed tubes and susbsequent formation of In-oxides may drive the decomposition of Ni_2InP at lower temperatures. Above 526°C, however, Ni_2P, InP and In should be in equilibrium with one another in a closed system (according to Mohney and Chang [42]), which appears to be the case here, other than the oxidation of In.

The reactions which take place during annealing are summarized schematically in Fig. 5-9. The overiding result is the laterally non-uniform morphology of the crystallized phases. Similar behaviour has been reported by Appelbaum *et al.* [40] in their studies of Ni(100 nm)/InP interactions (in He). At 250°C (30-60 min), Auger results indicated an intermixed region of Ni, In and P. No phases, other than Ni and InP, were detected by XRD. The intermixed region was likely the same as our amorphous phase (and the phase reported by Sands *et al.* [19] - annealed in forming gas), which would explain why it was not detected by XRD. Appelbaum *et al.* [40] also report "phase separation" for annealing at times longer than 60 min at 250°C or at 300°C. Auger results indicate a Ni-P rich region and a Ni-In rich mixture with some P in the outer layer. Because of the nature of Auger analysis, Appelbaum *et al.* were unable to conclusively identify the phases. It is likely that the Ni-P rich region is the same as our Ni_2P and the Ni-In rich region may have been Ni_2InP. The low P levels in the Ni-In rich region may be attributable to differential sputtering effects during Auger depth profiling. In addition, it should be pointed out that several Ni_2InP regions studied in our work (from samples annealed at 250-400°C) had relatively high In levels compared to P. Electron diffraction patterns from these higher In regions indicated a structure corresponding to Ni_2InP; none of the patterns could be indexed to any Ni-In phases.

Many of our results are also very similar to those reported by Sands *et al.* [19], as has already been discussed. Sands also found regions of Ni_2InP with higher In levels, which was attributed to loss of P by sublimation. The major difference between our work and Sands' work is the absence of a hexagonal ternary phase ($Ni_{2-3}InP$), which formed prior to Ni_2InP (monoclinic) formation in their work.

There are many similarities between the Ni/InP and Pd/InP systems [44,45]. In both near noble metal systems, a metal-rich amorphous phase forms during deposition and grows during early stages of annealing. This is followed by crystallization of the amorphous phase - Pd_2InP in the Pd/InP system and Ni_2InP in the Ni/InP system.

Annealing at higher temperatures (500°C for Ni/InP and 450°C for Pd/InP) results in decomposition of the ternary phases. A major difference in the two systems is that in the Pd/InP system, the crystallization process is much more uniform, i.e., PdInP particles nucleate across the entire amorphous layer/InP interface producing a uniform ternary layer. This is contrasted with Ni/InP, where crystallization is laterally non-uniform resulting in patches of Ni_2InP, Ni_2P and In_2O_3 and mixed $Ni_2InP/Ni_2P/In_2O_3$ regions.

b. *Crystal structure determination of Ni_2InP*

(i) Lattice structure of Ni_2InP

The structure of Ni_2InP was studied in more detail in samples annealed at 400°C for 8 or 15 min. Examination of the zero order Laue zone (ZOLZ) and the higher order Laue zones (HOLZ) for CBED patterns revealed information with respect to the crystal symmetry and structure. The monoclinic structure proposed by Sands *et al.* [19] was initially assumed. Only the lattice parameters were provided by Sands, i.e., a= 0.681 nm, b= 0.529 nm, c= 1.280 nm and β= 95°. From the lattice parameters, the unit cell volume can be calculated, giving a value of 0.459 nm^3. The primitive cell unit volume can be calculated from CBED patterns, using information from both the ZOLZ and HOLZ [46]. A consistent volume of 0.220-0.225 nm^3 was determined from 7 of 9 orientations (two were closer to 0.200 nm^3), which is about one-half the value obtained from the proposed lattice parameters. (The variation in cell volume may be a consequence of composition variability.) If Sands' proposed lattice parameters are correct then the unit cell would have to be non-primitive, i.e., base-centred monoclinic with two lattice points per unit cell, which would account for the difference in cell volumes. On the other hand, Sands' parameters may not be correct. For example, if the c parameter is equal to one-half the proposed value (c= 0.64 nm), the volume of the unit cell would then correspond to that calculated from the CBED patterns and the structure would be primitive. If Sands' structure is assumed to be correct, then there should be systematic absences in the diffraction patterns (for example, the 100 reflection is not allowed in Figure 5-10), unless the structure is ordered, which is indeed a possibility. If, however, c= 0.64 nm, and not 1.28 nm, then the 100 reflection in Figure 5-10 would be allowed. At this point we cannot conclusively rule out either possibility. However, of the 9 orientations studied, all matched with the c= 0.64 nm structure, while all but two matched with the c= 1.28 nm structure. XRD patterns from Ni_2InP samples had abnormally strong peaks for d spacings corresponding to 002, 004 and 006 reflections for Sands' structure (c= 1.28 nm) or 001, 003 and 005 reflections for the c= 0.64 nm structure. According to electron diffraction results, however, the odd reflections (001, 003, 005, etc.) should be observed for Sands' structure (assuming that it is base centred and ordered), but are not, providing further evidence that the c parameter may be 0.64 nm and not 1.28 nm.

By superimposing the higher order Laue zone (HOLZ) reflections onto the ZOLZ reflections in a [001] type zone axis pattern, the structure can be determined as either primitive or nonprimitive. If the reflections line up in both the [100] and [010] directions then the unit cell is primitive. (The observed [100] direction in a [001] zone axis pattern for a monoclinic structure is, in fact, a projection of the [100] direction onto the reciprocal lattice plane imaged, so that the inverse of the magnitude of the reciprocal lattice vector in the observed [100] direction is slightly less than the a lattice parameter.) The [001] pattern in Figure 5-11 clearly shows that the spots line up in both the [100] and [010] directions, indicating that the unit cell is primitive. The magnitude of the reciprocal lattice vector (H) in the [001] direction can be calculated from the pattern in Figure 5-10. The inverse of H (H^{-1}) gives the c lattice parameter. H^{-1} values were calculated from several [001] patterns, giving c= 0.64nm ±0.02nm.

Close examination of [001] patterns also indicates that the angle β is slightly larger than 90° (confirming the monoclinic structure initially reported by Sands *et al* [19]). If, as stated above, the beam direction is parallel to the [001] direction, the HOLZ and ZOLZ reflections should line up in both the [100] and [010] directions. If the crystal is tilted slightly, so that the beam direction is not quite parallel to the [001] direction, but is, instead, perpendicular to the ZOLZ containing the [100] and [010] directions, the HOLZ and ZOLZ spots will be misaligned slightly along the [010] direction. The value of β can be measured approximately from this shift. This effect is shown schematically in Figure 5-12 and in two partial CBED patterns in Figure 5-13. The ZOLZ and FOLZ spots line up along the [010] direction in Figure 5-13a, indicating that the beam direction does correspond to the zone axis. The FOLZ and ZOLZ spots are shifted slightly (a few degrees) along the [010] direction in Figure 5-13b, which indicates that the beam direction is not exactly parallel to the [001] zone axis, but is perpendicular to the ZOLZ containing both the [100] and [010] directions.

The angle β can only be measured approximately from the pattern in Figure 5-13. A more accurate analysis is outlined below and in Figure 5-14. The magnitude of three coplanar reciprocal lattice vectors, which are perpendicular to the [010] direction, are measured. The vectors are drawn in real space so that they form a triangle, with the lengths of the sides equal to an appropriate integer multiple of the reciprocal of the magnitudes of the three vectors (Figure 5-14). If the lengths of the three sides are known, then any of the angles can be calculated from the following equation:

$$\cos \beta = (x^2 + y^2 - z^2) / 2xy \qquad (5\text{-}2)$$

The directions chosen for the calculation are shown in Figure 5-14, giving a value of β equal to 94 ± 0.3°

(ii) Point group determination

Point group determination was done based on the analysis given by Buxton *et al* [49]. The relationship between observed symmetries in CBED patterns and the 31 diffraction groups, which correspond to the 32 three dimensional point groups, is shown in Table 5-3.

Information concerning the symmetry of Ni_2InP can be obtained by examining the CBED patterns in more detail, in particular the HOLZ lines (Figure 5-15). In every pattern examined, a plane of symmetry or mirror plane was found perpendicular to the b direction.

Figure 5-15 shows a zone axis CBED ([103] if a monoclinic structure is assumed - this is based on previous work done by Sands *et al* [19]). The zero order Laue zone (ZOLZ) symmetry (Figure 5-15b) is 2mm, which gives a projection diffraction group of $2mm1_R$ (Table 5-3 - appropriate symmetry information is highlighted), and therefore, possible diffraction groups of $2m_Rm_R$, 2mm, 2_Rmm_R and $2mm1_R$. The whole pattern (Figure 5-11a) and zero order disc symmetries (Figure 5-15c) are both m, which means that the diffraction group must be 2_Rmm_R.

In order to ascertain the point group, another zone axis was chosen (Figure 5-16 - $[1\bar{3}\bar{5}]$ for the assumed monoclinic structure). The ZOLZ symmetry is 2, giving a projection diffraction group of 21_R and 3 possible diffraction groups - 2, 2_R and 21_R. The whole pattern symmetry is 1, so that the diffraction group must be 2_R.

The point group is determined using Table 5-4 [47], which shows the relationship between diffraction groups and crystal point groups. Several point groups (nine) correspond to both diffraction groups, 2_Rmm_R and 2_R. However, seven of these can be eliminated from consideration, as they represent crystals that possess 4-fold, 3-fold or 6-fold symmetry. The point group, mmm, can also be discounted as it requires 3 orthogonal axes. If a monoclinic crystal structure is assumed, then the point group must be 2/m.

(iii) Space group determination

The final step in the process is to determine the space group. A given point group type and crystal structure can correspond to several possible space groups. It is necessary to analyze the reflections that are kinematically forbidden for each space group in order to identify the appropriate one. Due to the dynamical nature of electrons, reflections that are forbidden kinematically often occur in CBED patterns due to double diffraction. This is either due to crystal centering or to additional symmetry elements, such as glide planes or screw axes. When two or more equivalent double diffraction paths exist in a given orientation, the kinematically forbidden reflections that occur will have a central line of zero intensity (Gjϕnnes-Moodie or G-M line) passing through the disc. The reflections, forbidden by kinematical theory, which generally have a multiple double diffraction route, usually appear on a principal line of a zone axis pattern indicating that the electron beam is incident on the crystal either parallel to a glide plane or perpendicular to a screw axis [50]. Table 5-5, established by Steeds and Vincent [51], describes the relationship between the dynamical absences and the number of symmetry elements that can be responsible for those dynamical absences. In order to determine whether one or both glide plane and screw axis symmetry elements are present, the orientation of the G-M line with respect to the bright-field mirrors within the zone axis must be analyzed. Figure 5-17 shows a [001] ZOLZ CBED pattern, with spots indexed as 010 and 100. It possesses the characteristics of alternate forbidden reflections along the [010] direction and characteristic lines of absence alternately appearing in these reflections along this direction (indicated by arrows in Figure 5-17). A mirror plane occurs along [100] or perpendicular to [010]. According to Table 5-5, the symmetry element is a screw axis perpendicular to the mirror plane. The space group is then $P2_1/m$, as determined from Ref. [52].

5-2-2 Conclusions

The conclusions based on the experimental results for the Ni/InP system can be described as:

1. An amorphous ternary phase, approximate composition corresponding to Ni_3InP, forms during Ni deposition at the Ni/InP interface. The amorphous phase grows during low temperature annealing, consuming the entire Ni layer by 250°C.
2. Crystallization of the amorphous phase begins at 250°C at the amorphous phase/InP interface and the process is laterally non-uniform. The two major phases formed are Ni_2InP and Ni_2P. Ni_2InP grows with a preferred orientation to the InP substrate, i.e., $[001]_{Ni2InP} // [001]_{InP}$. Oxidation of In also occurs.
3. Annealing at 500°C results in decomposition of Ni_2InP, forming Ni_2P and In. Oxidation of In also takes place.
4. The point group of Ni_2InP was determined as 2/m by analyzing the symmetry of zone axis CBED patterns.
5. The unit cell of Ni_2InP was confirmed to be primitive monoclinic with lattice parameters of a= 0.681 nm, b= 0.539 nm, c= 0.64 ± 0.02nm and $\beta = 94 \pm 0.3^{o}$.

6 The space group of Ni_2InP is identified as $P2_1/m$, by analyzing the dynamic absences along a systematic line of reflections.

5-3 Ge/Ni Metallizations to n-type InP

5-3-1 Experimental results and discussion

a. Interfacial structure of as deposited specimen

Interfacial reaction characterization was carried out starting with the as deposited specimens - 4 layers are visible in Figure 5-18. EDX analysis (Figures 5-19a, b, c, d) and SAD analysis of individual layers indicate that the outer layer is amorphous Ge, (Figures 5-20 a and b). The layer next to it is a Ge-Ni mixed layer (Figures 5-21a and b), followed by a layer of Ni with a very fine grain size (~10nm) (Figures 5-22a and b). The inner most layer is an amorphous ternary phase containing Ni, In and P. The thicknesses of these layers were measured to be 50nm for the Ge layer, 16nm for the Ge-Ni layer, 13nm for the Ni layer and 16nm for the amorphous ternary phase (Figure 5-18). The nominal thickness for the deposited metallization was 52.5nm of Ge and 25nm of Ni. The differences arise because of reaction between the layers during deposition and sample preparation.

b. Reactions between Ge and Ni

The first sign of reaction between Ge and Ni metallizations seems to appear in the as deposited samples. A thin Ge-Ni mixed layer exists at the interface between the Ge and Ni layers (see the image of a cross section specmen shown in Figure 5-18). However, plan view images (Figure 5-21) and corresponding diffraction patterns do not show any evidence of Ni/Ge interaction. Only polycrystalline Ni and amorphous Ge (the ring pattern corresponds to Ni, the blurred ring corresponds to amorphous Ge) were identified. The reacted layer in the cross section specimens is likely a result of heating during epoxy curing during specimen preparation.

Significant differences can be seen from the micrograph of a cross section specimen (Figure 5-23) annealed at 250°C for 60s. The thickness of the Ge layer is approximately 20 nm, which is less than the original thickness and indicates that part of the Ge participated in reactions with Ni. The remaining Ge retained its amorphous structure. The thickness of the Ge-Ni layer (in fact, it is two layers) increases from ≈16 nm to ≈50 nm. GeNi (orthorhombic, a= 0.5811 nm, b= 0.5381 nm, c= 0.3428 nm) (Figure 5-24a, b), with irregularly shaped grains ranging from 30 to 45nm in size, and $Ge_{12}Ni_{19}$ (hexagonal, a=0.672nm. c=1.005nm) (Figure 5-25a, b) with a grain size of ~20nm, have formed at the

Ge/Ni interface. $Ge_{12}Ni_{19}$ is not a stable phase at room temperature, but it did form in this case. $Ge_{12}Ni_{19}$ forms from the remaining Ni in contact with the amorphous layer. Since Ni is in contact with a metastable phase, it is possible to form a metastable phase ($Ge_{12}Ni_{19}$).

Annealing at 250 °C for >120 s resulted in more Ge reaction with Ni to form GeNi and the transformation of $Ge_{12}Ni_{19}$ to GeNi. The interfacial structure consists of amorphous Ge, GeNi and the decomposed ternary layer (Ni-In-P) on InP (Figure 5-26). The changes to the amorphous layer, which are shown in Figure 5-26 and 5-27, will be discussed in the next section.

Essentially all the Ge is consumed (a small amount of excess Ge remains) by 250°C and 480s (Figure 5-27b), or at higher temperatures (350°C) and shorter times (60s) (Figure 5-28), to form GeNi. Basically, a single, fairly uniform layer of GeNi covers the InP substrate.

c. Formation and growth of the amorphous ternary phase

In the previous section, it was shown that a ternary amorphous phase ($Ni_{\approx 3}InP$) formed at the interface between Ni and InP in the Ni/InP system. A similar amorphous phase formed at the Ni/InP interface for the Ge/Ni metallization. The initial formation of the amorphous ternary phase is likely a result of two effects, one being the interdiffusion that occurs between the deposited metallization and substrate atoms during deposition - sample heating to ≈100°C occurs. The other factor is heating during specimen preparation, when specimens are subjected to temperatures ranging from ~80 to 100°C for 1 hour. This is likely the primary cause of initial amorphous phase formation, as there is no visible amorphous ternary phase at the InP interface in the as deposited plan view specimens.

The thickness of the amorphous ternary layer increases with increasing temperature. It reaches 30nm when heated at a temperature as low as 160°C for 2 min (Figure 5-29). About 10nm of Ni was consumed to participate in both the Ge-Ni reactions and ternary amorphous phase growth from 16 nm to 30 nm (measured from the as deposited image shown in Figure 5-18 and the image of the specimen annealed at 160°C for 2 min shown in Figure 5-29). The remaining 3nm of Ni was aconsumed during further growth of the aporphous layer as well as in the formation of Ge-Ni compounds. The ternary layer remained amorphous up to 250°C (60s), and became thicker (~35nm) (see Figure 5-23).

The composition of the amorphous phase, as determined by EDX analysis, was found to be variable, i.e. $Ni_{2-3}InP$, which is in agreement with previous work [16,49] and is similar in composition to the amorphous layer that formed in the Ni/InP metallizations.

d. Decomposition of the amorphous ternary phase

Decomposition of the amorphous ternary phase occurred after annealing at temperatures >250°C. Unlike the Ni/InP system there was no transformation to a crystalline ternary phase of similar composition. Instead, a new phase consisting of primarily Ni, P and Ge formed. The phase formation will be discussed below.

(i) Nucleation

Annealing at 250°C for 90s resulted in the nucleation of a new phase from the amorphous phase. Crystallization started with the formation of nucleation sites, one of which is shown in the plan view image in Figure 5-30a. The site areal density is of the order of $\approx 2.5 \times 10^3/\mathrm{mm}^2$ (Figure 5-30b). At each nucleation site a mixed microstructure is apparent (Figure 5-30c). Some grains appear to be textured, while others are equiaxed (Figure 5-31). Randomly oriented nuclei form, with preferentially oriented grains growing at the expense of the others. Preferred growth occurs laterally through the amorphous layer.

There are three possible nucleation locations: the interface between the amorphous layer and the Ge-Ni layer, the interface between the amorphous layer and InP and within the amorphous layer. No direct experimental evidence has been found to confirm or rule out any of these possibilities. However, the subsequent preferred growth with respect to InP (discussed below) suggests that nucleation occurred primarily at the amorphous layer/InP interface. For comparison, in the Ni/InP metallization, Ni_2InP nucleation occurred at the amorphous layer/InP interface, although this was the only heterogeneous nucleation site available.

(ii) Preferred growth

The phase that formed during the decomposition of the amorphous phase was found to have a Ni_2P-type hexagonal structure (a= 0.607 nm and c= 0.337 nm) and contained significant amounts of Ge in addition to Ni and P. The phase is hereafter referred to as $Ni_2P(Ge)$, which implies that Ge is in solid solution. The orientation relationshop between InP and the textured $Ni_2P(Ge)$ was found to be $[2\bar{1}\bar{1}3]_{Ni2P(Ge)}$ $//[100]_{InP}$. A lateral growth direction was along $<0\bar{1}10>$ direction in $Ni_2P(Ge)$. This is apparent in Figure 5-32, which shows 2 diffraction patterns taken from a $Ni_2P(Ge)$ crystal by tilting the crystal about an axis parallel to its gowth direction. The growth direction is determined from the cross multiple of the two zone axes.

Complete crystallization of the amorphous ternary phase was found in specimens annealed for longer times, i.e., 120s at 250°C. The textured structure of the crystallized product remained (Figure 5-33a). EDX analysis of plan view specimens shows that the textured phase contains Ni, P and Ge (Figure 5-33b), and almost no In. However, EDX analysis of cross section specimens yields significant amounts of In, which implies that crystallization of the amorphous ternary phase resulted in the release of In, which likely segregated to the interface or grain boundaries. Indium was also detected on the surface of the contact, which suggests that In out diffusion has occurred. It should be emphasized that Ge inward diffusion played an important role in preventing In from dissolving in $Ni_2P(Ge)$, as Ge has a higher affinity for Ni than for In (evident in the Ge-In and Ge-Ni phase diagrams in Figure 5-34). A reasonable assumption is that Ge diffuses into the amorphous layer and replaces In to form $Ni_2P(Ge)$ nuclei. It seems likely that Ge substitutes for P in $Ni_2P(Ge)$. At higher annealing temperatures, $Ni_2P(Ge)$ transform to GeNi (which is stable to ≈450°C). If Ge substitutes for Ni in Ni_2P, then one would expect a Ge-P compound(s) to form as an intermediate step or as a final phase. However, no Ge-P phases were detected.

The proposed decomposition reaction isgiven below. For simplicity, the amorphous layer, which has a variable composition ($Ni_{2\text{-}3}InP$), is assumed to have a composition corresponding to Ni_2InP.

$$Ni_{2\text{-}3}InP_{\,amor} + x\,Ge \rightarrow Ni_2(P_{1\text{-}x},Ge_x)_{\,hex} + \;x\,InP_{regrown} + (1\text{-}x)\,In \qquad (5\text{-}3)$$

where $0 \le x \le 1$. The term $InP_{regrown}$ refers to InP regrowth on the substrate during $Ni_2P(Ge)$ formation, which will be discussed in later paragraphs. As mentioned previously, In was detected in the $Ni_2(P_{1\text{-}x},Ge_x)$ (or $Ni_2P(Ge)$) layer in cross section specimens, but not in plan view specimens. If In was present at the grain boundaries, it may have been etched away during plan view specimen preparation.

$Ni_2(P_{1\text{-}x},Ge_x)$ is not thermally stable. Further Ge diffusion to the layer results in the formation of GeNi. A single layer of GeNi was found in samples annealed at 250°C for 480 s or 300°C for 60s. The reaction can be written as

$$Ni_2(P_{1\text{-}x},Ge_x) + (2\text{-}x)\,Ge \;+ (1\text{-}x)\,In = 2\,GeNi_{orth} + (1\text{-}x)\,InP_{regrown} \qquad (5\text{-}4)$$

where $0 \le x \le 1$.

(iii) Epitaxial growth of InP

InP epitaxial regrowth during amorphous layer crystallization/decomposition is proposed. It can be divided into two stages. It occurs initially during $Ni_2(P_{1\text{-}x},Ge_x)$

formation and later during $Ni_2(P_{1-x},Ge_x)$ decomposition (reaction with Ge to form GeNi). Experimental evidence for InP regrowth is shown in Figures 5-27 and 5-28. During annealing at 250°C from 120s to 480s, $Ni_2(P_{1-x},Ge_x)$ disappears and is replaced by InP. Regrowth of GaAs has been reported in similar metallizations to GaAs (Pd/Ge to n-type GaAs) and also proposed for other metallizations to InP [53,54].

e. Contact structure after higher temperature annealing

In samples annealed at 350^0C for 60s (Figure 5-28), a single layer of GeNi formed adjacent to InP and a thin In-rich layer (~10nm) was present on the surface of the films. A micrograph of a plan view specimen shows fairly uniform grains of GeNi (~50nm) (Figure 5-35). The thickness of GeNi layer is 60-62nm and the InP surface is fairly smooth. The nominal deposited amounts of Ge and Ni were 52.5nm and 25nm respectively, which correspounds to an atom ratio of Ge/Ni slightly greater than 1. To form 60-62nm of GeNi, 24.5-25.3nm of Ni and 49.68-52.37nm of Ge are needed, which implies that some excess Ge is available for inward diffusion to the InP, for doping purposes. The regrown InP is the most likely candidate for significant doping.

After annealing at higher temperatures (450°C for 60s), a porous and thick layer containing mainly In as well as P and Ge was found on the surface of the films. In addition, the GeNi/InP interface had become quite rough (Figure 5-36a). This is a sign of further decomposition, releasing In and P, both of which diffused through the GeNi layer to the surface (Figure 5-36a, b). InP decomposition would be expected to have an adverse effect on electrical properties, as the heavily doped regions would decompose first.

The overall reactions for the Ge/Ni/InP system are shown schematically in Figure 5-37.

5-3-2 Conclusions

1. An amorphous ternary phase formed and grew at the Ni/InP interface, by consuming Ni and InP, during low temperature annealing (<250°C).
2. Crystallization of the amorphous phase started at about 250°C, resulting in the formation of a Ni_2P-type compound, which decomposed at higher temperatures or longer annealing times.
3. Reactions between Ge and Ni began at temperatures <160°C, ultimately forming a continuous layer of GeNi (250°C for 480 s).
5. Annealing at 350°C resulted in the formation of a fairly uniform layer of GeNi, but with a thin layer of In oxide on the surface of the contacts.

6. Higher temperature annealing (>400°C) resulted in further InP decomposition and roughening of the InP surface.

5-4 Relationship between electrical properties and microstructure

5-4-1 Electrical properties

Problems were encountered in obtaining reliable electrical measurements. The initial set of samples processed for TLM measurements gave widely varying results, which were non-ohmic in many cases. For these samples, the interconnect layers (Ti/Pt/Au) were deposited after contact annealing. It is believed that the oxidation of Ge, as well as In and P, that occurred during annealing was responsible for the unreliable results - the oxides are poor conductors. A second set of TLM samples was fabricated. In this case, the interconnect layers (Ti/Pt/Au) were deposited immediately after Ge/Ni deposition and prior to any annealing. The interconnect layers were able to act a capping layer to prevent oxidation of the metallization. It is likely that the interconnect layers were inert relative to the contact metallization, at least at the temperatures studied (≤450°C). Further microstructural analysis is needed, but is unavailable at this time, to confirm this hypothesis.

Only limited electrical measurements were attainable at this time - these are shown in Table 5-6. Ohmic behaviourand relatively low specific contact resistances (low 10^{-6} Ω-cm^2 range) were obtained for all samples measured.

5-4-2 Ohmic behaviourand contact microstructure

It is difficult, if not impossible, to draw any meaningful corelations between the limited electrical results and the contact microstructure. Nevertheless, a couple of points can be made. The contact resistance was fairly low and consistent for the 3 measurements at 300°C and 350°C, while there was an increase at 450°C. The contact structure at 300-350°C consisted of a laterally uniform GeNi layer on InP, which was microstructurally the most desirable structure. At 450°C, the metallization/semiconductor interface had become quite irregular and significant outward In and P diffusion - a sign of InP decomposition - was detected.

References

1. J.A. Del Alamo and T. Mizutani, *Solid-State Electr.* Vol. 31, 1635 (1988).
2. K.P. Pande, E. Martin, D. Gutierrez and O. Aian, *Solid State Electr.*, Vol. 30, 253 (1987).
3. L.P. Erickson, A. Waseem and G.Y. Rovinson, *Thin Solid Films,* Vol. 64, 421 (1979).
4. N.S. Fatemi and V.G. Weizer, *Mat. Res. Soc. Symp. Proc.* Vol. 260, 537 (1992).
5. D.A. Anderson, R.J. Graham and J.W. Sttds, *Semicond. Sci. Technol.* Vol. 3, 63 (1988)
6. R.J. Graham, S. Myhajlenko and J.W. Steeds, *J.Appl. Phys.* Vol. 57,1311 (1985).
7. A. Piotrowska, E. Kaminska, A. Barcz, J. Adamczewska and A.Turos, *Thin Solid Films,* Vol. 130, 231 (1985).
8. M.F.J. O'keefe, R.E. Miles and M.J. Howes, *Indium Phosphide and Related Mater. for Adv. Electr. Optical Devices*, Vol. 1144, 361 (1989).
9. G. Bahir, J.L. Merz, J. R. Abelson and T.W. Sigmon, *J.Electr. Mater.* Vol. 16, 257 (1987)
10. H. Morkoc, T.J. Drummond and C.M. Stanchak, *IEEE Trans. Electr. Devices* Vol. ED-28, 1 (1981).
11. D.G. Ivey, D. Wang and D. Yang, *Microscopical Soc. Can. 20thy ann. Meet*, 3-5 June 1993, Toronto, Ont.
12. D.G. Ivey, D. Wang, D. Yang. R. Bruce and G. Knight, *J. Electr. Mater.* Vol. 23, 441 (1994).
13. A. Appelbaum, M. Robbins and F. Schrey, *IEEE Ttrans. Electr. Devices* , Vol. ED-34, 1026 (1987).
14. E. Kuphal, *Solid State electron*, Vol. 24, 69 (1981).
15. V.L. Rideout, *Solid state Electron.* Vol. 18, 541 (1975).
16. A. Appelbaum, P.M. Thomas and P. A. Baarnes, in *Semiconductor-based heterosturctures: Interfacal structure and Stability*, M.L. Green, E.E. Baglin, G.Y. Chin, H.W. Deckman, W. Mayo and D. Narasinham Eds, The Metallurgical Society, Inc. 409, (1986).
17. J. Dunnand G. Stringfellow, *J. Electronic Materials*, Vol. 19, No.2, 1990.
18. N.S. Fatemi and V.G. Weizer, *J Appl. Phys.* Vol. 73, 289(1993).
19. T. Sands, C.C. Chang, A.S. Kaplan, V.G. Keraqmidas, K.M. Krishnan and J. Washburm, *Appl. Phys. Lett.* Vol. 50, 1346 (1987).
20. G. Stremsdierfer, Y. Wang, J.R. Martin and E.Souteyrand, *Mat,Res. Soc.Symp Proc.*, Vol.260, 543 (1992).
21. S.E. Mohney and Y.A. Chang, *Mat. Res. Soc.Symp. Proc.* Vol. 337. 393-398 (1994).
22. S.E. Mohney and Y.A. Chang, *J. Mater. Res.* Vol.7, 955 (1992).
23. V.G. Weizer, N.S. Fatemi, and A.L. Korenyi-both, *Proc. Fourth International Conf.* on *Indium Phosphide and Related materials*, Newport, RI, (1992).
24. M. Ogawa, *J. Appl., Phys.*, Vol. 51, 406, (1980).
25. T.S. Kuan, P.E. Batson, T.N. Jackson, H. Rupprecht and E.L. Wilkie, *J. Appl. Phys.*, Vol. 54, 6952, (1983).
26. Z. Liliental and R.W. Carpenter and K. Eacher, *Ultramicroscopy*, Vol. 14, 135, (1984).
27. Y.C. Shih, M. Murakami, E.L. Wilkie and A.C. Callegari, *J. Appl. Phys*, Vol.62, 582 (1987).
28. R.A. Bruce and G.R. Piercy, *Solid-State Electron.*,Vol 30, 729, (1987).
29. J.B.B. Oliveira, C.A. Olivieri and J.C. Galzerani, *Vacuum*, Vol.41, 807, (1990).
30. S.J. Chua, S.H. Lee, R. Gopalakrishnan, K.L. Tan and T.C. Chong, *Thin solid Films*, Vol. 200, 211, (1991).
31. T. Sands, *J. Metals*, 38:31 (1986).
32. S.A. Chambers and V.A. Loebs, *J.Vac. Sci. Technol.*, Vol. A10:1940 (1992).

33. H.M. Harris and J.R. Farley, *Mat. Res. Soc. Symp. Pro.*, Vol. 260. 475, (1992).
34. M. Murakami, A. Otsuki, K. Tanahashi and H.K. Takata, *Mat. Res. Soc. Symp. Proc.*, Vol. 260, 457, (1992).
35. J. Dunn and G. Stringfellow, *J.Electronic Materials*, Vol. 19, No.2, 1990.
36. C.J. Cooke and W. Hume-Rothery, *J. Less-Common Met.*, Vol. 10, 42 (1966).
37. D.Coullman, N. Newman, G.A. Reid, Z. Liliental-Weber, E.R. Weber and W.E. Spicer, J. Vac. Sci. Technol. Vol. A 5,1521 (1987).
38. T.S. Kuan, P.E. Batson, T.N. Jackson, H. Rupprecht, and E.L. Wilkie, *J. Appl. Phys*. Vol. 54, 6952 (1983).
39. N.S. FATEMI and V.G. WEIZER, *Mater. Res. Soc. Symp. Proc.*, Vol. 260, 537 (1992).
40. A. Appelbaum, P. M. Thomas and P. A. Barnes, "Interaction of Nickel with InP as a Function of Annealing Time and Temperature", *Semiconductor-based Heterostructures: Interfacial Structure and Stability,* ed. M. L. Green, E. E. Baglin, G. Y. Chin, H. W. Deckman, W. Mayo and D. Narasinham (Warrendale, PA: The Metallurgical Society. 1986), 409-417.
41. G. Stremsdoerfer *et al.*, "Refractory Ohmic Contacts Formed by Electroless Deposition of Palladium and Nickel Onto N-InP", *Mat. Res. Soc. Symp. Proc.*, 260, 543-548 (1992).
42. S. E. Mohney and Y. A. Chang, "Phase Equilibria and Ternary Phase Formation in the In-Ni-P System, *J. Mater. Res.*, Vol. 7, 995-960 (1992).
43. A. Appelbaum, M. Robbins and F. Schrey, "Sputtered Ni-P as an Ohmic Contact to n-InP, p-InGaAs and as a Diffusion Barrier", *IEEE Transactions of Electron Devices,* ED-34,1026-1031 (1987).
44. R. C. Popowich *et al.*, "Phase Formation in the Pd-InP System", *J. Appl. Phys.*, Vol. 64, 4909-4913 (1988), .
45. D.G. Ivey *et al.*, "Reactions Between Pd Thin Films and InP", *J. Electron. Mater.*, Vol. 21, 831-839 (1992).
46. Y. Lepage and D.A. Downham, "Primitive Unit Cell Volumes Obtained from Unindexed CBED Patterns", *J. Electron Micros. Tech.*, Vol. 18, 437 (1991).
47. M.H. Loretto, *Electron Beam Analysis of Materials* London, UK: Chapman and Hall, Ltd., 1984), 79-100.
48. D.G. Ivey and D. Wang, "Low Temperature Reactions Between Nickel Thin Films and InP", presented at TMS Fall Meeting, Pittsburgh, PA, October 17-21, 1993.
49. B.F. Buxton, J.A. Eades, J.W. Steeds and G.M. Racjham, *Phil. Trans. Roy. Soc.*, Vol. 281, 171 (1976).
50. J. Gjϕnnes and A.P. Moodie,*Acta Cryst.*, Vol. 19, 65 (1965).
51. J.W. Steeds and R.J. Vincent,*J. Appl. Cryst.*, Vol. 16, 317 (1983).
52. T. Hahn, editor, "International Tables for Crystallography: Volume A, Space Group Symmetry" (D. Reidel Publishing Co., Dordrecht, Holland, 1983) No. 13, pp. 166-167.
53. T. Sands, E.D. Marshall and L.C. Wang, J. Mater. Res. Vol. 3(5), Sep/Oct, 914-921(1988).
54. D.G. Ivey, P. Jian, L. Wan, R. Bruce, S. Eicher, C. Blaauw, J. Electron. Mater., Vol.20, 237 (1991).
55. D.G. Ivey, D. Wang, D. Yang, R. Bruce and G. Knight, *J. Electr. Mater*. Vol. 23, 441 (1994).

Table 5-1 AuGeNi contacts to GaAs

Metallization	Doping level (cm^{-3})	Resistance r_c (Ω-cm^2)	Processing condition	Reference
50 nm Au/20 nm Ni/100 nm (Au-Ge)	2 x 10^{17}	9 x 10^{-7}	410 °C, 115 s	25
200 nm Au/ 20 nm Ni/20 nm Ge	1 x 10^{18}	5.6 x 10^{-6}	330 °C, 100 hrs	28
200 nm Au/20 nm Ni/20 nm (Au-Ge)	1 x 10^{18}	1.6 x 10^{-5}	330 °C, 100 hrs	28
20 nm Ni/100 nm (Au-Ge)	1 x 10^{18}	9.3 x 10^{-6}	330 °C, 100 hrs	28
100 nm AuGeNi/AuNi	7.8 x 10^{17}	1.3 x 10^{-5}	460°C, 3 min	29
	6.6 x 10^{18}	2.7 x 10^{-6}		
600 nm Au/150 nm Ni/40 nm Ge/120 nm Au	8 x 10^{17}	8.6 x 10^{-6}	380°C, 15 min	30

Table 5-2 AuGeNi contacts to InP

Metallization	Doping level (cm^{-3})	Resistance r_c (Ω-cm^2)	Processing condition	Reference
25 nm Ni/125 nm (Au-Ge)	—	8 x 10^{-6}	375 °C, 3min	2
30 nm Ni/150 nm (Au-Ge)	8 x10^{17}	0.02-0.07Ωcm	360 -630 °C, 30 s	1
40 nm Au/15 nm Ni/60 nm (Au-Ge)	2x10^{18}	2 x 10^{-7}	430-450 °C, 2 s	9
100 Au /75 nm Ni/50 nm(Au-Ge)	----	8x10^{-7}	450°C, 25 s	10
70- nm Ni/300 nm (Au-Ge)/40 nm Ni	8 x10^{17}	2.3 x 10^{-6}	400 °C, 2 min	7
70 nm Ni/ 300 nm (Au-Ge)	8 x10^{17}	1.2 x 10^{-6}	350-400°C, 2 min	7
140 nm Ni/40 nm Au/20 nm Ge	1.7x10^{18}	10^{-7}	400 °C, <20 min	3
140 nm Ni/20 nm Ge/40 nm Au	1.7x10^{18}	10^{-8}	400°C, <5 min	18
5 nm Ni/500 nm Au/50 nm Ge	10^{15}	1.5 x 10^{-6}	330-390°C, 15 min	5
40 nm Au/50 nm Ge/25 nm Ni	10^{17}	10^{-7}	400°C, 10 s	11, 12
5 nm Ni/25nm Ge/50 nm Au/40 nm Ni	(5-9)x10^{15}	10^{-4}	450 °C, 1 min	8
Au(40nm)/Ge(50 nm)/Ni(25 nm)	1x10^{17}	8x10^{-5}	325°C	12

Table 5-3 Relationship between observed symmetries in CBED patterns and diffraction groups [47]

Observed symmetry in zero-order zone	Projection diffraction group	Possible diffraction groups	Symmetries of high-order information	
			Whole pattern	Zero-order disc
1	1_R	1	1	1
		1_R	1	2
2	21_R	2	2	2
		2_R	1	1
		21_R	2	2
m	$m1_R$	m_R	1	m
		m	m	m
		$m1_R$	m	2m
2mm	$2mm1_R$	$2m_Rm_R$	2	2mm
		2mm	2mm	2mm
		2_Rmm_R	m	m
		$2mm1_R$	2mm	2mm
4	41_R	4	4	4
		4_R	2	4
		41_R	4	4
4mm	$4mm1_R$	$4m_Rm_R$	4	4mm
		4mm	4mm	4mm
		4_Rmm_R	2mm	4mm
		$4mm1_R$	4mm	4mm
3	31_R	3	3	3
		31_R	3	6
3m	$3m1_R$	$3m_R$	3	3m
		3m	3m	3m
		$3m1_R$	3m	6mm
6	61_R	6	6	6
		6_R	3	3
		61_R	6	6
6mm	$6mm1_R$	$6m_Rm_R$	6	6mm
		6mm	6mm	6mm
		6_Rmm_R	3m	3m
		$6mm1_R$	6mm	6mm

Table 5-4 Relationship between diffraction groups and crystal point groups [47]

Diffraction groups

	1	$\bar{1}$	2	m	2/m	222	mm2	mmm	4	$\bar{4}$	4/m	422	4mm	$\bar{4}2m$	4/mmm	3	$\bar{3}$	32	3m	$\bar{3}m$	6	$\bar{6}$	6/m	622	6mm	$\bar{6}m2$	6/mmm
$6mm1_R$																											X
$3m1_R$																										X	
$6mm$																									X		
$6m_Rm_R$																								X			
61_R																							X				
31_R																						X					
6																					X						
6_Rmm_R																				X							
$3m$																			X								
$3m_R$																		X									
6_R																	X										
3																X											
$4mm1_R$															X												
4_Rmm_R														X													
$4mm$													X														
$4m_Rm_R$												X															
41_R											X																
4_R										X																	
4									X																		
$2mm1_R$								X							X												X
2_Rmm_R					X			X			X				X					X			X				X
$2mm$							X																			X	
$2m_Rm_R$						X						X		X										X			
$m1_R$							X						X	X											X	X	
m				X			X						X	X					X			X			X	X	
m_R			X			X	X		X	X		X	X	X				X			X			X	X	X	
21_R					X															X							
2_R		X			X			X			X				X					X			X				X
2			X															X									
1_R				X															X								
1	X		X	X		X	X		X	X		X	X	X		X		X	X		X	X		X	X	X	

Crystal point groups

Table 5-5 Six different cases of dynamic absences along a single systematic line of reflections [51]

WP	BF	Diffraction group	Orientation of mirrors with respect to line of absences in a zone-axis pattern (orthogonal lines are principal axes)	Minimum number of symmetry elements responsible for absence
1	m	m_R	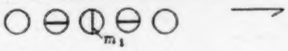	Screw axis perpendicular to beam (2_1, 4_1, 4_3, 6_1, 6_3 or 6_5)
m	m	2_Rmm_R (a) and (b) or	(a) 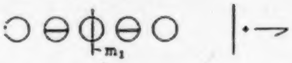	Screw axis perpendicular to the beam and to a mirror plane; $2_1/m$, $6_3/m$
		m (b)	(b) 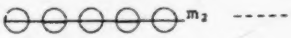	Glide plane parallel to beam
m	2mm	$m1_R$	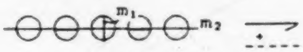	Screw axis (2_1, 6_3) plus parallel glide plane
2mm	2mm	2mm or $2mm1_R$	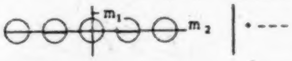	As (b) above with an extra mirror plane parallel to the beam and perpendicular to the glide plane.
2	2mm	$2m_Rm_R$	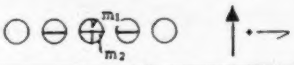	Screw axis (2_1, 4_1, 4_3, 6_1, 6_3 or 6_5) perpendicular to a two-fold axis or 2_1 axis perpendicular to a four-fold axis both perpendicular to the beam.

Table 5-6 Specific contact resistances for Ge/Ni-InP contacts annealed at different temperatures and times.

Annealing condition (°C/s)	300/120	350/60	350/480 *	450/60 *
r_c ($\times10^{-6}$ Ω-cm^2)	3.5 - 5.0	3.2	2.6-4.2	3.3-9.6

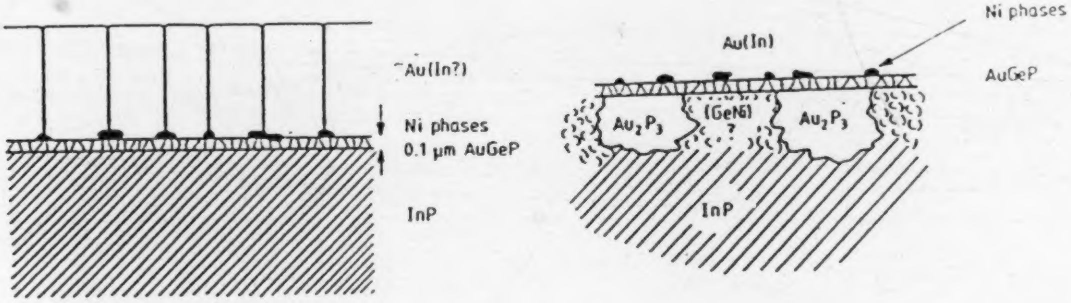
Au(In?)
Ni phases
0.1 µm AuGeP
InP
Ni phases
Au(In)
AuGeP
Au2P3
(GeNi) ?
Au2P3
InP

Fig. 5-1 Schemematic model for the AuGeNi alloyed contact to InP, immediately after alloying (a) and after subsequent heat treatment at elevated temperatures for several hours (b).

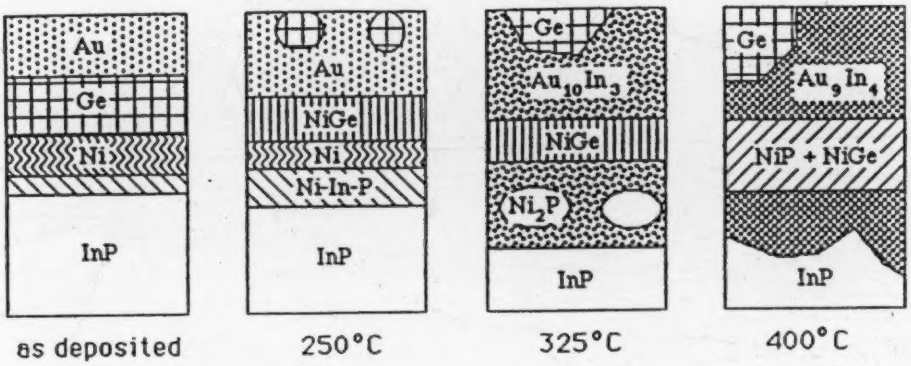
Au
Ge
Ni
InP
as deposited
Au
NiGe
Ni
Ni-In-P
InP
250°C
Ge
Au10In3
NiGe
Ni2P
InP
325°C
Ge
Au9In4
NiP + NiGe
InP
400°C

Fig. 5-2 Schematic representation of reactions that occur in the Au (40 nm)/Ge (50 nm) Ni (25 nm) system during annealing.

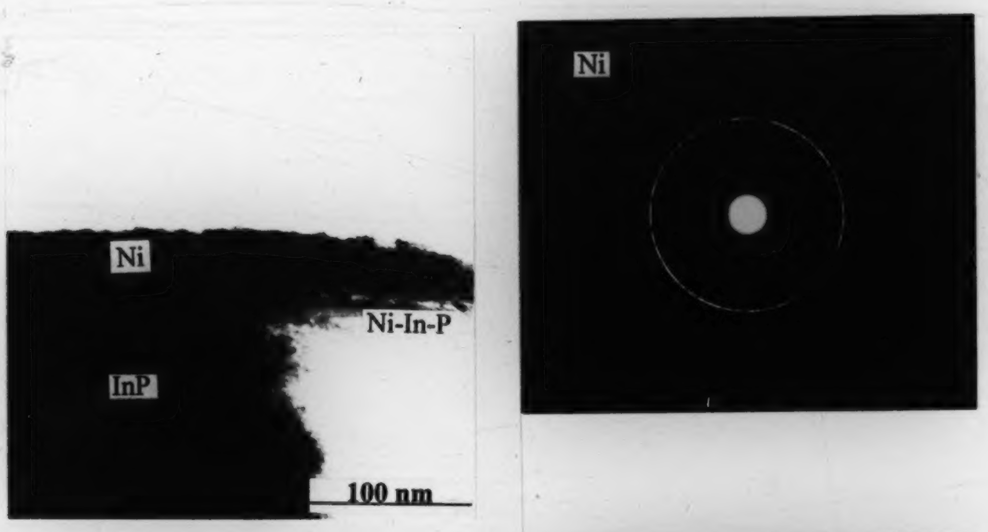

Fig. 5-3 Bright field (BF) micrograph from a cross section specimen of the as deposited sample. Also shown is an SAD pattern from a plan view specimen of the Ni layer.

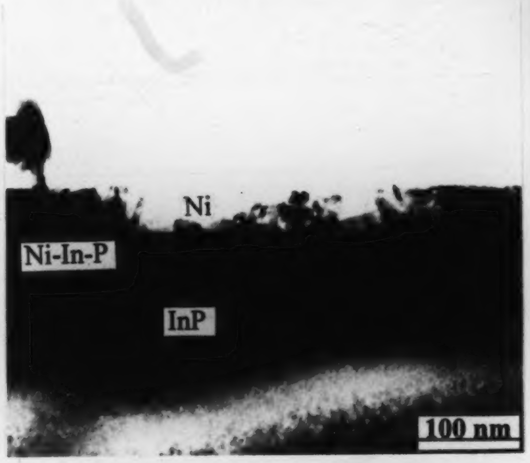

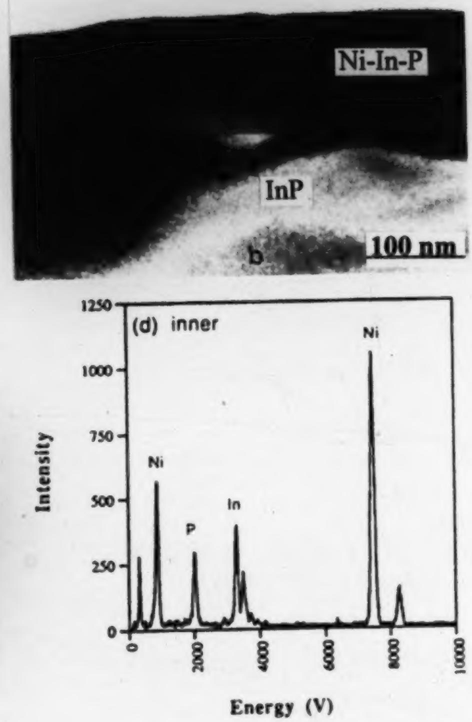

(a) (c)

Fig. 5-4 BF micrographs of cross section specimens (a) annealed at 190°C for 15 min and (b) annealed at 250°C for 30 min. Also shown are EDX spectrum taken from the amorphous ternary layer (c).

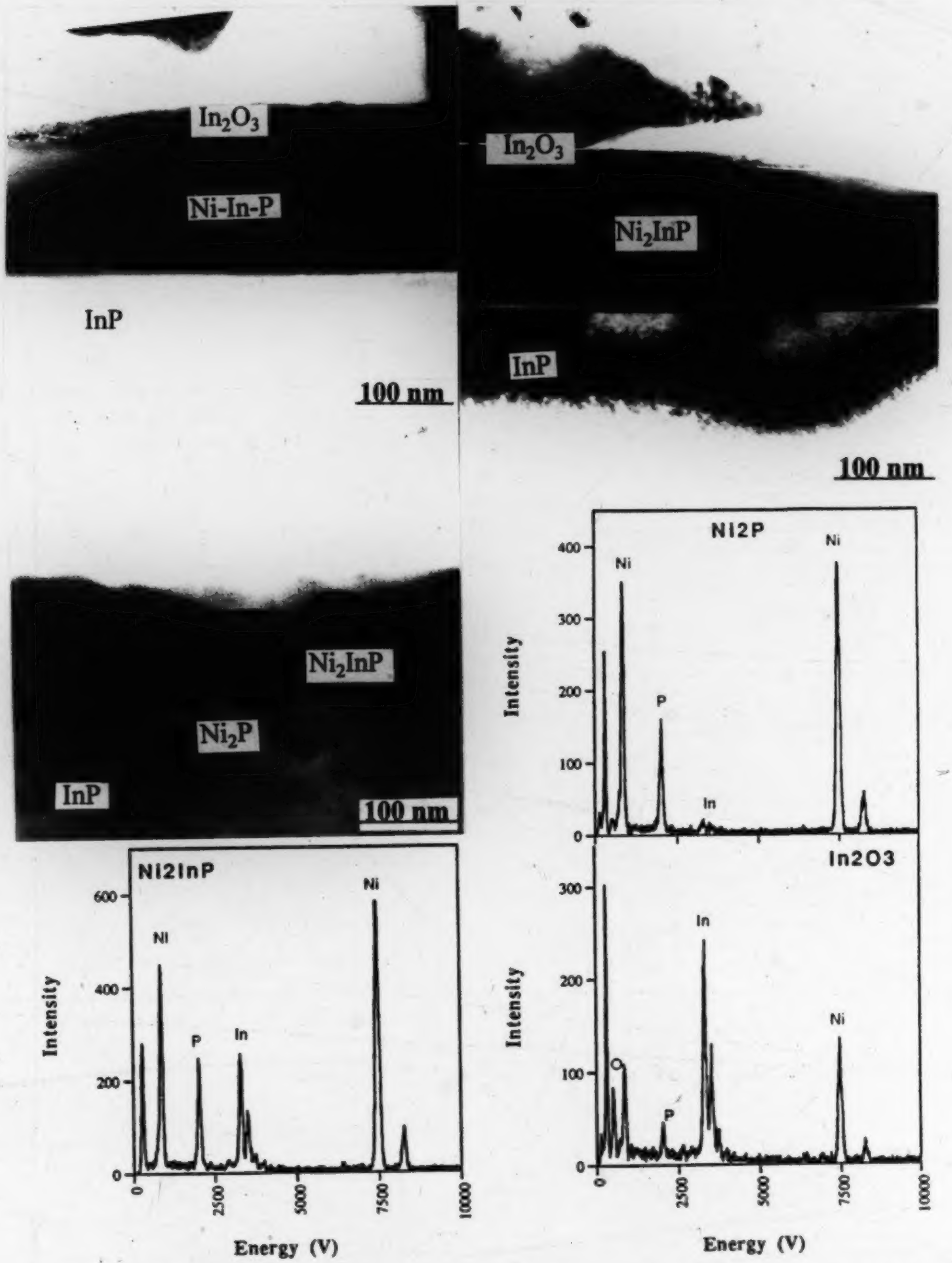

Fig. 5-5 BF micrographs and EDX spectra from cross section specimens of a sample annealed at 250°C for 90 min. Note, that these micrographs are taken from different regions of the same specimen, indicating the non-uniform nature of the crystallization process.

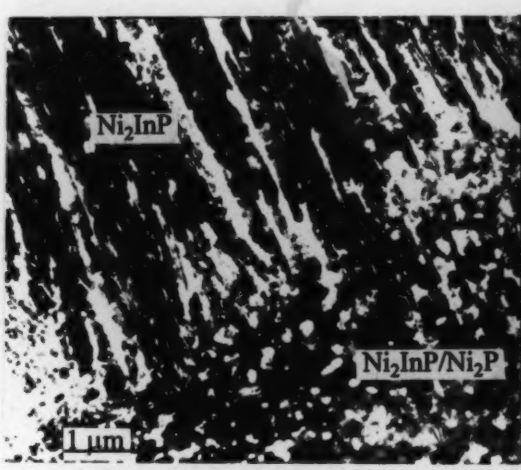
Ni_2InP
Ni_2InP/Ni_2P
1 µm

Fig. 5-6 BF micrograph from a plan view specimen of a sample annealed at 280°C for 5 min. Two distinct regions are shown, i.e., single crystalline Ni_2InP (upper left) and a polycrystalline Ni_2P/Ni_2InP mixed region (lower right).

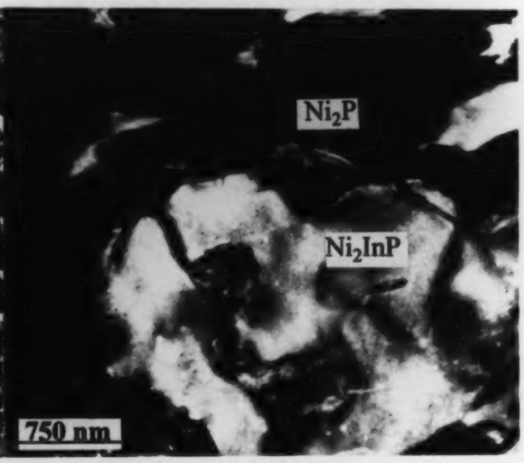
Ni_2P
Ni_2InP
750 nm

Fig. 5-7 (a) BF micrograph of a plan view specimen annealed at 400°C for 15 min.

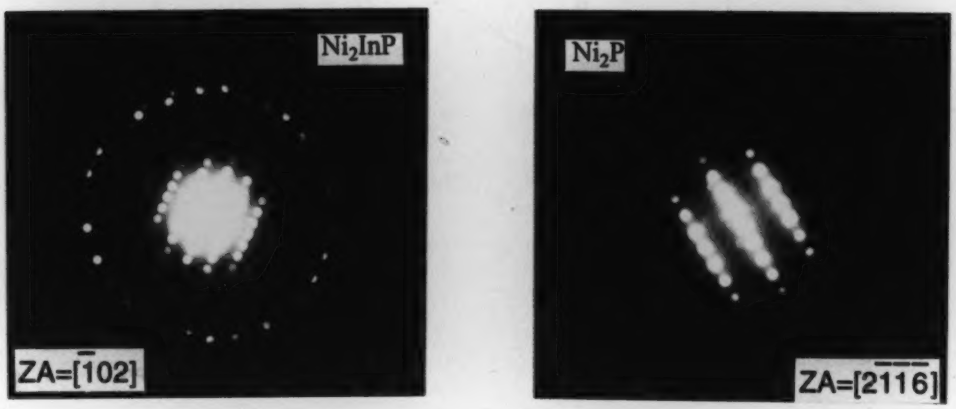
Ni_2InP
$ZA=[\bar{1}02]$
Ni_2P
$ZA=[2\bar{1}\bar{1}\bar{6}]$

(b) (c)

Fig. 5-7 CBED patterns (b) and (c) from (a) showing that two phases are present, Ni_2P and Ni_2InP.

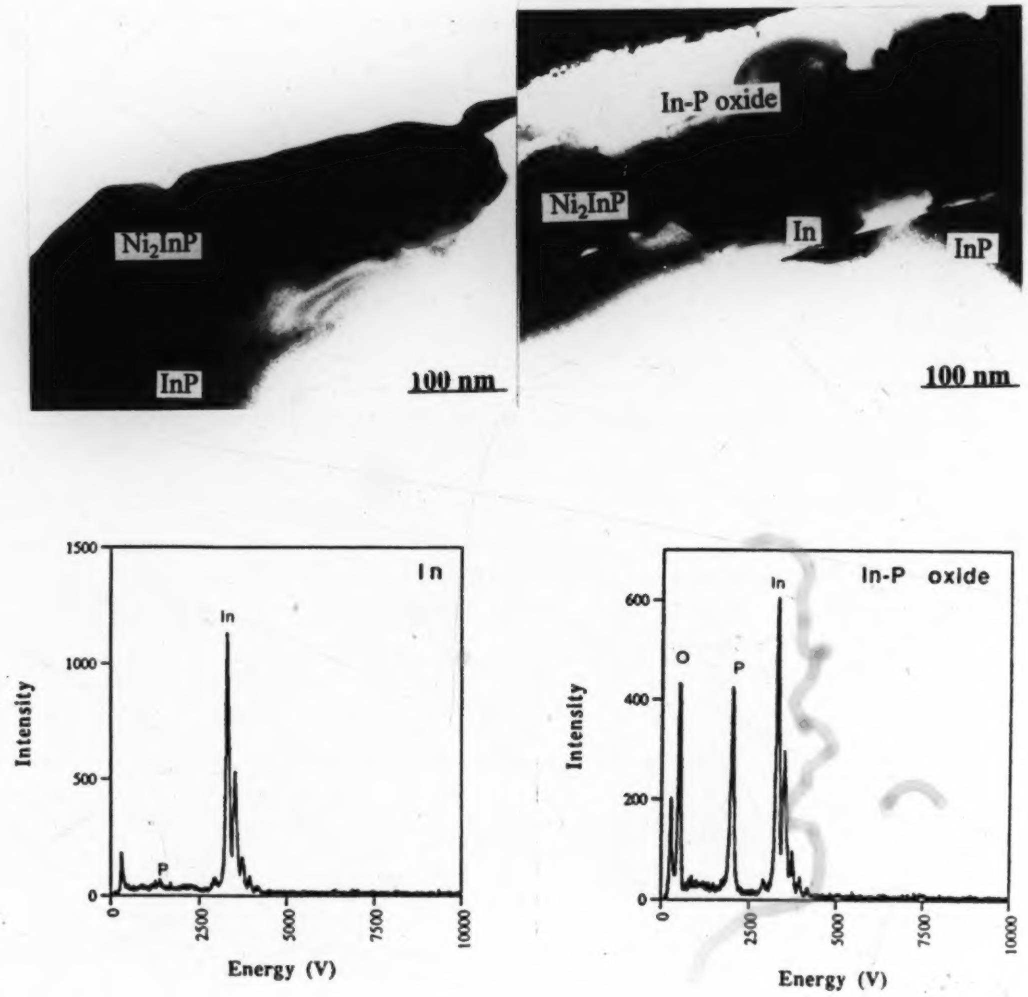

Fig. 5-8 BF micrograph and EDX spectra from different regions of a specimen annealed at 500°C for 20 min. The layer has become non-uniform and shows sign of agglomeration.

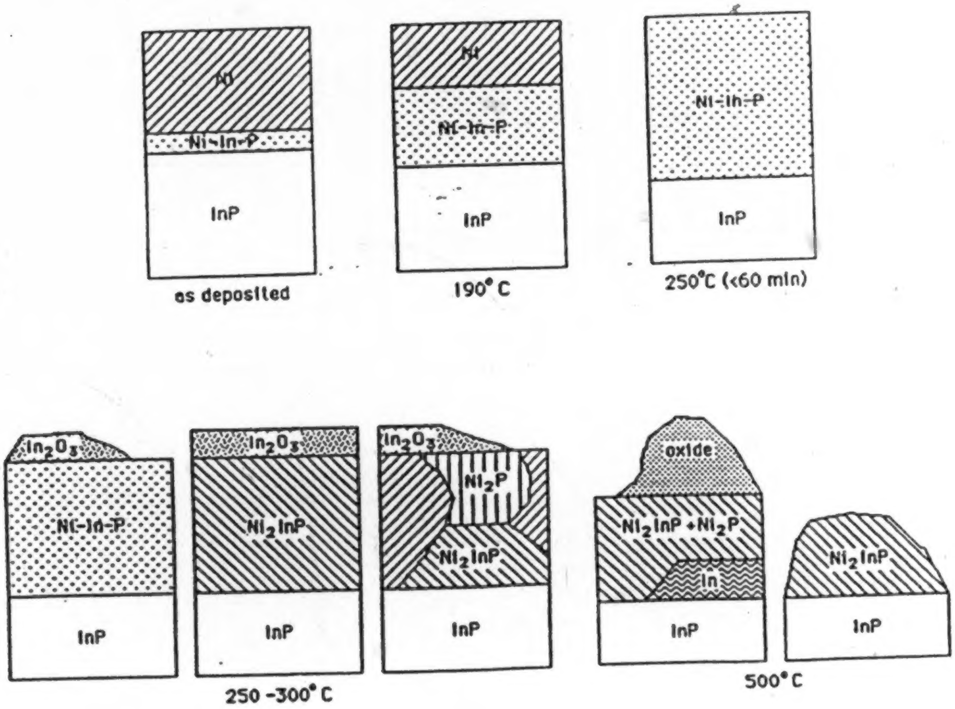
Ni
Ni-In-P
InP
as deposited
Ni
Ni-In-P
InP
190° C
Ni-In-P
InP
250°C (<60 min)
In_2O_3
Ni-In-P
InP
In_2O_3
Ni_2InP
InP
250 -300° C
In_2O_3
Ni_2P
Ni_2InP
InP
oxide
$Ni_2InP + Ni_2P$
In
InP
Ni_2InP
InP
500° C

Fig. 5-9 A schematic representation of reactions occurring during the annealing of Ni/InP.

Ni_2InP
ZA=[001]

Fig. 5-10 CBED pattern from [001] orientation of Ni_2InP.

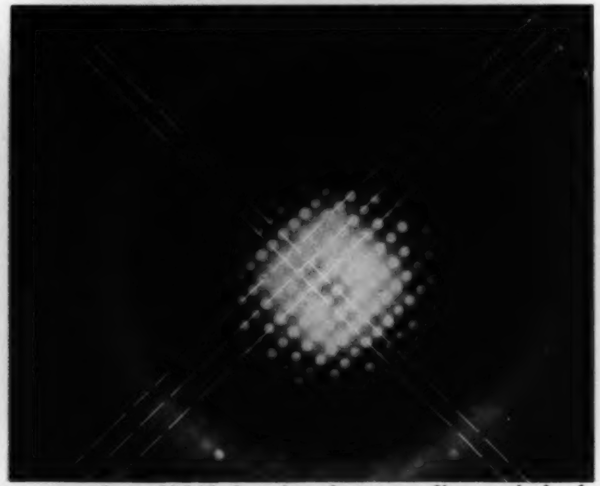

Fig. 5-11 CBED pattern from [001] showing that spots line up in both the [100] and [010] directions.

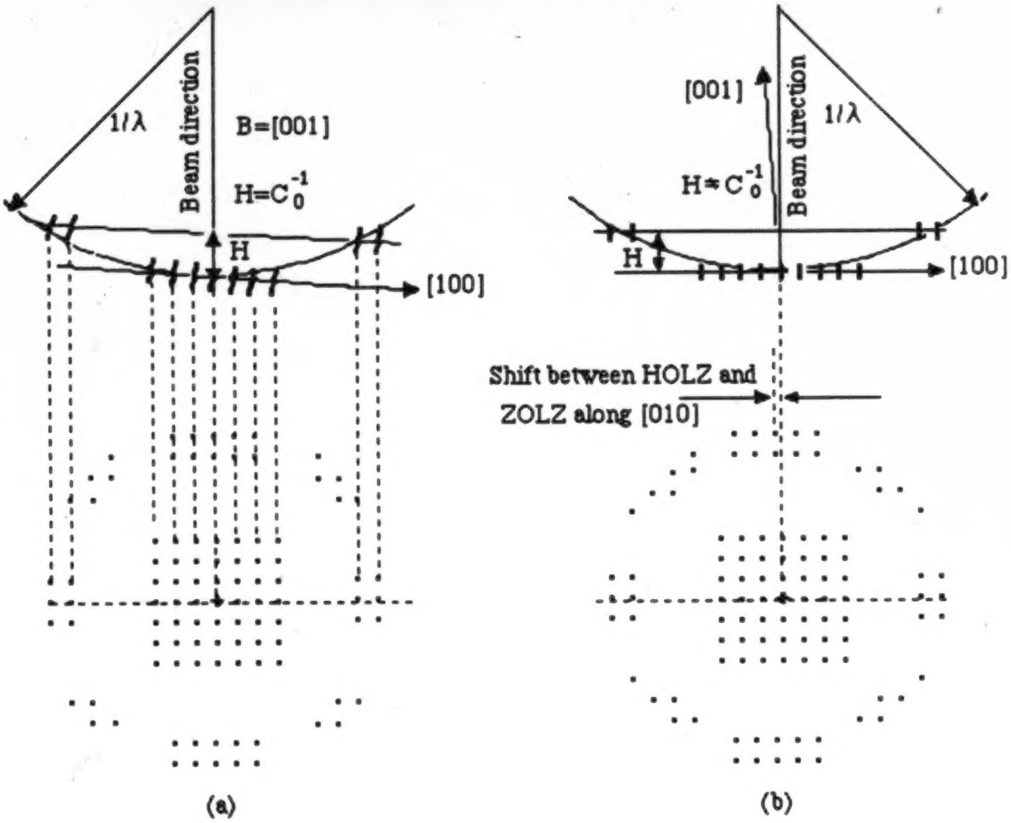
1/λ
Beam direction
B=[001]
$H=C_0^{-1}$
H
[100]
(a)
[001]
Beam direction
1/λ
$H=C_0^{-1}$
H
[100]
Shift between HOLZ and
ZOLZ along [010]
(b)

Fig. 5-12 Schematic drawings showing cases where a) the beam direction is parallel to the [001] direction and b) beam is perpendicular to the ZOLZ containing [100] and [010] g vectors.

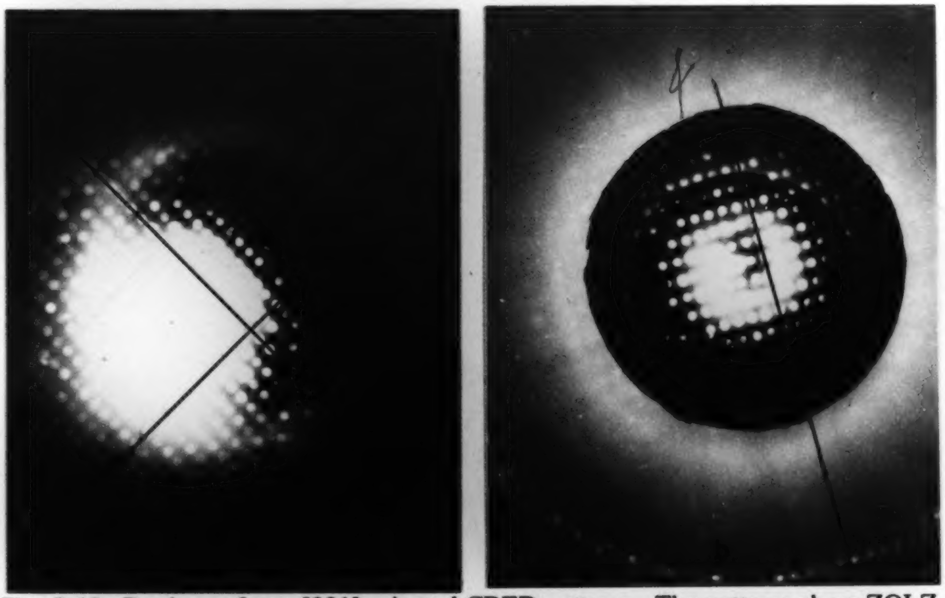

Fig. 5-13 Portions of two [001] oriented CBED patterns. The patterns show ZOLZ and FOLZ spots along the [010] direction. ZOLZ and FOLZ spots line up along the [010] direction in (a), but are slightly misaligned in (b).

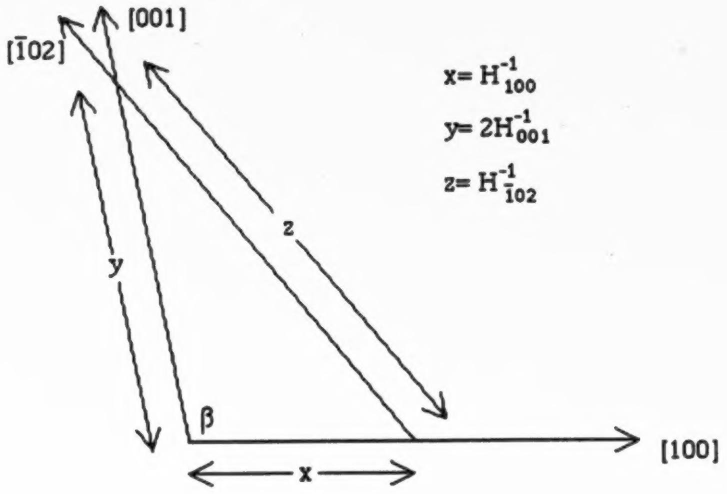

Fig. 5-14 Schematic drawing showing how the angle β can be calculated from 3 coplanar reciprocal lattice vectors perpendicular to the [010] direction.

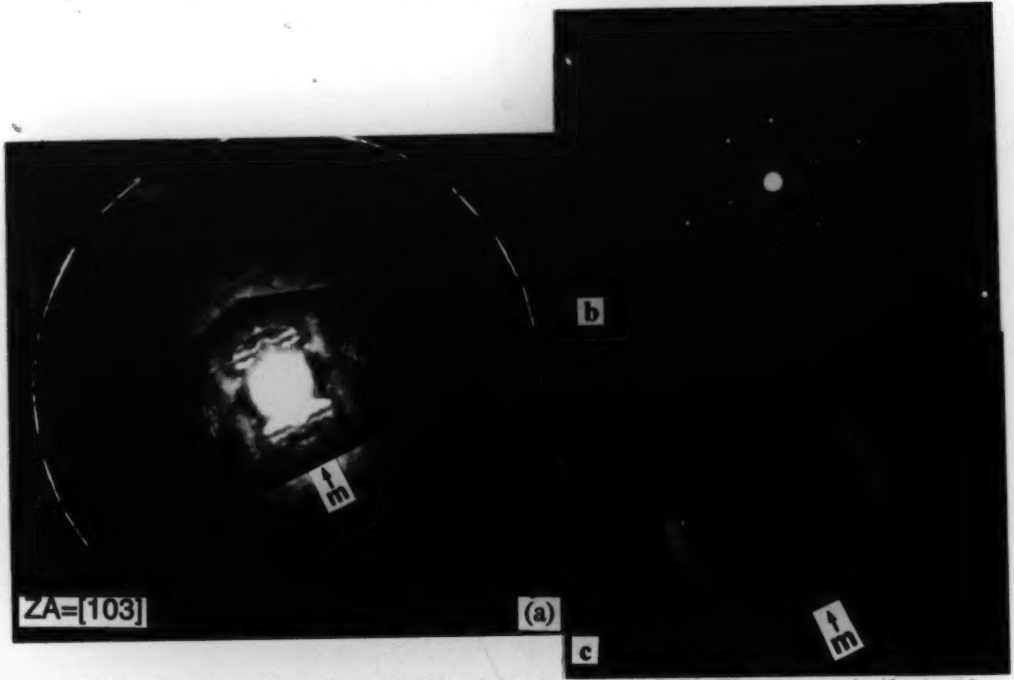

Fig. 5-15 CBED patterns from [103] orientation of Ni_2InP. The pattern in (b) is taken with a smaller condenser aperture than the patterns in (a) and (c). The pattern in (a) gives the whole pattern symmetry (m); the pattern in (b) shows the ZOLZ symmetry (2mm); the pattern in (c) gives the zero order disc symmetry (m).

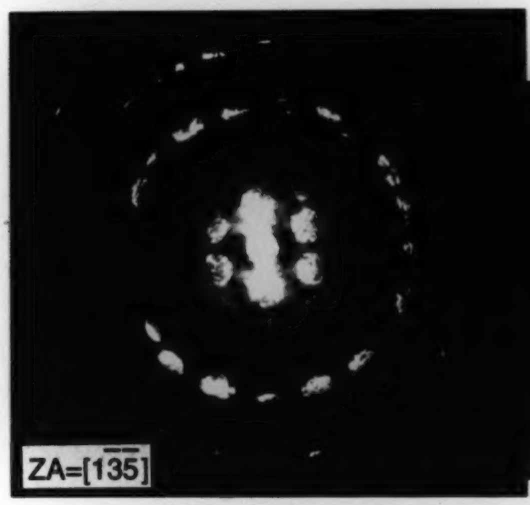

Fig. 5-16 CBED pattern from $[1\bar{3}\bar{5}]$ orientation of Ni_2InP. The ZOLZ symmetry is 2, while the whole pattern symmetry is 1.

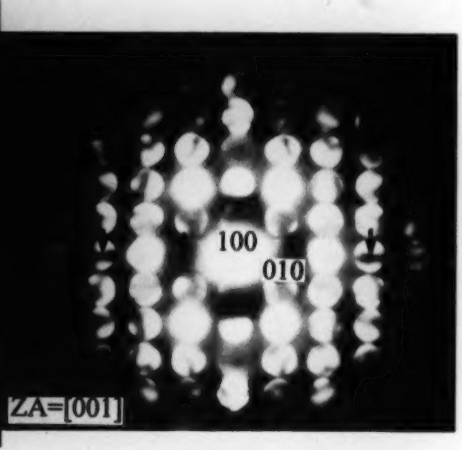

Fig. 5-17 ZOLZ spots from [001] oriented CBED pattern from Ni_2InP.
Alternate forbidden reflections are visible along the [010] direction at k = ±1,3,5,...

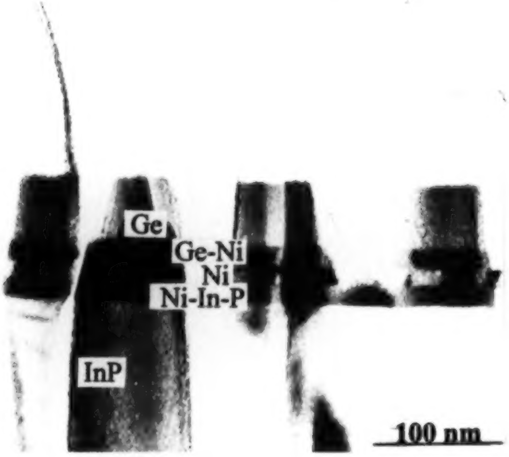

Fig.5-18 BF micrograph of an as-deposited cross section specimen showing the layer sequence: Ge/Ge-Ni/Ni/Ni-In-P/InP.

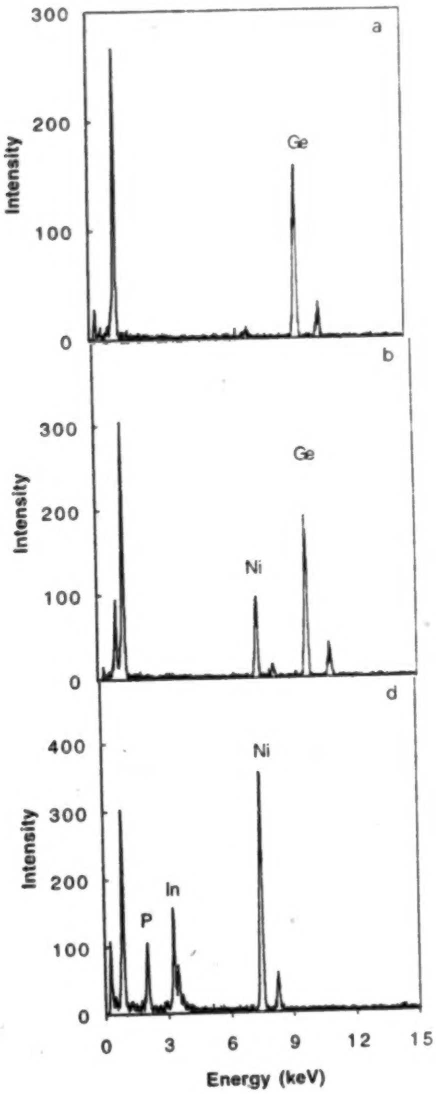

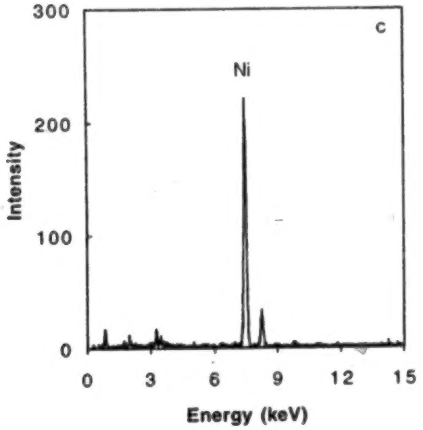

Fig. 5-19 EDX spectra taken from each layer of an as deposited specimen: (a) outer layer of Ge, (b) Ge-Ni, (c) Ni and (d) the inner most layer of Ni-In-P.

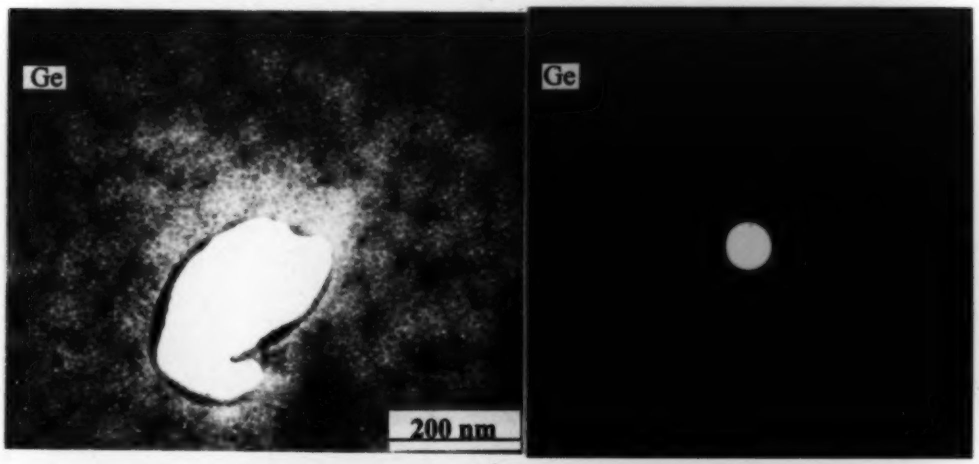

(a) (b)

Fig. 5-20 (a) BF micrograph of Ge from an as deposited plan view specimen. (b) SAD pattern from Ge layer shown in (a) indicating that it is amorphous.

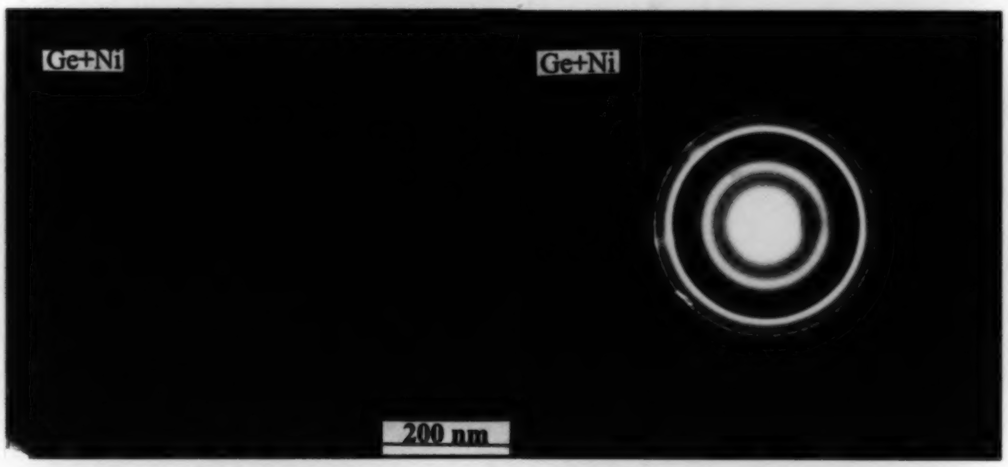

(a) (b)

Fig. 5-21 (a) BF micrograph of the Ge-Ni mixed layer from an as deposited plan view specimen. (b) SAD pattern from (a) (rings are from polycrystalline Ni and a diffuse ring from amorphous Ge).

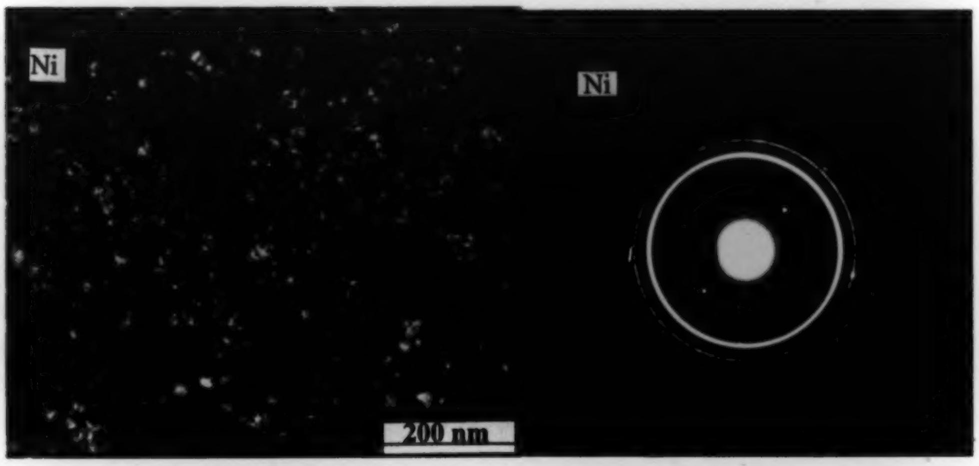

(a) (b)

Fig. 5-22 (a) BF micrograph of Ni layer from an as deposited plan view specimen. InP is adjacent to Ni. (b) SAD pattern from the Ni layer shown in (a). Spots are from InP.

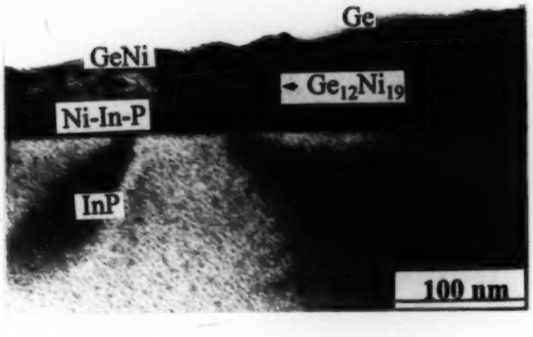
Ge
GeNi
← $Ge_{12}Ni_{19}$
Ni-In-P
InP
100 nm

Fig. 5-23 BF micrograph of a cross section specimen annealed at 250°C for 60s.

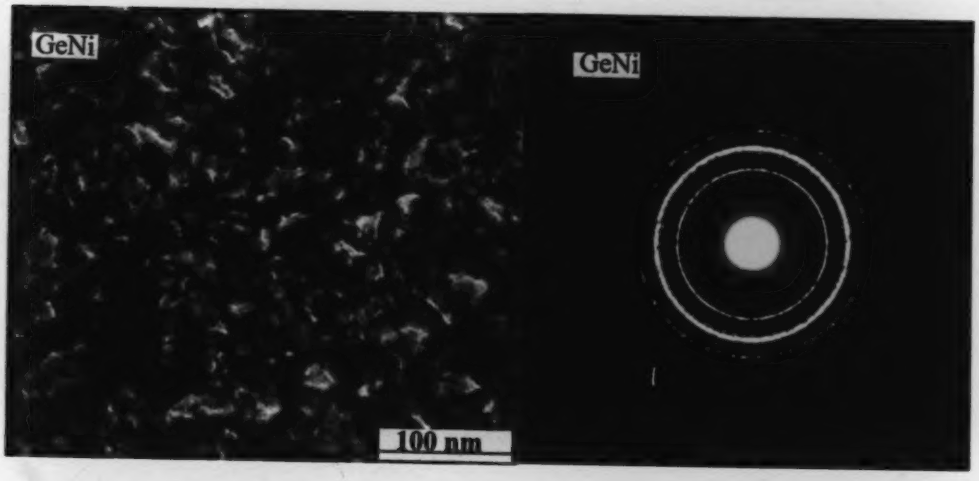

(a) (b)

Fig. 5-24 (a) BF micrograph of the GeNi layer from a plan view specimen annealed at 250°C for 60s showing that the grain size is 40-50nm. (b) SAD pattern from GeNi layer shown in (a).

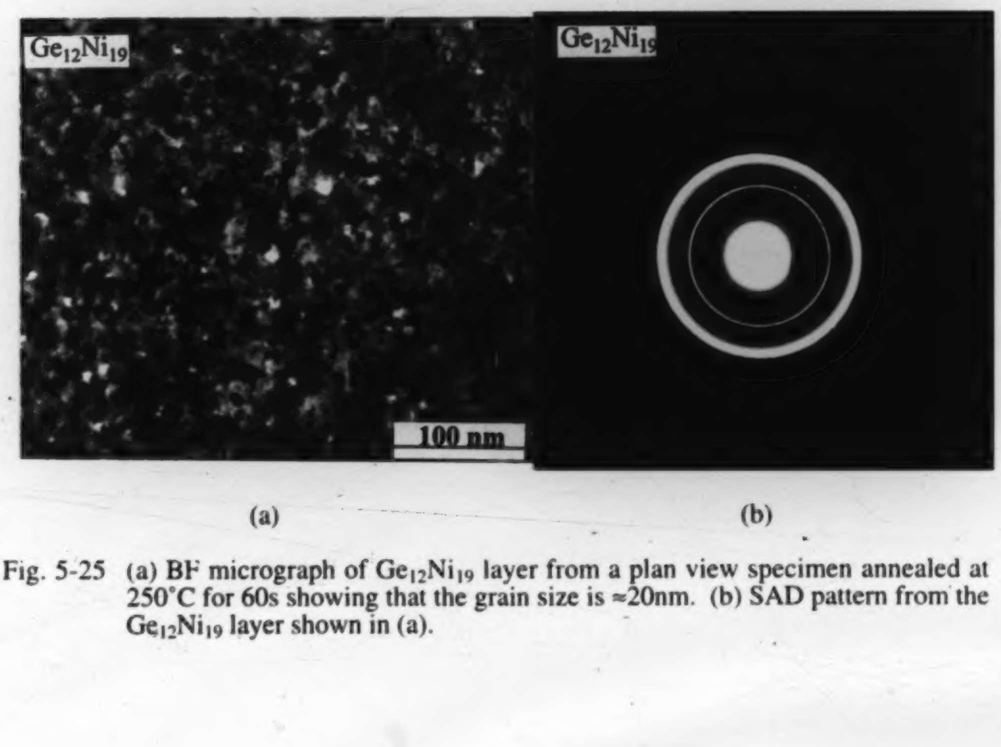

(a) (b)

Fig. 5-25 (a) BF micrograph of $Ge_{12}Ni_{19}$ layer from a plan view specimen annealed at 250°C for 60s showing that the grain size is ≈20nm. (b) SAD pattern from the $Ge_{12}Ni_{19}$ layer shown in (a).

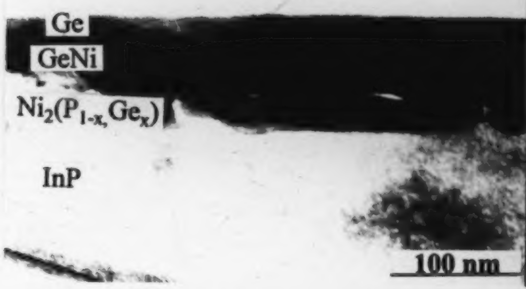
Ge
GeNi
$Ni_2(P_{1-x,}Ge_x)$
InP
100 nm

Fig.5-26 BF micrograph of a cross section specimen annealed at 250°C for 120s

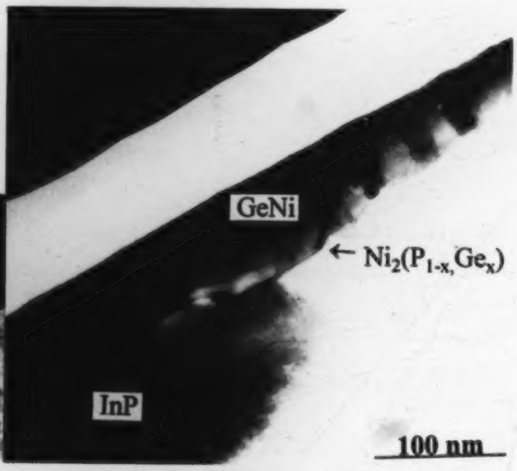
GeNi
← $Ni_2(P_{1-x,}Ge_x)$
InP
100 nm

Fig. 5-27 (a) TEM image of a cross section specimen annealed at 250°C for 240 s.

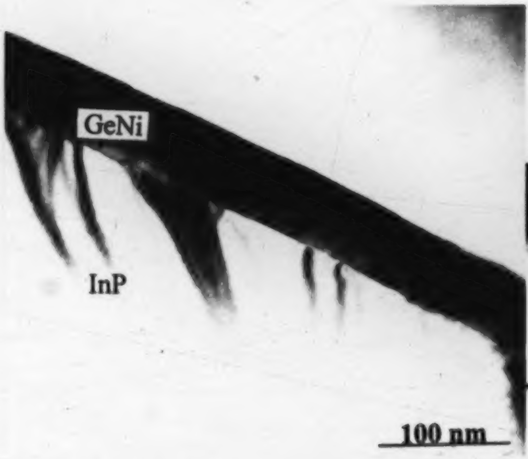
GeNi
InP
100 nm

Fig. 5-27 (b) TEM image of a cross section specimen annealed at 250°C for 480 s.

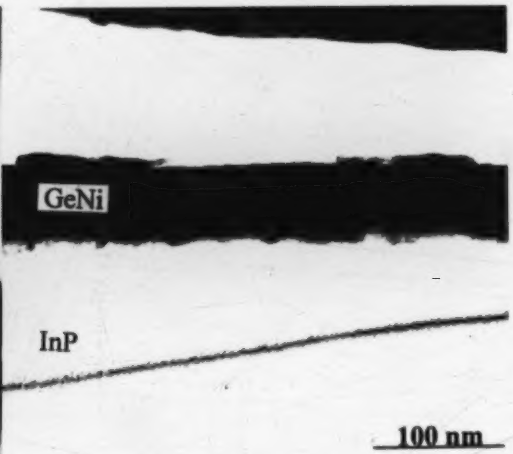
GeNi
InP
100 nm

Fig. 5-28 BF micrograph of a cross section specimen annealed at 350°C for 60s

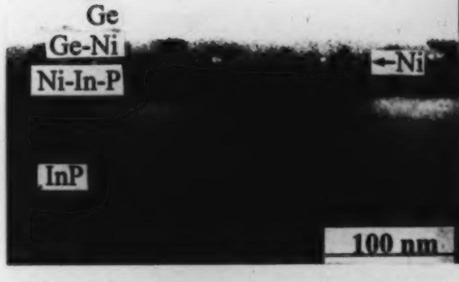
Ge
Ge-Ni
Ni-In-P
←Ni
InP
100 nm

Fig. 5-29 BF micrograph of a cross section specimen heated at 160°C for two minutes showing that the thickness of the amorphous ternary layer has increased relative to the as deposited sample.

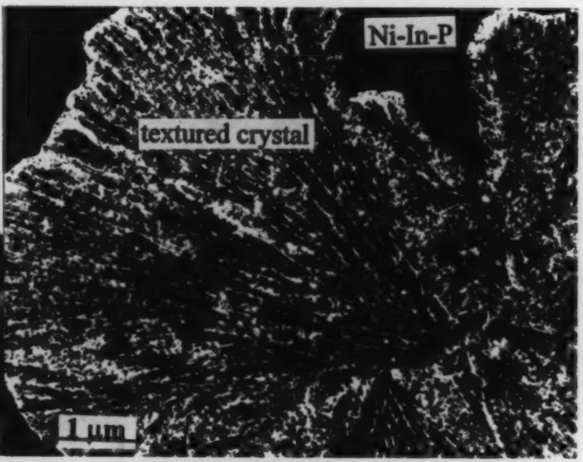
Ni-In-P
textured crystal
1 μm

Fig. 5-30 (a) BF micrograph of the inner layer from a specimen annealed at 250°C for 90s, showing two regions, i.e., the amorphous region and a crystallized region with a nucleation site,

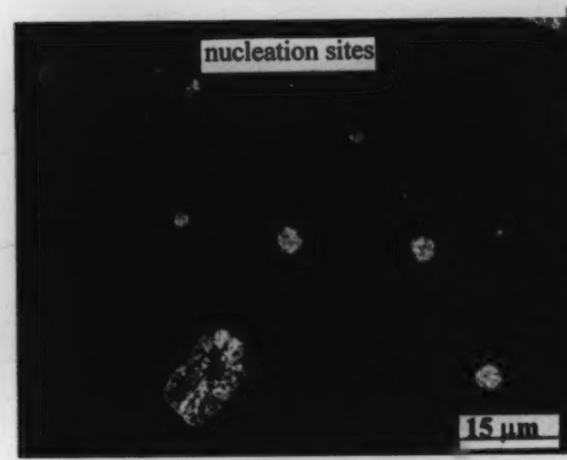
nucleation sites
15 μm

Fig. 5-30 (b) BF micrograph of the inner layer from a specimen annealed at 250°C for 90s, showing distribution of the nucleation sites.

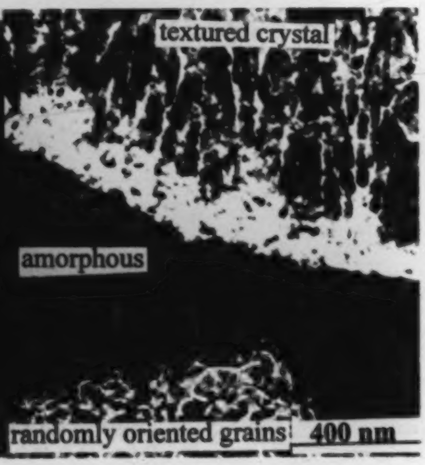
textured crystal
amorphous
randomly oriented grains
400 nm

Fig. 5-31 BF micrograph of crystallized region with small grains showing that the growth of the grains is limited by their orientations.

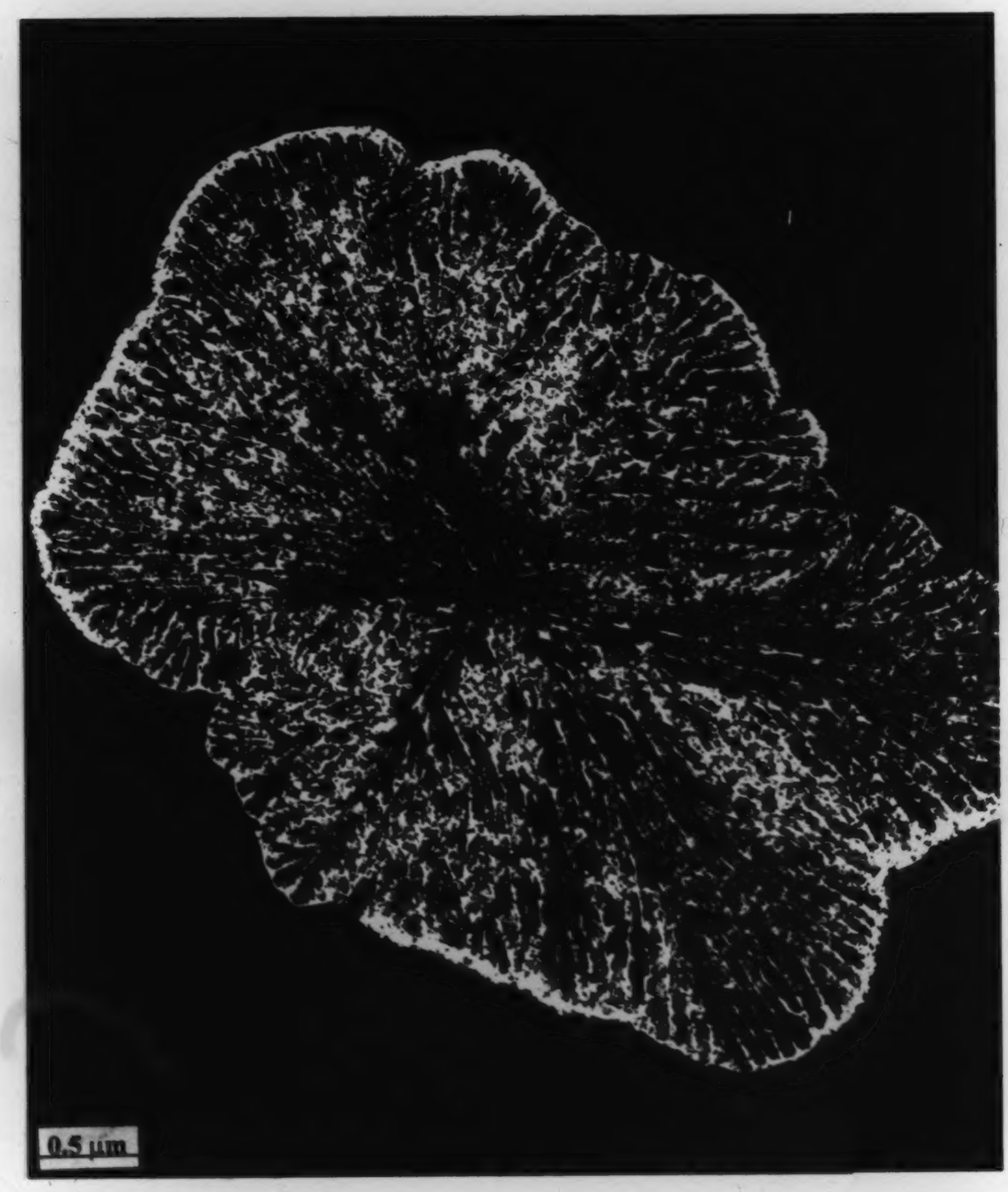

Fig. 5-30 (c) Micrograph of the inner layer from a specimnen annealed at 250°C for 90s showing a nucleation site.

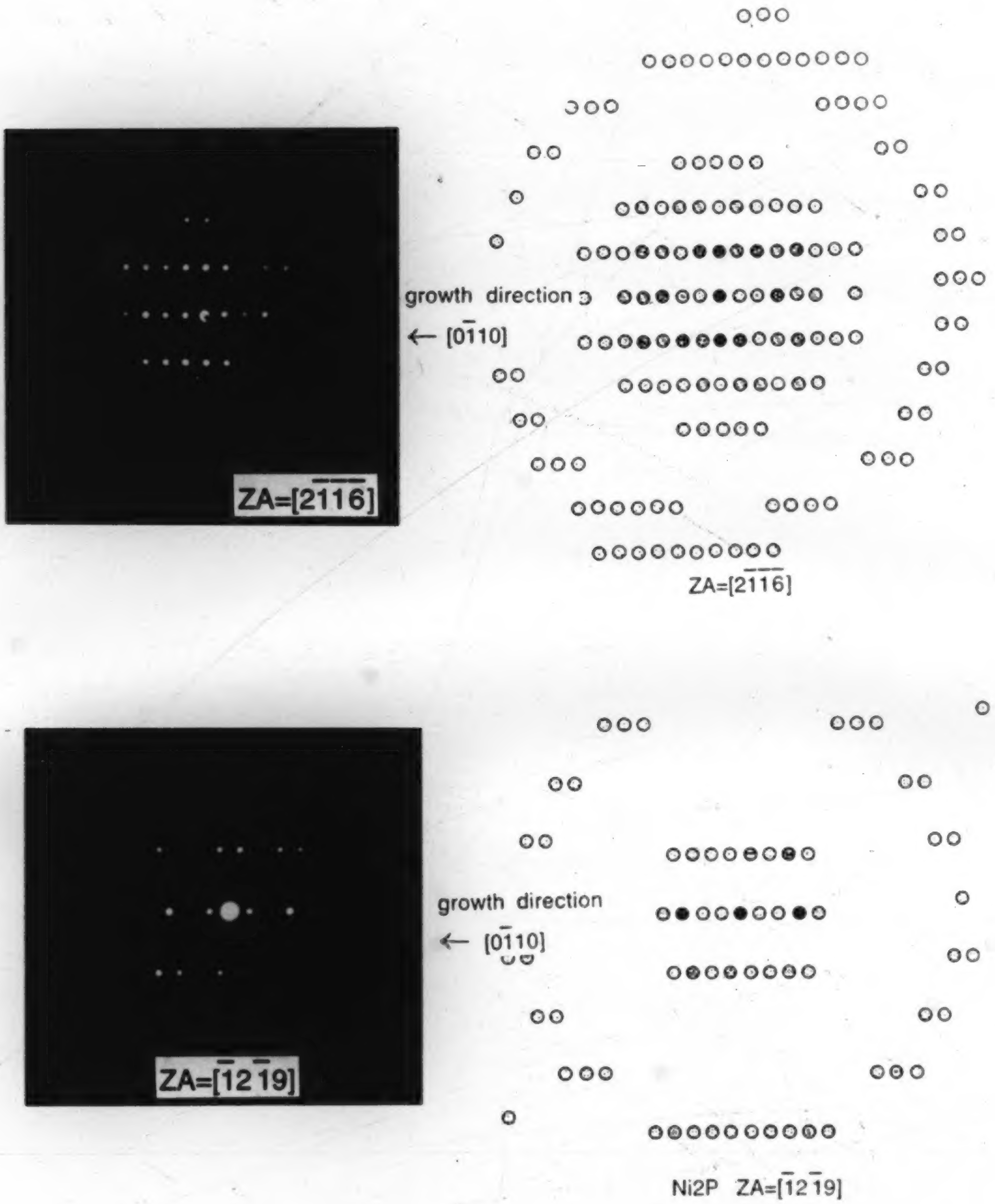
ZA=[2$\bar{1}\bar{1}\bar{6}$]
growth direction
← [0$\bar{1}$10]
ZA=[2$\bar{1}\bar{1}\bar{6}$]
ZA=[$\bar{1}$2$\bar{1}$9]
growth direction
← [0$\bar{1}$10]
Ni2P ZA=[$\bar{1}$2$\bar{1}$9]

Fig.5-32 (a) Two sets of diffraction patterns and (b) computer simulations showing that the grain growth direction is <0$\bar{1}$10>.

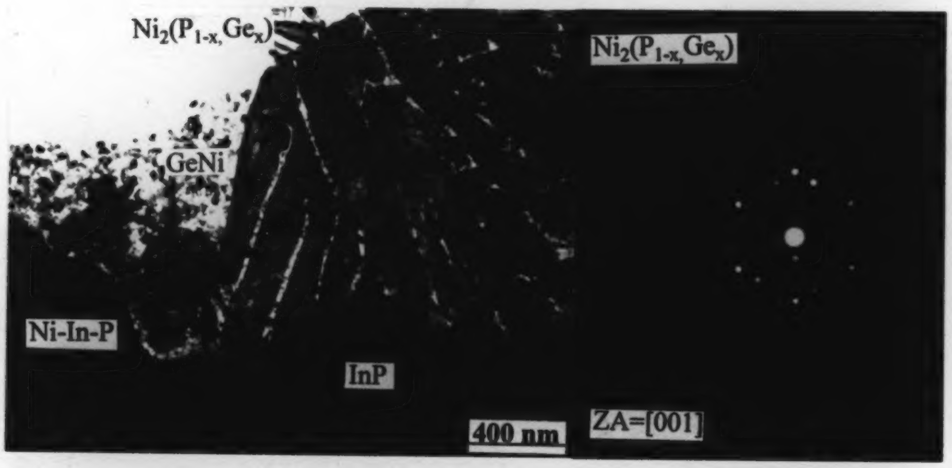
$Ni_2(P_{1-x},Ge_x)$
$Ni_2(P_{1-x},Ge_x)$
GeNi
Ni-In-P
InP
400 nm
ZA=[001]

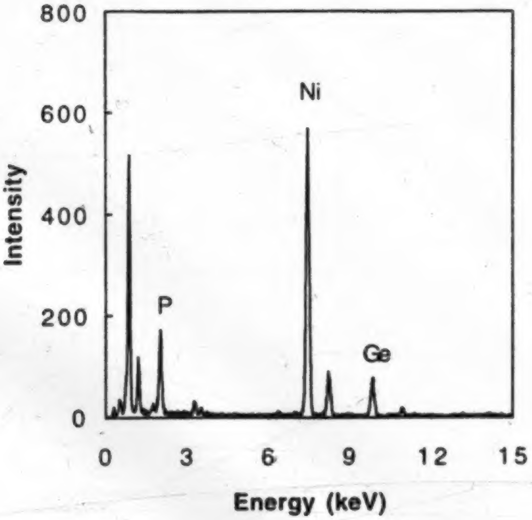

Fig. 5-33. (a) BF micrograph of the textured single crystal sandwiched by a Ge-Ni layer and InP. (b) CBED diffraction pattern (ZA=[001]) from the textured single crystal and (c) EDX spectrum from the textured crystal.

Ge-In

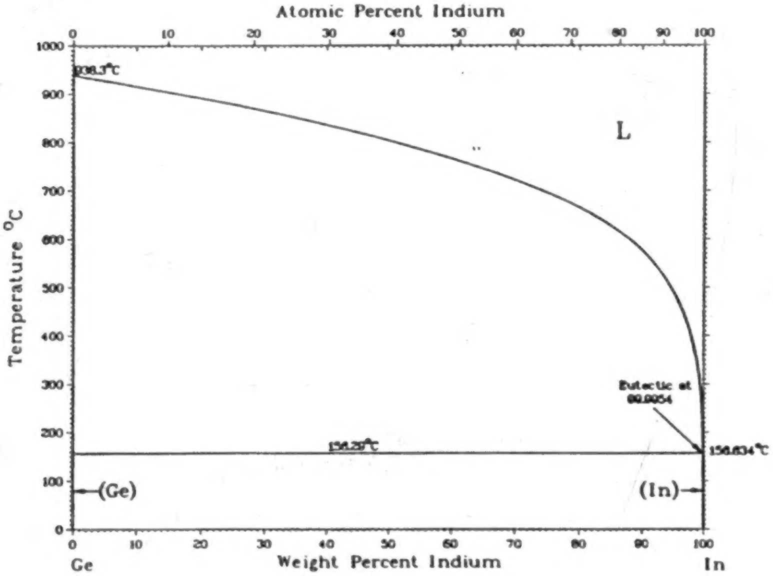

Ge-Ni

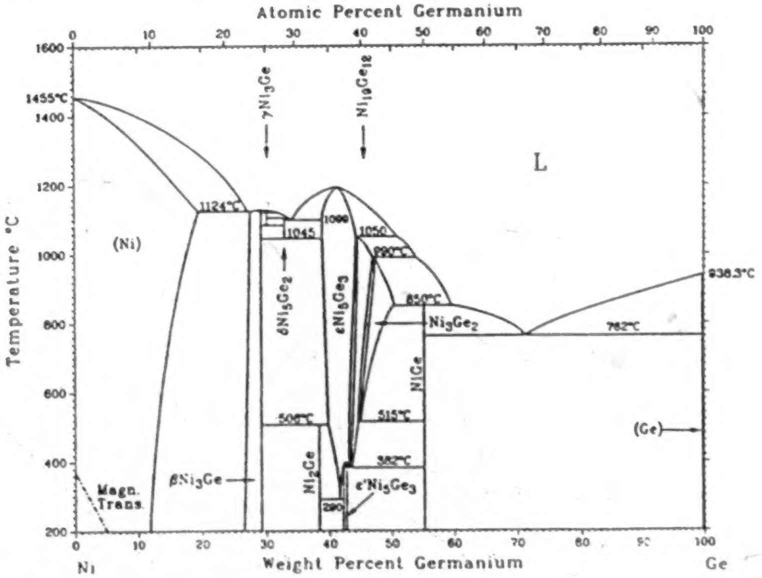

Fig. 5-34 Ge-In and Ge-Ni phase diagrams.

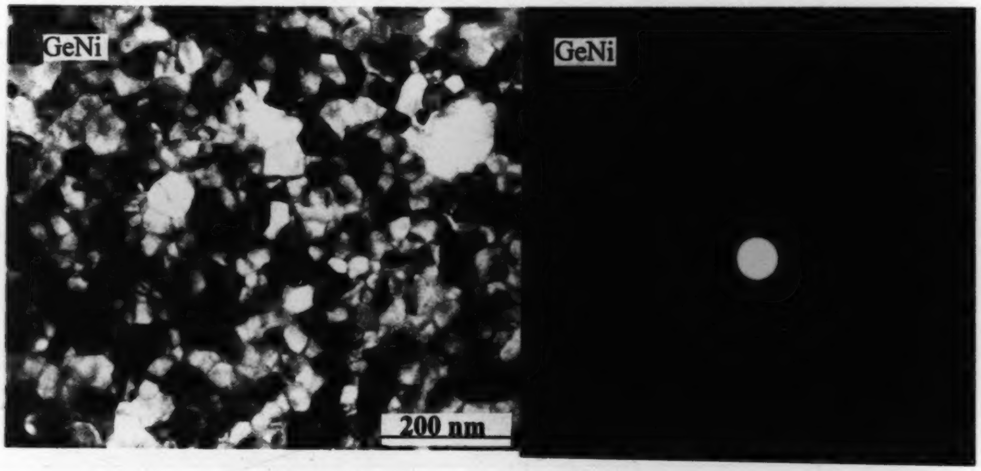

(a) (b)

Fig. 5-35 (a) BF micrograph of the GeNi layer from a plan view specimen annealed at 350°C for 60s.
(b) SAD pattern from the layer shown in (a).

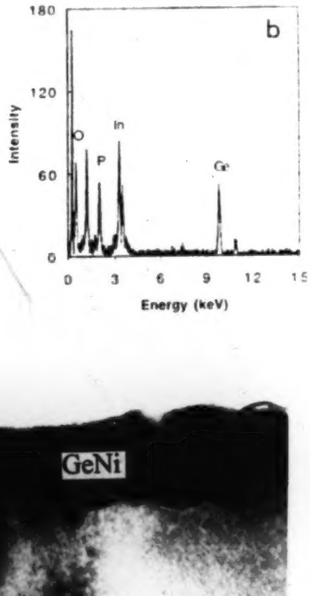

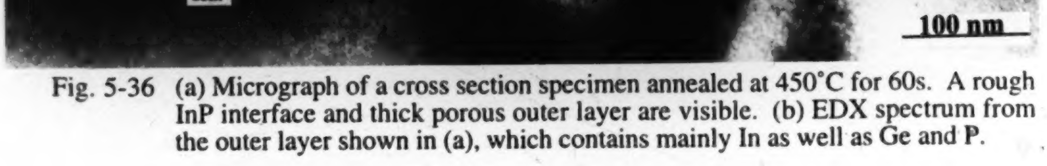

Fig. 5-36 (a) Micrograph of a cross section specimen annealed at 450°C for 60s. A rough InP interface and thick porous outer layer are visible. (b) EDX spectrum from the outer layer shown in (a), which contains mainly In as well as Ge and P.

Schematic Reactions of Ge/Ni Metallizations to InP

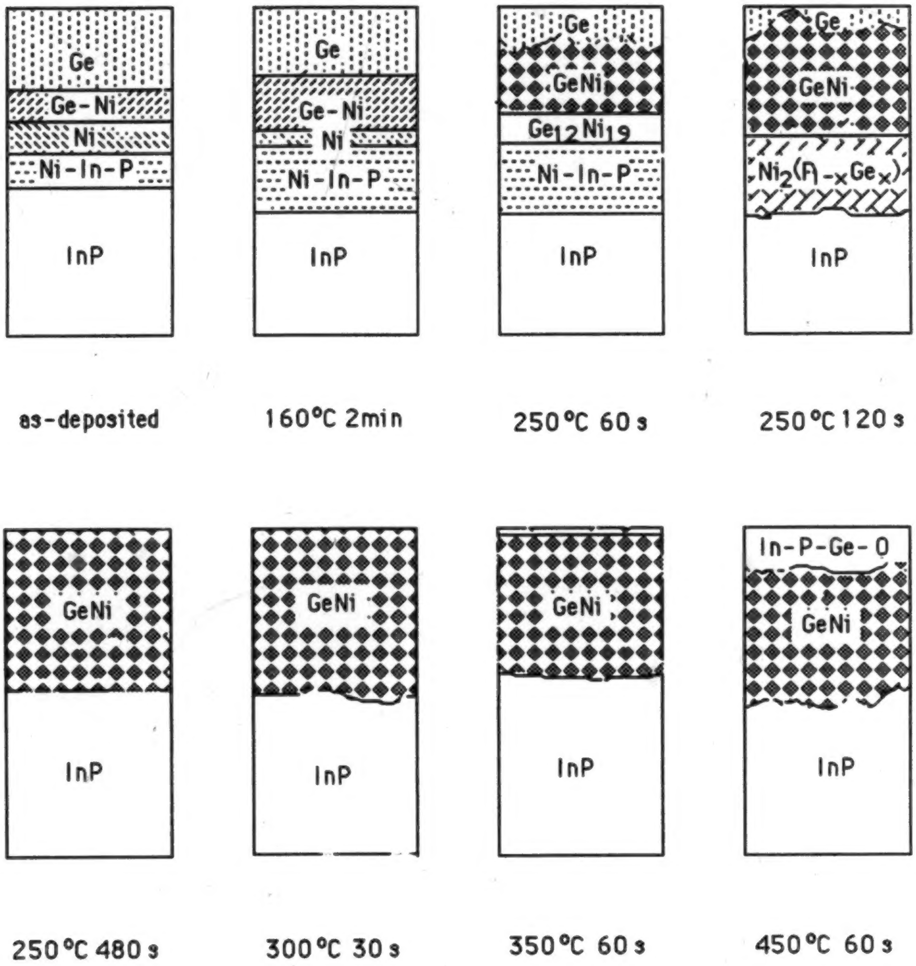
Ge
Ge-Ni
Ni
Ni-In-P
InP
as-deposited
Ge
Ge-Ni
Ni
Ni-In-P
InP
160°C 2min
Ge
GeNi
$Ge_{12}Ni_{19}$
Ni-In-P
InP
250°C 60 s
Ge
GeNi
$Ni_2(P_{1-x}Ge_x)$
InP
250°C 120 s
GeNi
InP
250°C 480 s
GeNi
InP
300°C 30 s
GeNi
InP
350°C 60 s
In-P-Ge-O
GeNi
InP
450°C 60 s

Fig. 5-37 Schematic representation of reactions between the Ge/Ni metallization and InP.

Chapter 6

Summary and Recommendations

6-1 Summary

Interfacial reactions that occur during annealing in three metallization systems, i.e., Ti (100 nm)/InP, Ni (50 nm)/InP, and Ge (52.5 nm)/Ni (25 nm)/InP, have been characterized using transmission electron microscopy (TEM) techniques. In each system, the reaction mechanisms between the metallizations and InP substrate have been explored. The relationship between microstructures and electrical properties of Ge/Ni-InP have also been investigated. Summaries of the experimental results are as follows:

For the Ti/InP system, the deposited Ti film possesses a <001> preferred orientation. No interfacial reactions take place in the specimens annealed at temperatures less than 325°C. Reactions between Ti and InP were observed after annealing at 325°C for 5 min, resulting in an In-rich region and a Ti-P regions at the Ti/InP interface. Further decomposition of InP occurred at higher temperatures. A continuous layer of metallic In and TiP formed between InP and Ti in the specimen annealed at 350-550°C. Most of the P from the decomposition of InP evaporated through the In, TiP and Ti layers. At higher temperatures, the surface of the Ti layer oxidized and In diffused through the TiP and Ti layers to the surface to form In_2O_3. Annealing temperatures ≥500°C resulted in rough interfaces. Both TiP and Ti grains were subjected to growth as annealing temperatures were increased.

For the Ni/InP system, initial annealing at low temperatures led to formation and growth of an amorphous ternary phase ($Ni_{\approx 3}InP$). Complete consumption of Ni occurred by 250°C resulting in an uniform amorphous ternary layer. Crystallization of the amorphous ternary phase took place at annealing temperatures ranging from 250°C to 300°C. Random nucleation of Ni_2InP occurred at the amorphous layer/InP interface and then preferentially orientated grains grew to form single crystalline Ni_2InP areas. In addition, Ni_2P and In_2O_3 formed at temperatures ranging from 250°C to 300°C. Partial decomposition of Ni_2InP occurred at ~500°C resulting in the formation of Ni_2P and release of metallic In. Indium diffused to the surface to oxidize, forming In_2O_3.

For the Ge/Ni/InP system, the contact structure of the as deposited specimen consisted of Ge/Ge-Ni/Ni/amorphous ternary phase/InP instead of the nominal scheme of

52.5 nm Ge/ 25 nm Ni /InP. Reactions between Ge and Ni began at temperatures <160°C, forming GeNi as well as $Ge_{12}Ni_{19}$. $Ge_{12}Ni_{19}$ was unstable and disappeared in later anneals. Eventually the reaction between Ge and Ni resulted in a continuous layer of GeNi. An amorphous ternary phase (Ni-In-P) formed at the Ni/InP interface during low temperature annealing (<250°C). It grew as temperatures were increased. Higher temperature annealing (≥250°C) led to decomposition of the amorphous ternary phase, resulting in the formation of a textured Ni_2P-type compound, which then transformed to GeNi at longer annealing times and/or higher temperatures. Decomposition of the amorphous ternary phase also released In and the transformation of Ni_2P to GeNi (reaction with Ge) produced P, which may have made it possible for InP to regrow epitaxially. Higher temperature annealing (>400°C) resulted in further InP decomposition and roughening of the InP surface.

6-2 Recommendations

From experimental observations in the Ge/Ni/InP system, it is proposed that regrowth of InP occurred during Ni_2P decomposition. As a result, a laterally smooth interface formed, which is required for good ohmic contact fabrication. However, the occurrence of epitaxial regrowth of InP was not conclusively demonstrated. Experiments using marker layers could be done to confirm this phenomenon.

As mentioned in the beginning of the thesis, an atomic ratio of Ge/Ni slightly more than 1 was chosen for the metallization, since GeNi is believed to be stable in contact with InP during annealing (up to at least 450°C). The excess Ge is believed to be necessary for localized doping of the underlying semiconductor to achieve the required low contact resistance values. Higher temperature annealing resulted in InP interface roughening (~450°C) and InP decomposition, which destroys the Ge localized doping effect and therefore degrade the contact quality. Additional studies are needed to confirm the role of Ge in attaining low resistance ohmic contacts.

In order to reveal the relationship between electrical properties and contact microstructures, electrical property measurement should be done systmatically. The Ge/Ni metallization system underwent a number of reactions during annealing. The effect of each reaction or each phase on electrical propertiescan be only explored by more complete electrical measurements.

Since the Ge/Ni metallization was capped with a Ti/Pt/Au layer during electrical property measurements, a more complex system was introduced. The measured electrical results may not directly correlate with the original contact studied (Ge/Ni-InP), if interfacial reactions were affected by the capping layer. Consequently, the contact microstructure with the Ti/Pt/Au capping layer should be examined.